RESOLVING THE PARADOXICAL NATURE OF A BIFUNCTIONAL ENZYME: PATHWAYS AND REGULATION OF INTRAMOLECULAR ELECTRON TRANSFER IN KATG

by

Olive Jofi Njuma

A dissertation submitted to the Graduate Faculty of
Auburn University
in partial fulfillment of the
requirements for the Degree of
Doctor of Philosophy

Auburn, Alabama
August 06, 2016

Keywords: catalase-peroxidase (KatG), peroxidase electron donors (PxEDs), proximal tryptophan, exchange-coupled radical, narrow doublet radical

Approved by

Douglas C. Goodwin, Chair, Associate Professor of Chemistry and Biochemistry
Holly R. Ellis, Associate Professor of Chemistry and Biochemistry
Steven O. Mansoorabadi, Assistant Professor of Chemistry and Biochemistry
Christopher J. Easley, Associate Professor of Chemistry and Biochemistry

Abstract

Catalase-peroxidases (KatGs) are heme-dependent enzymes that use a single active site to perform two activities by protein-based radical dependent mechanisms. As a catalase, in its first step, it reduces H_2O_2 to water and the ferric enzyme is converted to a high valent ferryl-porphyrin π cation radical intermediate, compound I (i.e., Fe^{IV}=O[porphyrin]$^{\bullet+}$). Thereafter, compound I is proposed to undergo an intramolecular electron transfer where the porphyrin radical is reduced by a unique methionine tyrosine tryptophan (MYW) adduct cofactor to form compound I* (i.e., Fe^{IV}=O[MYW]$^{\bullet+}$). Compound I* then reacts with a second equivalent of H_2O_2 producing an oxyperoxidase or compound III-like species referred to as a compound III* (i.e., Fe^{III}-$O_2^{\bullet-}$[MYW]$^{\bullet+}$). Finally, another intramolecular electron transfer from the Fe^{III}-$O_2^{\bullet-}$ heme to the MYW adduct radical occurs forming the ferric heme, O_2, H_2O and a closed shell MYW adduct. In contrast, for the peroxidase cycle, upon the formation of compound I, the enzyme is reduced in two sequential one electron steps by exogenous electron donors, first to form a ferryl intermediate known as compound II (i.e., Fe^{IV}=O) and then to the ferric enzyme, generating two equivalents of donor radical. For the nearly 30 years since its initial discovery, the nature of the interplay between these two activities in KatG has not been understood. All evidence including the pH-dependence of its two activities and the properties of site specific variants has suggested mutual antagonism between both activities. However, our lab recently observed stimulation of KatG catalase activity by peroxidatic electron donors at conditions that coincide with host-defense

mechanisms like the neutrophil oxidative burst (i.e., pH 5.0, large [H_2O_2]). Hence, evidence is also accumulating that KatG uses a peroxidase scaffold, a unique Met-Tyr-Trp covalent adduct, and even assistance from peroxidatic electron donors (PxEDs) to perform its dominant catalase activity. The synergistic effect expands the conditions for KatG as an efficient catalase. This is especially useful for plant and animal pathogens which encounter enormous amounts of H_2O_2 produced by the immune responses of their hosts. This is particularly important for *Mycobacterium tuberculosis*, a known intracellular pathogen most abundant in host neutrophils and macrophages. To this hostile environment, *M. tuberculosis* brings KatG as its only catalase active enzyme.

The purpose of this dissertation is to elucidate the role of PxEDs in this novel mechanism of H_2O_2 decomposition by KatG. We have observed that the return of KatG ferric state at the conclusion of H_2O_2 consumption is not catalytically competent to account for the rate of catalatic H_2O_2 decomposition. These data suggested that catalase inactive intermediates accumulated during turnover. We hypothesized inactive intermediates might accumulate because of off-pathway protein oxidation events and PxEDs prevent the accumulation of these inactive enzyme forms. We also hypothesized that the proximal tryptophan (W321 in *M. tuberculosis* KatG) was a prominent conduit for off-pathway electron transfer. In order to evaluate these hypotheses, we produced the W321F KatG variant to make this site unoxidizable and compared its properties with wild-type KatG. At neutral pH where catalase activity is optimal, the catalase activity of KatG and its W321F variant are nearly identical. At lower pH where the stimulatory effect of PxEDs is maximal (pH 5.0), the unassisted catalase activity of W321F exceeded that of the wild-type enzyme. By stopped-flow, both proteins showed identical initial rates of H_2O_2 decomposition, and

compound III-like species (i.e., Fe^{III}-$O_2^{\bullet-}$) dominated the heme spectrum at these early reaction times. As turnover progressed, wild-type KatG more rapidly lost activity than W321F and transitioned to a mixture of heme states at the conclusion of H_2O_2 consumption. Conversely, W321F sustained higher rates of H_2O_2 consumption and transitioned to a compound I-like species (i.e., Fe^{IV}=O [porphyrin]$^{\bullet+}$) at the time H_2O_2 consumption ceased. Thereafter, the W321F KatG ferric state returned an order of magnitude more rapidly than the wild-type enzyme. PxEDs stimulated catalatic H_2O_2 consumption by both proteins as well as the return of the ferric state after H_2O_2 depletion. However, the effect was more pronounced in both respects for wild-type than W321F KatG.

Samples of both proteins freeze-quenched 10 ms after reaction with H_2O_2 produced a narrow-doublet radical species as detected by electron paramagnetic resonance (EPR) spectroscopy. This signal is consistent with a radical centered on the MYW covalent adduct of KatG. Reactions of wild-type KatG quenched at the time H_2O_2 consumption ceased (6 s), produced a singlet EPR spectrum with clear evidence of exchange-coupling due most likely to the heme center. This is consistent with a radical centered on the proximal tryptophan. At 1 and 5 min after H_2O_2 depletion, protein-based singlet radical species were still detected, albeit at lesser intensity and with much diminished exchange-coupling. These data are indicative of radical migration away from the KatG active site with time. Although W321F KatG showed a protein radical signal at the time of H_2O_2 deletion (1.6 s), no exchange-coupling was evident. In addition, the intensity and persistence of radical species at all subsequent reaction times were substantially diminished compared to the wild-type enzyme. Inclusion of PxED in reactions of wild-type and W321F KatG with H_2O_2 produced only the

narrow-doublet signal corresponding to the MYW adduct radical detected at 10 ms. Little or no protein-based radical was observed at H_2O_2 depletion or any time thereafter. All these data supported our hypotheses that PxEDs stimulate KatG catalase activity by rescuing inactive intermediates that result from off-pathway protein oxidation events starting with oxidation of the proximal tryptophan.

The pH-dependence of the stimulatory effect of PxEDs is striking not only because of the physiological implications of a low-pH catalase activity, but also because of known structural adjustments in KatG that are also pH-dependent. Without a PxED, KatG shows poor catalase activity at pH 5.0. This is attributed at least in part to the position of the enzyme's so-called arginine switch (R418 in *M. tuberculosis* KatG). At pH 8.5, the R418 guanidinium side chain is oriented toward the phenolate oxygen of the MYW adduct, and at pH 4.5, it is oriented to the protein's solvent accessible surface. At pH 6.5, there are equal populations of both conformational states and this corresponds to KatGs optimum unassisted catalase activity.

To investigate the participation of R418 in the mechanism of PxED-stimulated catalase activity, we evaluated R418K and R418A KatG. In most respects, R418K was indistinguishable from wild-type KatG. In contrast, R418A KatG showed a diminished k_{cat}/K_M (7.4×10^{3} $M^{-1}s^{-1}$) for catalase activity at pH 7.0. Activity increased appreciably at pH 5.0 with a k_{cat}/K_M of 5.2×10^{5} $M^{-1}s^{-1}$. PxEDs were able to stimulate R418A KatG to an extent similar to wild-type KatG, albeit with much more PxEDs required for its catalase restoration. Similarly, R418A KatG produced more PxED radicals to H_2O_2 consumed also supports its need for more PxED for its rescue mechanism. By rapid-freeze quench EPR, R418A KatG produced a MYW narrow-doublet radical at 10 ms after its reaction with H_2O_2.

Over time at its point of H_2O_2 depletion (i.e., 20 s), R418A transitioned to an exchange-coupled proximal tryptophanyl radical. More so, remote protein-based radicals persisted throughout turnover even at later times of its reaction with H_2O_2. The less broad and less intense radicals observed are consistent with radical migration from the active site. When PxEDs were included in the reactions, R418A only formed the narrow-doublet radical at 10 ms. Strikingly, the intensity of the narrow-doublet radical produced by R418A KatG when PxED was added was two-fold greater than that seen for either wild-type or W321F KatG. This suggested that R418A KatG recycle more non-MYW adduct radicals back to the active MYW adduct radical. As with wild-type KatG and W321F KatG, little or no other radical was detected at the point of H_2O_2 depletion and thereafter. All these data suggest that R418 influences KatG activity, inactivation, and restoration mechanisms.

In conclusion, at early reaction times corresponding to the most rapid rates of H_2O_2 decomposition, all KatG proteins formed a putative Fe^{III}-$O_2^{\bullet-}$[MYW]$^{\bullet+}$species. Wild-type KatG and R418A KatG transitioned to an exchange-coupled proximal tryptophanyl radical intermediate (Fe^{IV}=O [$W321^{\bullet+}$]) at their points of H_2O_2 depletion. This species slowly reverts to the KatG ferric resting state. In contrast, W321F formed an uncoupled radical which rapidly returns to its ferric state. These data suggest that KatG proximal tryptophan is the first residue that gets oxidized for KatG inactivation. PxEDs reduce all non-MYW radicals but leave the MYW adduct radical untouched thereby stimulating KatG catalase activity. We propose that PxEDs restores catalase active states simultaneous with optimizing catalatic H_2O_2 degradation. This thesis enlightens us on KatG intramolecular electron transfer and protein-based radicals which relates the enzymes catalase and peroxidase mechanisms of

H_2O_2 detoxification. As such, we also propose that the proximal tryptophan facilitates the mutual synergism of both the catalase and peroxidase activities of KatG. Until the present time, the identity and role of KatG physiological electron donor has been a conundrum in the field. The synergism observed in this dissertation may provide some insights into the characteristics of the unknown physiological electron donor. This will carry important ramifications for those organisms which utilize KatG to detoxify the threat posed by H_2O_2, most importantly for organisms like *M. tuberculosis* whose only catalase active enzyme is KatG.

Acknowledgments

My sincere gratitude goes to my advisor Dr. Douglas Goodwin. He has been an exemplary mentor who has been patient with my lack of biochemistry background from the genesis of this project to the revelation. Indeed, this dissertation would not have been feasible if not of his encouragement, willingness, and persistence. His enormous sacrifice and contribution to my career goals and professional aspirations seconds no other. His goal for my career has been for me to become nothing short of an extraordinary scientist.

I am also grateful to my committee members, Dr. Holly Ellis, Dr. Steven Mansoorabadi, and Dr. Christopher Easley, for their contribution and support to see that this dissertation comes out outstanding. I am thankful to Dr. Jin Wang for her time, suggestions, and corrections. I am also grateful to Dr. Eduardus Duin for his assistance with the use of the X-band EPR spectrometer. Finally, I am thankful to our collaborators at Georgia State University (Dr. Aimin Liu and Ian Davis) and the National High Magnetic Field Laboratory at Florida State University (Hans Von Tol, Andrew Ozarowski, and Sebastian Stoian).

I would also like to thank my research colleagues, (Drs. Yu Wang, Elizabeth Ndontsa, and Haijun Duan), Rene Fuanta, Hui Xu, and Jessica Krewall along with several undergraduate students whom I worked with for their support and friendly environment.

My greatest appreciations go to my family, relatives, and friends for their constant love and support throughout my studies. I dedicate this work to my mum (Mrs. Lisonge Sophie Mojoko), my dad (Mr. Monyenge Njuma John), sisters (Lisonge Rita and Enanga Lisonge),

and brother (Njuma John Njuma II) and my entire family for encouraging me through the happy and difficult seasons I encountered during my graduate school career.

Table of Contents

List of Figures

List of Tables

Chapter One: Literature Review

1.1. Oxygen and its Toxicity

Oxygen (O_2) can be viewed as a 'double-edged sword' [1-4]. The versatility of O_2 as both a terminal electron acceptor and an oxidant allows for the generation of enormous amounts of energy in the form of ATP captured by oxidative phosphorylation from the oxidation of nutrient carbon to carbon dioxide. Molecular oxygen, with a triplet (i.e., $^3O_2$) ground state, is relatively unreactive towards most biological molecules because they are singlet in their ground states. The kinetic barrier presented by this spin restriction can be overcome in multiple ways. First, triplet O_2 can be excited to one of two singlet states (i.e., singlet $^1O_2$) by the reversal of the spin of one electron (Fig. 1.1 A) [1, 5]. Second, redox active transition metals can facilitate electron transfer from singlet biological molecules to O_2 to generate superoxide ($O_2^{\bullet-}$), hydrogen peroxide (H_2O_2), hydroxyl ($OH^{\bullet}$) radicals, and/or H_2O. This is because redox-active transition metals are capable of accommodating multiple oxidation and spin states. Therefore, it should not be a surprise that these metals (especially Fe) appear throughout processes connected to O_2.

Despite the use of transition metals to circumvent the spin restriction presented by O_2, the uncontrolled consequences of this interaction are formidable. As such, there are specialized systems in place at all times that are designed to control the interaction between transition metals and O_2. These systems are present at the points of transition metal transport and storage, oxygen transport and storage and at any place where the redox properties of transition metals are required. Whether generated from initial production of singlet O_2 or by

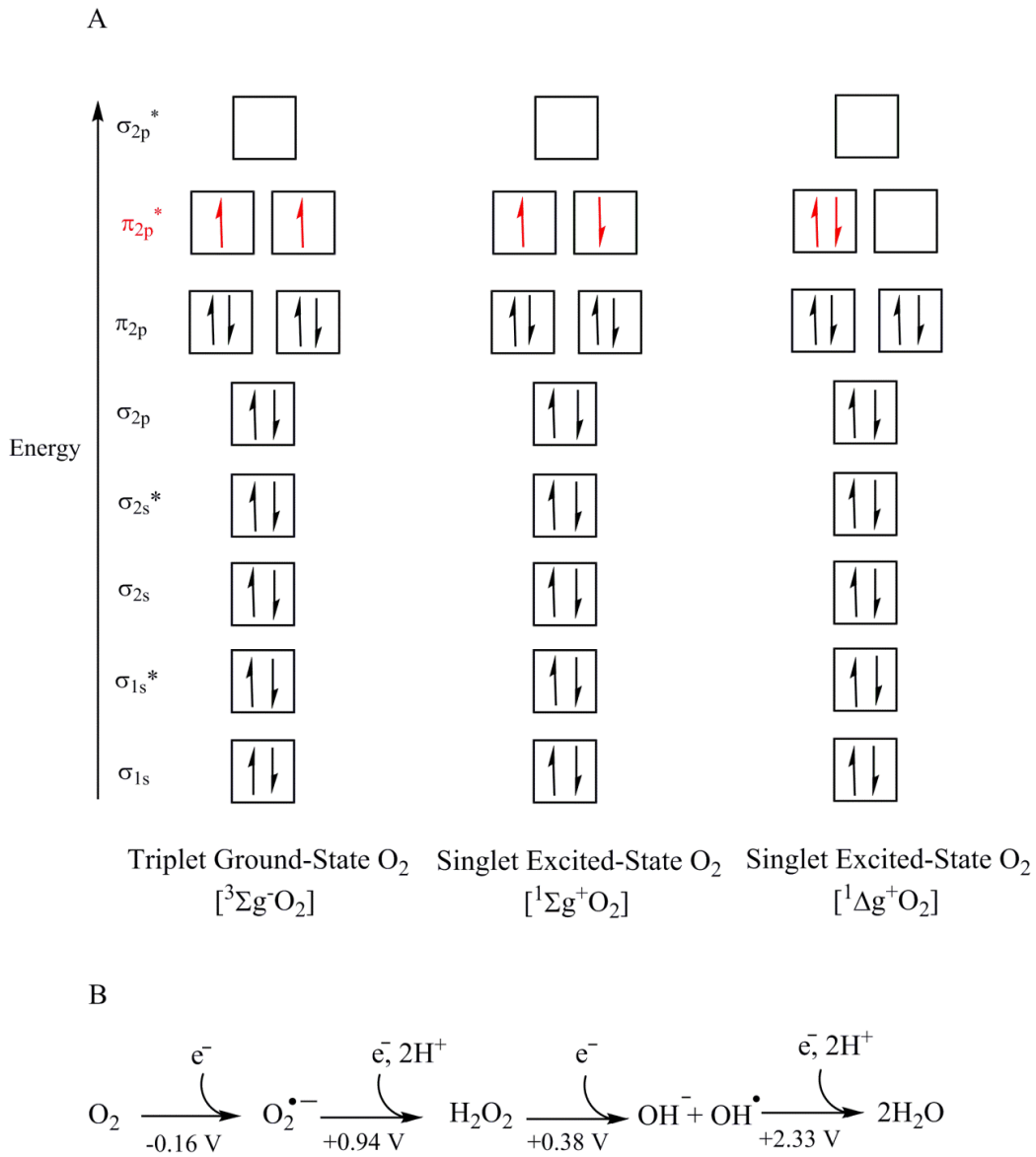

Figure 1.1. Molecular orbital diagram for triplet ground state of O_2, and its two excited singlet states (A). The four electron-reduction of molecular O_2 to water with standard (pH 7) reduction potentials for each one-electron step are indicated (B).

transition metal-catalyzed processes, partially reduced oxygen species ($O_2^{\bullet-}$, H_2O_2, and $OH^{\bullet}$) along with related derivatives (peroxyl and alkoxyl radicals) are termed reactive oxygen species (ROS) because of their capacity to react rapidly and indiscriminantly to achieve full reduction to water (Fig. 1.1 B) [1]. The collateral consequences of these reactions are observed by the modification of biomolecules of all types.

1.2. ROS: Sources, Biomolecular Alteration, and Mechanisms of Detoxification

All organisms that live in aerobic environments (whether or not they themselves use O_2) must confront the problem of ROS to one extent or another. The use of O_2 as a terminal electron acceptor in oxidative phosphorylation produces numerous opportunities for premature and incomplete O_2 reduction. Although ROS are used to some extent in signaling and regulation, especially of cellular redox status and redox processes, their accumulation holds damaging consequences for every class of biological molecule [1, 6]. Indeed, it appears that nature has taken note of the toxicity of ROS. Higher eukaryotes in particular rely on ROS for antimicrobial defenses. The oxidative burst of neutrophils is an example of this phenomenon [7]. The effect of ROS depends on both their identity and their relative concentrations. The following section will focus on different types of ROS, their origin, effects on biological systems, and how they can be detoxified.

1.2.1. Superoxide ($O_2^{\bullet-}$)

Superoxide ($O_2^{\bullet-}$) is the primary gateway for the generation of most if not all other ROS, and it is formed from the single electron reduction of O_2 (Fig. 1.1 B). There are numerous sources for the endogenous formation of $O_2^{\bullet-}$, but perhaps the largest contributor is mitochondrial or aerobic prokaryotic respiration. During cellular respiration, electron carriers like fully reduced flavins, flavin semiquinone radicals (Fig. 1.2), and transition

metal complexes of the electron transport chain occasionally reduce O_2 to form $O_2^{\bullet-}$. This circumvents the full four-electron reduction of O_2 at the cytochrome oxidase Cu/heme a_3 reaction center [1, 6, 8, 9].

Flavin (FAD or FMN)-dependent proteins are ubiquitous in metabolism. The flavins can accommodate a number of intermediate/redox states (Fig. 1.2). Most commonly, the fully oxidized states (FAD or FMN) can be reduced by a single electron to yield the flavosemiquinone radical. A second one-electron reduction produces the fully reduced ($FADH_2$ or $FMNH_2$) states. Reduced flavins react rapidly with O_2 to form an initial flavin peroxyl radical capable of a variety of chemical transformations, not the least of which is the formation of $O_2^{\bullet-}$ (Fig. 1.2) [8, 10].

Superoxide has consistently been observed to originate from the respiratory chain at complexes I and III. The most abundant source of $O_2^{\bullet-}$ is O_2 reduction by complex I $FMNH_2$ (or $FMN^{\bullet-}$) rather than electron transfer to the appropriate Fe/S cluster [6, 8, 10, 11]. Another common source of $O_2^{\bullet-}$ comes from the reduction of O_2 by the ubiquinone semiquinone radical at complex III [10].

Photosystems I and II (i.e., PSI and PSII) located in the thylakoid membrane are also known for their contribution in the generation of $O_2^{\bullet-}$ in plants, cyanobacteria, and algae during photosynthesis [12-14]. For example, in PSI the transfer of electrons from plastocyanin to ferredoxin also produces $O_2^{\bullet-}$. More so, the incomplete oxidation of water may result to the "leaking" of electrons from PSI which may subsequently react with O_2 to form $O_2^{\bullet-}$ [12]. Further, in PSII the excited energy transferred from chlorophyll P700 electron donor to its electron acceptors can also result in the formation of singlet $^1O_2$ [13].

Superoxide readily oxidizes Fe/S clusters, and therefore has the ability to interfere with

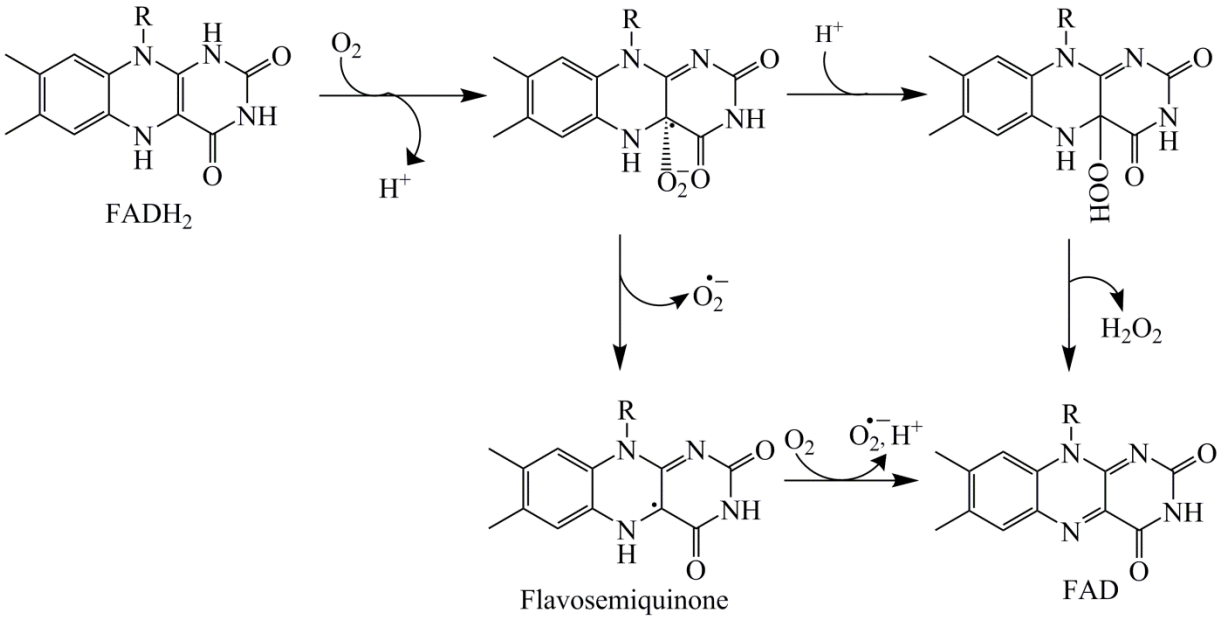

Figure 1.2. Flavoproteins contribution in the generation of ROS. Autoxidation of $FADH_2$ in flavoproteins [15].

a wide range of metabolic pathways [16, 17]. The Fe is readily detached from the cluster during Fe/S cluster inactivation, a process that occurs very rapidly with rate constants of 10^6-10^7 $M^{-1}s^{-1}$ [18]. Interestingly, the release of iron in this manner has the capacity to induce further destruction as uncontrolled Fe is able to catalyze the generation of additional ROS. Further, $O_2^{\bullet-}$ also inactivates catalase and glutathione peroxidase, and as such has the ability to interfere with subsequent steps in ROS detoxification.

There are two consequences of superoxide-based production and damage. One is that some organisms capitalize on the destructive nature of ROS to build defensive responses against hostile invaders. The second is that there are enzymatic defensive systems to prevent the accumulation of $O_2^{\bullet-}$. The former occurs in the context of the host-defense pathogen interaction. One of the efficient modes of defense against invading microorganisms is the rapid release of ROS (especially $O_2^{\bullet-}$) from various cell types during respiratory burst. The ROS are crucial weapons for the host. Membrane-bound NADPH oxidase is used by neutrophils and macrophages to generate copious amounts of $O_2^{\bullet-}$ [19]. Also, the primary source of ROS in NADPH oxidase is predominantly expressed in phagocytes. The ROS generated in this manner is strictly controlled to prevent further damage to neighboring tissues [7]. The superoxide formed is converted enzymatically to H_2O_2 by superoxide dismutase. The H_2O_2 produced in this manner plays an integral role in killing invading pathogens. First, it can participate directly in the oxidation of pathogen DNA, lipids and proteins [20]. More than this, H_2O_2 is used by myeloperoxidase to generate HOCl, a potent bactericidal agent. These systems are not without their consequences. Indeed, the ROS and other reactive species derived from phagocytes have recently been shown to be involved in the development of numerous chronic conditions connected to chronic inflammation,

including many cancers, coronary artery diseases, and diabetes [21].

Superoxide once formed can only proceed to form other ROS. More importantly, these are potentially more destructive ROS like H_2O_2 and $^{\bullet}OH$. Not surprisingly, these are often iron (or other redox transition metal)-catalyzed reactions. An example is the Fe-catalyzed Haber-Weiss reaction (**Eqn. 1.1**).

$$Fe^{3+} + O_2^{\bullet -} \longrightarrow Fe^{2+} + O_2 \qquad \textbf{(1.1)}$$

$$Fe^{2+} + H_2O_2 \longrightarrow Fe^{3+} + OH^- + OH^{\bullet} \quad \text{(Fenton Reaction)}$$

$$O_2^{\bullet -} + H_2O_2 \longrightarrow O_2 + OH^- + OH^{\bullet} \qquad \text{(Net Reaction)}$$

In terms of defenses against $O_2^{\bullet -}$ based molecular damage, McCord and Fridovich first isolated a blue Cu-containing protein (erythrocuperin) from bovine erythrocytes with the ability to scavenge $O_2^{\bullet -}$ [22]. The $O_2^{\bullet -}$ scavenging enzymes, later called superoxide dismutases (SODs), are all metalloenzymes and they are produced by all aerobic organisms. They catalyze $O_2^{\bullet -}$ disproportionation to form H_2O_2 and O_2. The rate constant for the uncatalyzed $O_2^{\bullet -}$ dismutation is optimal at a pH of 4.5 (2×10^7 $M^{-1}s^{-1}$) and decreases to 5×10^5 $M^{-1}s^{-1}$ at pH 7.0. Under the latter conditions, SOD produces a rate constant of about four orders of magnitude higher (i.e., 1.6×10^9 $M^{-1}s^{-1}$) which is at the diffusion limit [23].

The three main types of SOD are classified based on their protein fold and metal cofactor [23] (Fig. 1.3). Copper-Zinc SOD is a homodimer, found primarily in prokaryotes and mammals and is found in the cytoplasm [24]. The Cu ion is ligated by the imidazole side chains of four histidine residues and one water molecule. One of the His ligands to the Cu also ligates the Zn ion which is also coordinated to two other histidines and an aspartate (Fig. 1.3 A).

A

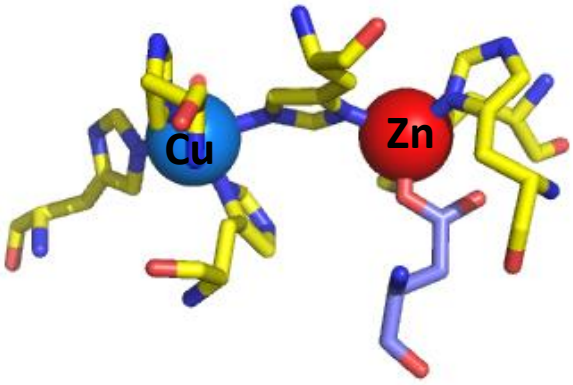

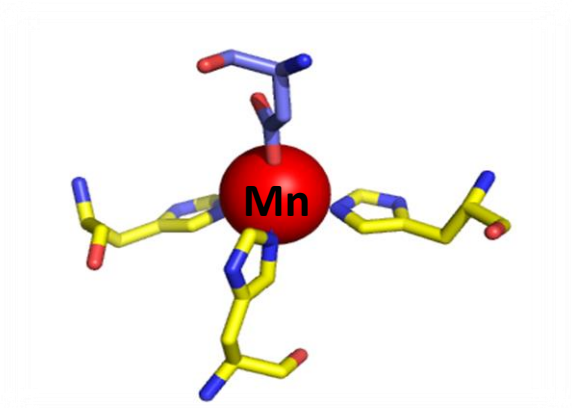

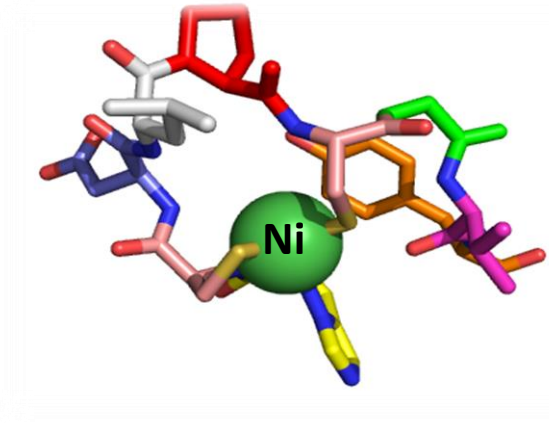

B C

Figure 1.3. Active sites of three types of SODs; Cu/Zn-SODs (A), Fe or Mn-SOD (B), and Ni-SOD, (C). Amino acids are colored as follows: Histidine-Yellow, Aspartate-Tv_blue, Tyrosine-Orange, Glycine-Green, Cysteine-Light Magneta, Valine-Purple, Proline-Red, Leucine-Gray. Amino acid oxygen and nitrogen elements are colored in red and blue, respectively. Structures were taken from PDB accession domain 1SDY [25], 2BPI [26], and 1Q0D [27] respectively.

Together, Fe-SOD and Mn-SOD constitute a second type of SOD found in prokaryotes, protists and in eukaryotic mitochondria and chloroplasts [28]. These SODs are dimers or tetramers. The mononuclear metal center is ligated by three histidines, one aspartate and either H_2O or OH^- depending on the oxidation state of the metal (Fig. 1.3 B). The Fe-SODs are found in the chloroplasts of plants while the Mn-SODs are found in mitochondria and several bacteria.

Finally, Ni-SOD constitutes the third type of SODs found primarily in prokaryotes [29]. They are mainly hexamers, each constituting an N-terminal hook that chelates the Ni ion. The Ni cycles between the +2 and +3 states for its catalytic activity. A conserved proline provides the hook by forming a sharp bend in the polypeptide chain. Also, two cysteines, one histidine and the amine of the N-terminus provide the ligands for the Ni cofactor [29]. All SODs, regardless of metal cofactor follow the same general sequence for $O_2^{\bullet-}$ disproportion (**Eqns. 1.2** and **1.3**).

$$M^{(n+1)}\text{-SOD} + O_2^{\bullet-} \longrightarrow M^{n+}\text{-SOD} + O_2 \qquad \textbf{(1.2)}$$

$$M^{n+}\text{-SOD} + O_2^{\bullet-} + 2\,H^+ \longrightarrow M^{(n+1)}\text{-SOD} + H_2O_2 \qquad \textbf{(1.3)}$$

where M = Cu, n = 1; Mn, n = 2; Fe, n = 2, Ni, n = 2.

1.2.2. Hydrogen Peroxide (H_2O_2)

Not only is $O_2^{\bullet-}$ destructive in its own right, but it leads to formation of other ROS (Fig. 1.1 B). Prominent among these is H_2O_2. Interestingly, the SOD defense against $O_2^{\bullet-}$ does not resolve the problem of H_2O_2 accumulation or its downstream consequences. There are multiple mechanisms for H_2O_2 generation: enzymatic and non-enzymatic, radical and non-radical. Oxidation of compounds can lead to the direct production of H_2O_2 as catalyzed

by numerous oxidases [9]. For example, the oxidation of alcohols to aldehydes by alcohol oxidase enzymes may also produce it as a byproduct [30]. Interestingly, in *E. coli* a flavin-dependent l-aspartate oxidase (NadB) contributes about one fourth of the H_2O_2 generated inside the cell [31]. A source of H_2O_2 in plant chloroplasts is PSI where it is generated by direct reduction of O_2 [32].

As mentioned before, H_2O_2 will also be produced as a result of any reaction (enzymatic or non-enzymatic) that generates $O_2^{\bullet-}$ because $O_2^{\bullet-}$ rapidly disproportionates to form H_2O_2 and O_2. Superoxide dismutase only catalyzes the reaction so it does not remove but instead hastens the generation of H_2O_2.

Like oxygen, Hydrogen peroxide is also widely known as a double-edge sword. At lower concentrations, it can be used in signal transduction pathways. It is also critical in the host immune responses of higher eukaryotes [31, 33]. On the other hand, at higher concentrations, it has been shown to directly inactivate numerous proteins. The proteins most sensitive to H_2O_2-dependent inactivation rely on redox active transition metals (e.g., Fe/S proteins) [34, 35]. As stated earlier, in the context of immune responses for higher eukaryotes, NADPH oxidase produces superoxide which disproportionates to H_2O_2. The H_2O_2 produced can be used by myeloperoxidases and lactoperoxidases to oxidize halides and pseudohalides (e.g., chloride and thiocyanate) to generate the corresponding hypohalous acids (e.g., HOCl and HOSCN) [33, 36]. These are powerful oxidizing and halogenating agents widely known for their bactericidal properties and their role in the innate immune response. Indeed, the H_2O_2 generated in this manner plays an integral role in the interaction of hosts and the pathogens that seek to colonize them.

Given its central position in the generation and consequences of ROS in biological

systems, it is not surprising to find that nature employs a diverse array of enzymes to safely remove H_2O_2. These enzymes can be divided into two main categories, catalases and peroxidases [37]. Catalase and/or peroxidase activity can be produced by a number of strategies including cysteine-dependent (e.g., alkyl hydroperoxide reductase [AhpC]), selenocysteine-dependent (e.g., glutathione peroxidase and NADPH peroxidase) [38, 39], and transition metal-dependent (e.g., manganese catalases) mechanisms [40]. However, as will become clear in subsequent sections of this review, one of the most widely exploited cofactors for diffusing the threat posed by H_2O_2 is heme [41]. As with superoxide, H_2O_2 is a formidable and destructive oxidant in its own right, but it is more prominently a precursor to far more destructive oxidants (Fig. 1.1 B).

1.2.3. Hydroxyl Radical ($HO^{\bullet}$)

The hydroxyl radical is an indiscriminant oxidant ($E^{o'}$ = +2.33 V) that reacts at diffusion-limited rates with all classes of biological molecules including nucleic acids, lipids, amino acids, and carbohydrates (Fig. 1.4) [6, 31, 42, 43]. The primary mechanism of $^{\bullet}OH$ radicals generation is one-electron H_2O_2 reduction facilitated either by reaction with reduced transition metals (e.g., Fe^{II} of the Fenton reaction) or by exposure to ionizing radiation (**Eqn. 1.1**) [42, 44].

There are virtually no kinetic or thermodynamic barriers to $^{\bullet}OH$ reduction by any class of biological molecule. It has an extremely short lifetime which means that its site of reduction is likely to be very close to its site of generation. In this respect, it is the location of redox active transition metals and the site of H_2O_2 generation that are predominant factors in determining where damage by $^{\bullet}OH$ is most likely to be observed. This is also the point where enzyme/protein based defenses are deployed as enzymatic strategies against $^{\bullet}OH$

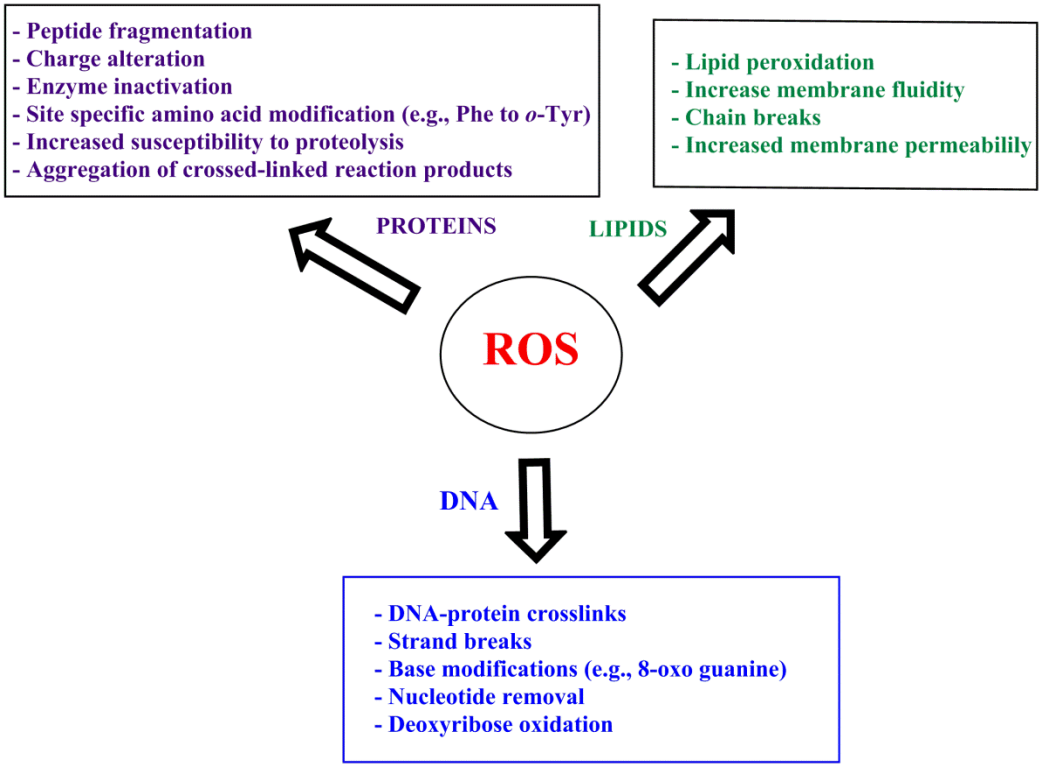

Figure 1.4. Potential molecular damage caused by ROS to all classes of biological molecules.

must be preventive. As there is no real kinetic barrier to $^{\bullet}OH$ reaction once formed, there is little point in enzyme-based systems to reduce it. Rather, sacrificial radical scavengers (e.g., ascorbate, flavonoids, tocopherols, etc.) are the only viable strategy to diffuse $^{\bullet}OH$ once generated. **1.3. Defense Mechanisms Against H_2O_2**

The need to detoxify H_2O_2 is made even more urgent in the context of a pathogen facing host defenses. Superoxide rapidly disproportionates due to the lower pH of the environments where it is generated and the action of SOD. The H_2O_2 produced especially by phagocytic leukocytes is used by myeloperoxidase to generate HOCl, a central weapon of defense immunity for the host. During oxidative stress, aerobic organisms require systems to fight and survive the threat posed by ROS. For the purpose of this research, we will focus our discussion on strategies nature has employed to eliminate H_2O_2. As mentioned before, heme is the most widely used cofactor by enzymes to eliminate the threat posed by H_2O_2.

Two broad categories to detoxify H_2O_2 are catalase and peroxidase mechanisms. Catalases are enzymes which catalyze the decomposition of H_2O_2 to water and oxygen ($2\ H_2O_2 \rightarrow 2\ H_2O + O_2$). In contrast, peroxidases catalyze the reduction of various peroxides with a vast array of electron donors ($H_2O_2 + RH \rightarrow 2\ H_2O + 2\ R^{\bullet}$). In both categories, the catalyst represented can be divided into heme-dependent and non-heme cofactor dependent mechanisms.

1.4. Catalases

Catalases are ubiquitous in nature, found throughout eubacteria, many archaebacteria, and across all major groups of eukaryotes [45]. A small group found only in selected eubacteria and archaea relies on a dinuclear manganese center for its catalase activity [40, 45]. Given the wide distribution of heme-dependent catalases, it begs the question as to why

there might be this completely distinct approach for catalatic H_2O_2 decomposition. Factors that may have influenced their emergence and persistence in nature include the enzyme's thermostability, and resistance to ligands like cyanide [40]. It may also coincide with a lower peroxide stress for the organisms known to carry it. Their catalase reaction cycle contrasts that of heme-dependent catalases in that there are no free radicals involved, there are no reactive intermediates in their cycle, and both water molecules from H_2O_2 reduction are formed during the first step of the reaction [40, 45, 46].

1.4.1. Heme-dependent Catalases

Heme-dependent catalases are far more widely distributed in nature [45]. These monofunctional (i.e., typical) catalases are homotetramers where each subunit bears a heme prosthetic group. In most catalases, heme *b* is used though heme *d* is observed in a handful of enzymes [45]. The heme iron is coordinated by a tyrosine phenoxide anion as its proximal [1]ligand. The anionic character of the ligand produces a very negative Fe^{III}/Fe^{II} reduction potential for the heme. As such, catalases are isolated in the ferric state, and they are also capable of stabilizing higher iron oxidation states (i.e., Fe^{IV}=O) [47, 48]. On the distal side of the heme are an invariant histidine, asparagine and serine (Fig. 1.5 A). The distal histidine imidazole plane is roughly parallel to the heme. This residue binds H_2O_2 through a hydrogen bond network. The distal histidine is proposed to serve as the general base to abstract a proton from hydrogen peroxide during compound I formation [47, 48]. The distal asparagine stabilizes the negative charge which develops on the distal O as the O-O bond is polarized and heterolytically cleaved (Fig. 1.6). The serine residue participates in a hydrogen bond

[1] By convention, the side of the heme where the protein-based ligand coordinates the iron is referred to its proximal side (Px).

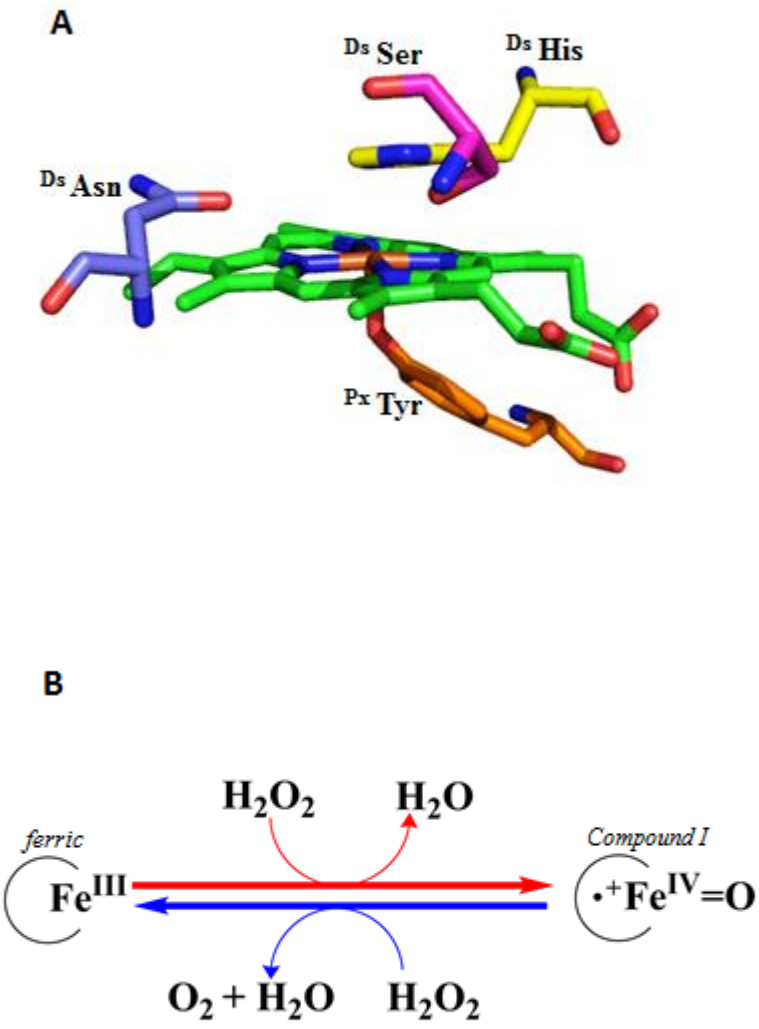

Figure 1.5. Active site of heme-dependent catalases showing four conserved residues (A) and the simplified catalytic cycle of monofunctional catalases (B). The structure image was generated from coordinates deposited under PDB accession domain 1IPH [49]. Ds (distal side of heme).

with the N^{δ} of the imidazole and increases its nucleophilicity hence stabilizing the heme pocket for facile H_2O_2 oxidation [47, 48]. For compound I reduction, the distal histidine has been proposed to act as an acid-base catalyst to oxidize H_2O_2 for facile release of O_2 and H_2O [50]. Together, these four residues help all monofunctional (or typical) catalases to perform their catalytic mechanism. The catalase cycle is a two-step mechanism where H_2O_2 acts first as an oxidant and then a reductant [45, 47, 48, 51, 52]. The ferric enzyme reacts with the first equivalent of H_2O_2 to form compound I and H_2O. For the second step, H_2O_2 is oxidized and compound I is reduced back to the ferric enzyme, releasing O_2 and H_2O (Fig. 1.5 B). All heme-dependent monofunctional catalases show a broad plateau for pH optimum in catalase activity. Hence, these enzymes have the ability to degrade H_2O_2 over a wide range of pH (i.e., pH 5-10) values.

Ferryl (Fe^{IV}=O) heme states are well known for their reactions with different peroxides and electron donors. Though they also form Fe^{IV}=O states, catalases are very limited in these kinds of reactions. One important feature of the typical (i.e., monofunctional) catalases is that the heme is deeply buried within the protein 20 Å from the closest surface [47]. A very narrow access channel for catalases leads to the active site heme and only allows passage of small molecules like H_2O_2 and ethanol to enter. However, large molecules like most peroxidatic electron donors are not able to access the active site. This is one prominent reason why catalases generally show poor peroxidase activity.

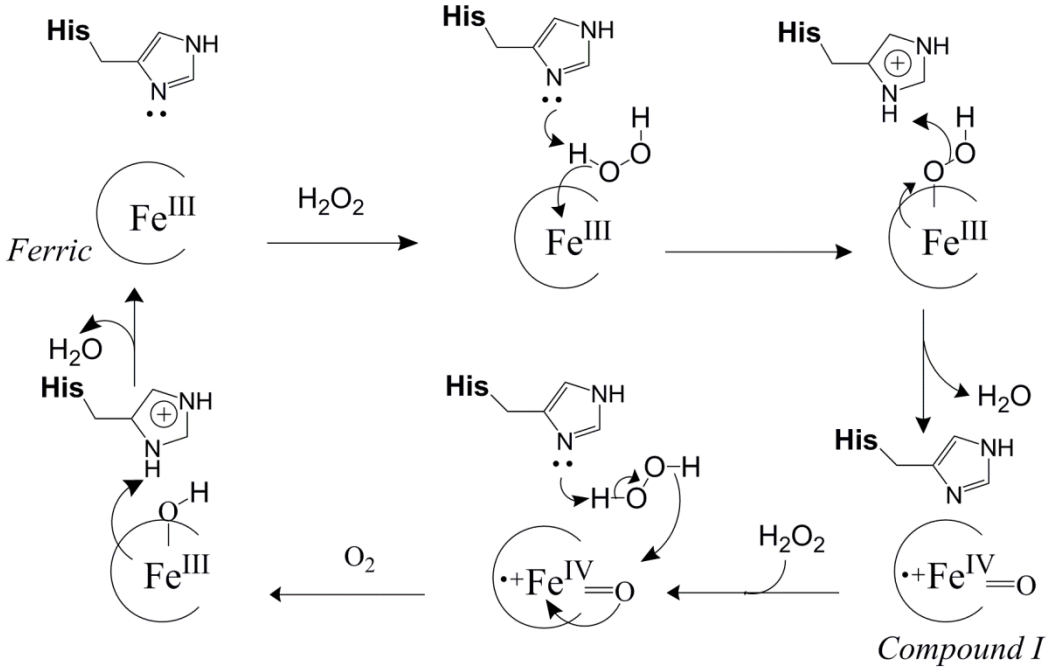

Figure 1.6. Classical reaction mechanism of heme-dependent monofunctional catalases [50].

Though there are distinctive features among them, the heme-dependent catalases all have a common fold. It consists of a core beta barrel domain, an alpha-helical domain, an N-terminal arm domain, and a "wrapping loop". The latter is a long protein segment that links the two globular domains (Fig. 1.7 B). This loop bears the proximal tyrosine ligand. The β barrel is the main feature of the catalase fold, and it constitutes an 8-stranded antiparallel β barrel that also contains about six α helices. The barrel is preceded by an extended N-terminal arm followed by the wrapping loop and terminated by the second globular domain (i.e., α helical domain). The first half of the barrel is situated at the distal side of the heme which constitutes strands β1 to β4. The second half of the barrel contributes to the NADPH binding domain for those enzymes that require NADPH and spans from strands β5 to β8 [53].

Despite the broad structural similarities between catalases, they are divided into three main clades based on sequence and structural distinctives [51]. Clade 1 enzymes are found in eubacteria, algae, and plants are characterized by a relatively small subunit size (55-69 kDa) [54]. They use heme *b* as their prosthetic group. Catalase CatF from *Pseudomonas syringae* is a typical example of a clade 1 catalase (Fig. 1.8 A) [54]. Clade 2 catalases found in eubacteria and fungi have a considerably larger subunit, (75-84 kDa). They use heme *d* as their prosthetic group (Fig. 1.8 B). The extra mass is contributed by a "flavodoxin-like" domain similar to the family of the type 1 glutamine amidotransferases (Fig. 1.8 B) [52]. Heme *d* is a derivative of heme *b* where one of its propionate side chains has been converted to a cis-hydroxy-γ-spirolactone, and the corresponding pyrrole ring C has lost the double bond between the outer C-6 position and the hydroxyl group of C-5 [55]. In addition, clade II enzymes also form a covalent modification between the $^{\beta}$C of the proximal Tyr ligand and

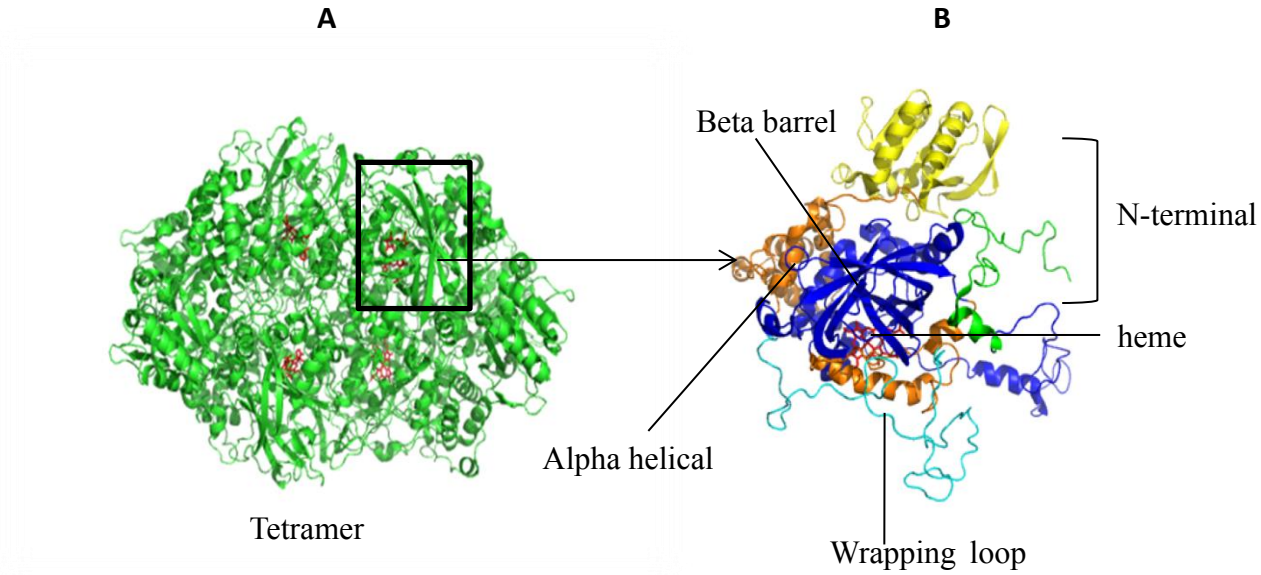

Figure 1.7. The multimeric structure (A), and the subunit (B) of *E.coli* HPII catalase. The globular beta barrel domain (Yellow), alpha helices (Green), and wrapping loop (Cyan). Structures were taken from PDB accession domain 1IPH [49].

the $^{\delta}$N from the imidazole group of the distal His [52, 56]. Catalase HPII from *E. coli* is an example of a clade 2 catalase (Fig. 1.8 B) [49, 52]. Clade 3 enzymes are the most widely distributed of the three. They are found in archaea, eubacteria, fungi, protists, plants, and animals [53]. They are highly similar to clade 1 catalases, especially in the use of heme *b* as their prosthetic group, and they also have a relatively small subunit size (43-75 kDa). They contrast other clades in that they bind NADPH as a second redox active cofactor (Fig. 1.8 C). The NADPH cofactor binds about 20 Å from the active site, but it is not directly required for catalatic turnover. It is proposed that NADPH serves as a reductant to restore catalase-inactive intermediates to the Fe^{III} state and maintain catalatic activity [51, 53]. Examples of clade 3 catalases include bovine liver catalase and human erythrocyte catalase [35, 53, 54].

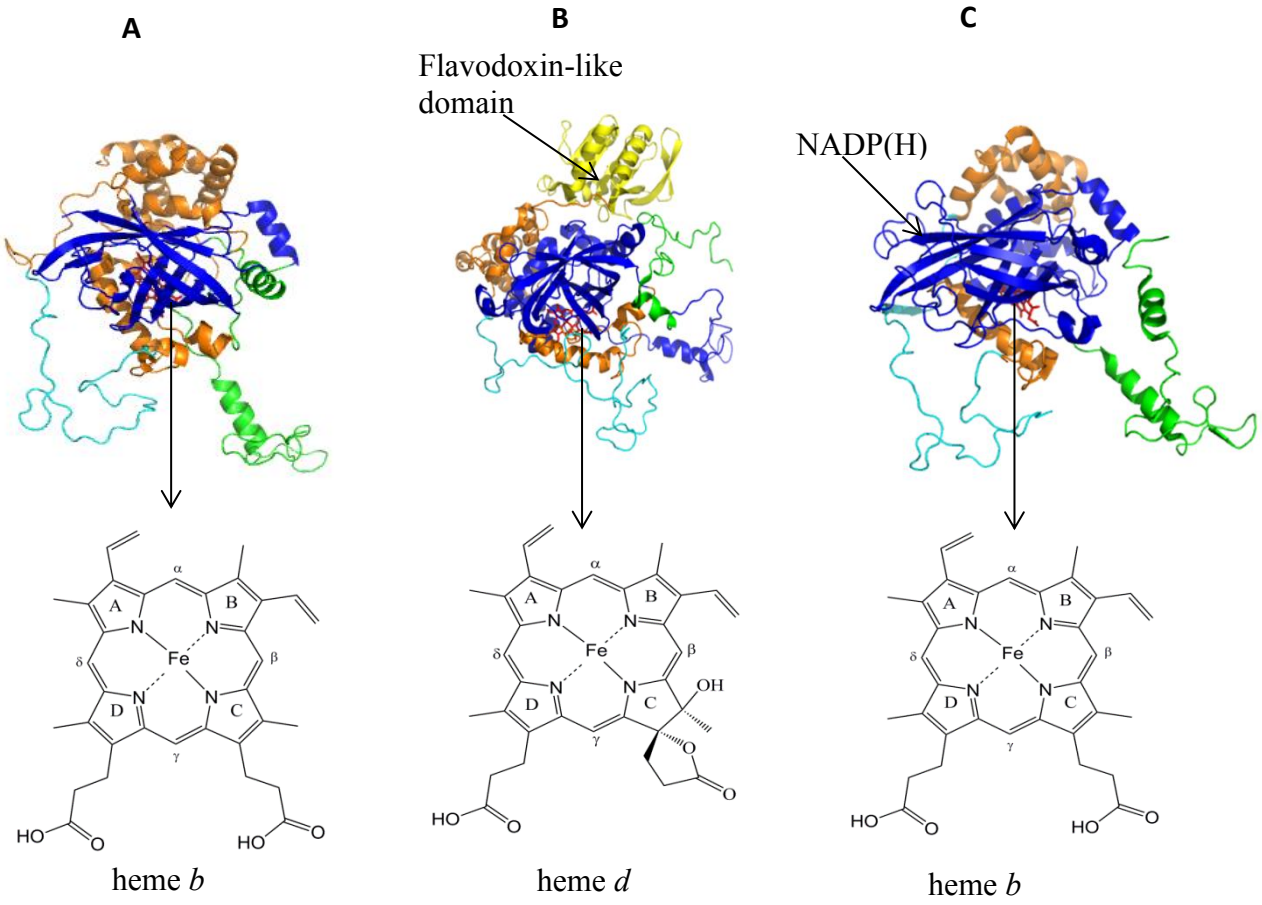

Figure 1.8. Catalase fold structures for representatives of three clades of heme-dependent catalases. CatF (clade 1) (A), HPII (clade 2) (B), and human erythrocyte catalase (clade 3) (C). Structures were constructed from PDB accession numbers 1M7S [54], 1IPH [49] and, 1QQW [57] respectively.

1.5. Peroxidases

In contrast to the H_2O_2 disproportionating activity of catalases, enzymes which utilize different peroxides as electron acceptors to catalyze a wide range of oxidative transformations are generally referred to as peroxidases. These enzymes are found in all classes of living organisms. As with catalases, they can be divided into two groups depending on whether or not they use heme as cofactor. The non-heme members can be divided into five independent families [58]. These include the thiol peroxidases (e.g., glutathione peroxidase and peroxiredoxines), alkylhydroperoxidases (AhpC), manganese catalases, NADPH peroxidases, and the non-heme haloperoxidases [38-40]. Most of them use FAD as cofactor and are capable of reducing lipid hydroperoxides, alkyl peroxides, and H_2O_2. It is noteworthy that the primary role of these enzymes is protection against oxidative stress; the identity of the oxidized electron donor is typically of secondary importance. Particularly in the context of prokaryotic organisms, these non-heme peroxidases are especially important for the disposal of endogenously generated H_2O_2. AhpC, for example, shows a very low k_{cat} and a very low apparent K_M for its H_2O_2 substrate. Consequently, it is very efficient, but it is also very easily overwhelmed. Thus, it is not likely to provide bacteria and other microorganisms sufficient defense against copious exogenous H_2O_2 generated by higher eukaryotes under threat of infection. As will be addressed later, heme-based H_2O_2 disposal systems are better positioned to address peroxide-based threats of this nature.

The heme containing peroxidases can be divided into four superfamilies. The first, previously known as the plant/fungal peroxidases or non-animal peroxidases is the peroxidase-catalase (Px-Ct) superfamily. The second, formerly known as the animal

peroxidases, is the peroxidase-cyclooxygenase (Px-Cx) superfamily. There are also the peroxidase-chlorite dismutase, and peroxidase-peroxygenase superfamilies [59]. The former two superfamilies are the largest and have the greatest bearing on the research presented in this dissertation, so they will be the focus of this literature review.

1.5.1. Animal Peroxidases (Peroxidase-Cyclooxygenases)

The peroxidase-cyclooxygenases were initially called mammalian peroxidases, but the emergence of other members in plants, fungi and bacteria warranted another nomenclature [58, 60, 61]. Though His-based ligation of the heme is common to both the Px-Cx and Px-Ct superfamilies, the modulation of the ligand by H-bonding is distinct. An Asn residue (rather than Asp in Px-Ct enzymes) H-bonds the proximal His producing more positive reduction potentials in the Px-Cx superfamily. Similarly, on the distal side of the heme, both superfamilies have a His and an Arg residue, but, Px-Cx enzymes also have a distal side Asp, Gln, and Met which are absent from the Px-Ct superfamily. A frequent, though not universal feature of Px-Cx members is the post-translation modification of the heme. Most commonly, ester linkages are established with Glu and Asp residues from the peroxidase protein. Another common though not universal feature of Px-Cx members is their oxidation of halide and pseudohalide substrates, leading to the generation of the corresponding hypohalite ions as products. Though all Px-Ct enzymes can oxidize at least some halides (e.g., I^-), this does not figure prominently in their physiological function. In contrast, hypohalite ion production by the Px-Cx enzymes myeloperoxidase (MPO), lactoperoxidase (LPO), and eosinophil peroxidase (EPO) is an essential component of innate immunity. Another Px-Cx member, thyroid peroxidase (TPO), leverages I^- oxidation towards the generation of triiodothyronine and thyroxine.

However, in this regard the most striking Px-Cx enzyme is MPO. MPO, a mammalian enzyme, is most abundant in neutrophils where it is stored in the cell's unique granules [60, 62]. It is also expressed to lesser extents in monocytes and some macrophages. MPO is a tetramer consisting of two light and two heavy polypeptide chains [62, 63]. These chains arise from the excision of a single polypeptide precursor. The chains are linked together by a disulfide bridge from a conserved Cys residue [62]. The heavy glycosylated chain contains the active site bearing the modified protoporphyrin IX heme. Also, a binding site for Ca^{2+} has been identified in the structure of MPO [62, 63]. The essential residues at the active site are the distal Arg239, Gln91, and His95. At the proximal side, H336 is the axial ligand which is also H-bonded with the carbonyl oxygen of Q421. The post-translational modification of rings A and C is a common, but not conserved feature for these enzymes (Fig. 1.9 B). Also, the vinyl group of ring A through its beta carbon forms a covalent association with the sulfur of a conserved methionine, a feature only unique to MPO [62, 63]. As would be anticipated, these modifications give rise to some unique spectral and redox features of MPO, hence its special catalytic abilities. Indeed, the Soret band for MPO is red shifted to about 425 nm along with very intense bands at the visible region giving the enzyme a unique green color [62].

Most, if not all peroxidases are capable of oxidizing I^- to OI^-. Fewer are able to oxidize Br^- to OBr^-, but MPO is unique among both the Px-Cx and Px-Ct superfamilies in its ability to oxidize Cl^- to OCl^- at the expense of H_2O_2 reduction, a fundamental part of the antimicrobial function of MPO in neutrophils. This special ability of MPOs has been linked to the presence of a third modification of the pyrolle ring A by a methionine. Also, MPO serves as a key mediator of molecular damage that accrues due to chronic inflammation with

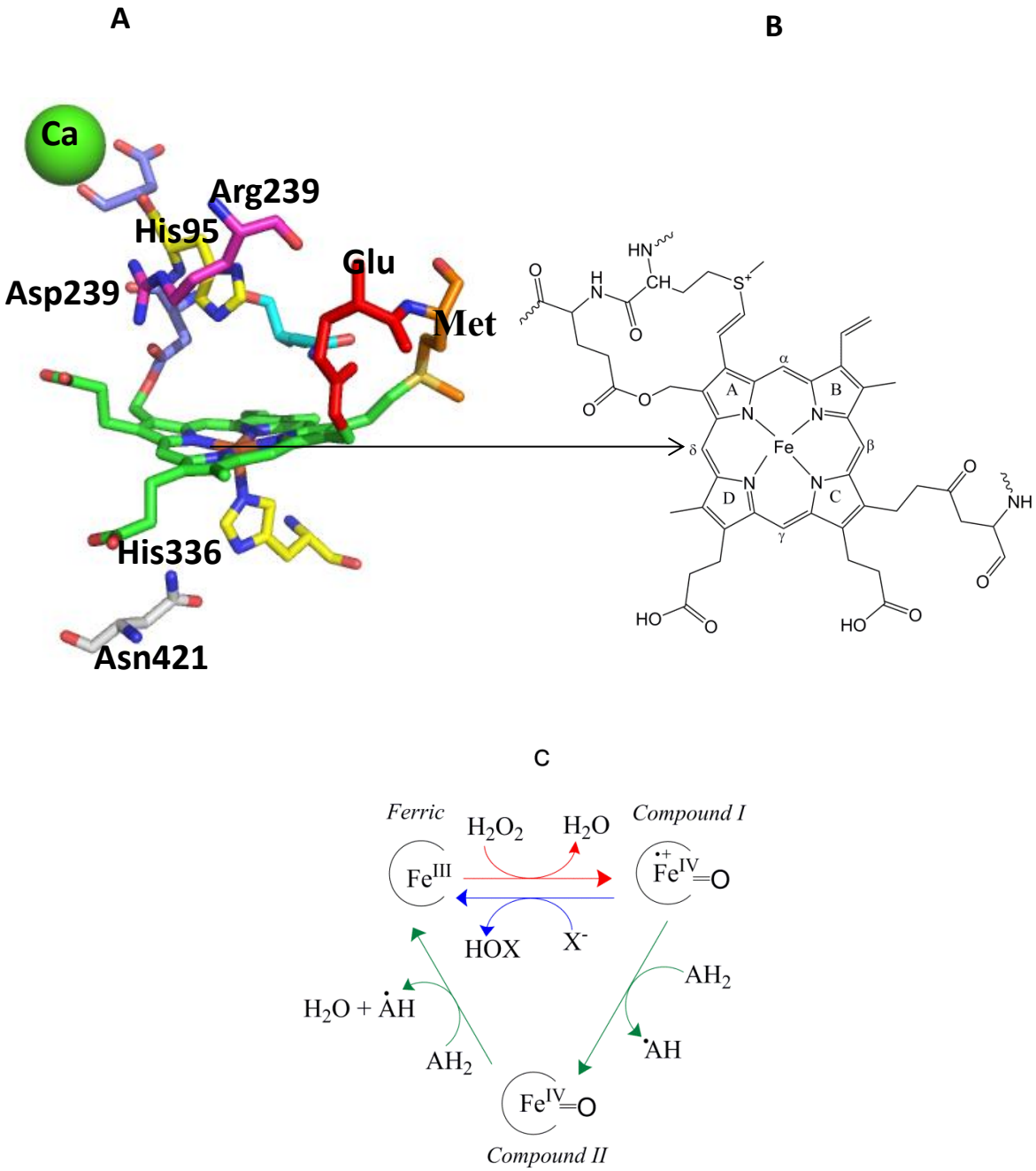

X^- (halide), XOH (hypohalous acid),
AH_2 (peroxidase reducing substrate)

Figure 1.9. Active site of mammalian myeloperoxidase (A), structure of modified heme in MPO, and catalytic mechanism of myeleoperoxidase (C). Amino acid oxygen and nitrogen elements are colored in red and blue, respectively. Ca^+ -green sphere. Structures were taken from PDB accession domain 1CXP [62].

respect to pathogenic bacteria. The presence of MPO substantially raises the stakes of H_2O_2 degradation. The failure of a pathogen to efficiently remove H_2O_2 exposes it to substantially greater damage from OCl^-.

The first step of the catalytic mechanism of MPO is similar to all heme peroxidases; the ferric enzyme reduces H_2O_2 to form compound I. However, an excess of peroxide is required to observe it. It has been proposed that the distal histidine and arginine assist in the first step where the H_2O_2 is oriented and bound to the ferric enzyme. This allows for the heterolytic O-O bond cleavage. Compound I oxidizes halides (Cl^- is unique to MPO) and several other peroxidatic electron donors (observed in most peroxidases) (Fig. 1.9 C). For the former cycle, compound I is reduced back to the ferric state by oxidizing a halide [62]. The latter cycle typical of peroxidases, compound I is reduced by the presence of peroxidatic substrates. It is hypothesized that the available substrate will determine what pathway dominates.

1.5.2. Px-Ct Superfamily: the Non-animal Peroxidases

This group represents the second superfamily of heme peroxidases. They are found predominantly in plants, fungi and bacteria [58, 61, 64]. All enzymes in this group have several structural similarities. Indeed, they all have a so-called peroxidase fold which is composed of 10 alpha helices (A-J) and little or no beta sheet (Fig. 1.10). The helical structure surrounding the active site heme is also quite distinct and comprises helices B, E, and F (Fig. 1.11). Within the active site, the heme is always heme *b*, and there are five residues invariant across the superfamily. These include the proximal histidine which is modulated through a strong H-bond to an Asp, the distal His modulated by an H-bond to an Asn, and the distal Arg (Fig. 1.12 A). All of these facilitate the peroxidase catalytic

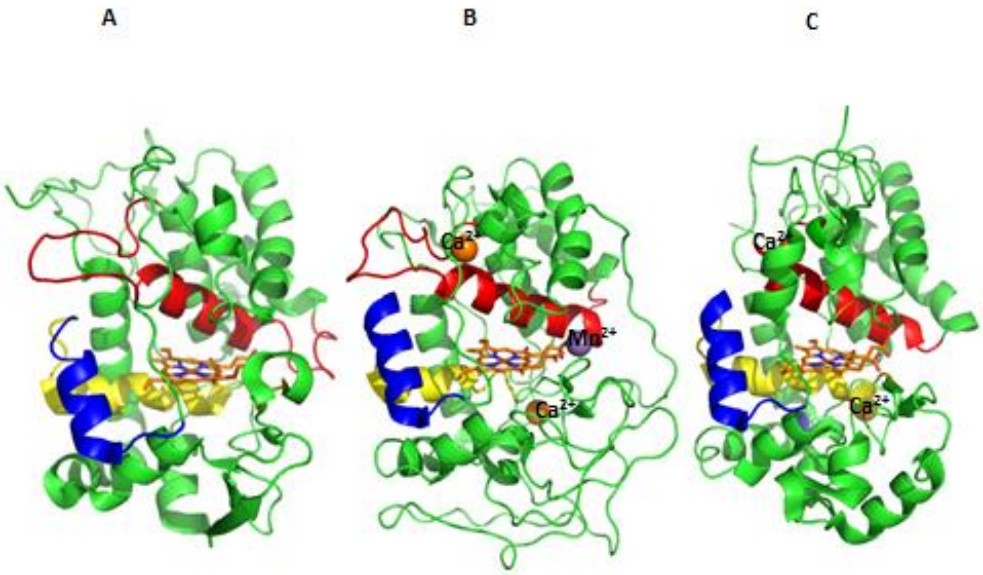

Figure 1.10. Ten helical structure representatives of the three classes of the Px-Ct superfamily. Cytochrome c peroxidase (class I) (A), manganese peroxidase (class II) (B) and horseradish peroxidase (class III) (C) are shown. Ca^{2+} ions are in orange while Mn^{2+} is shown in purple Structures constructed from PDB accession numbers 2CYP [65], 1MNP [66], and 1H5A [67] respectively.

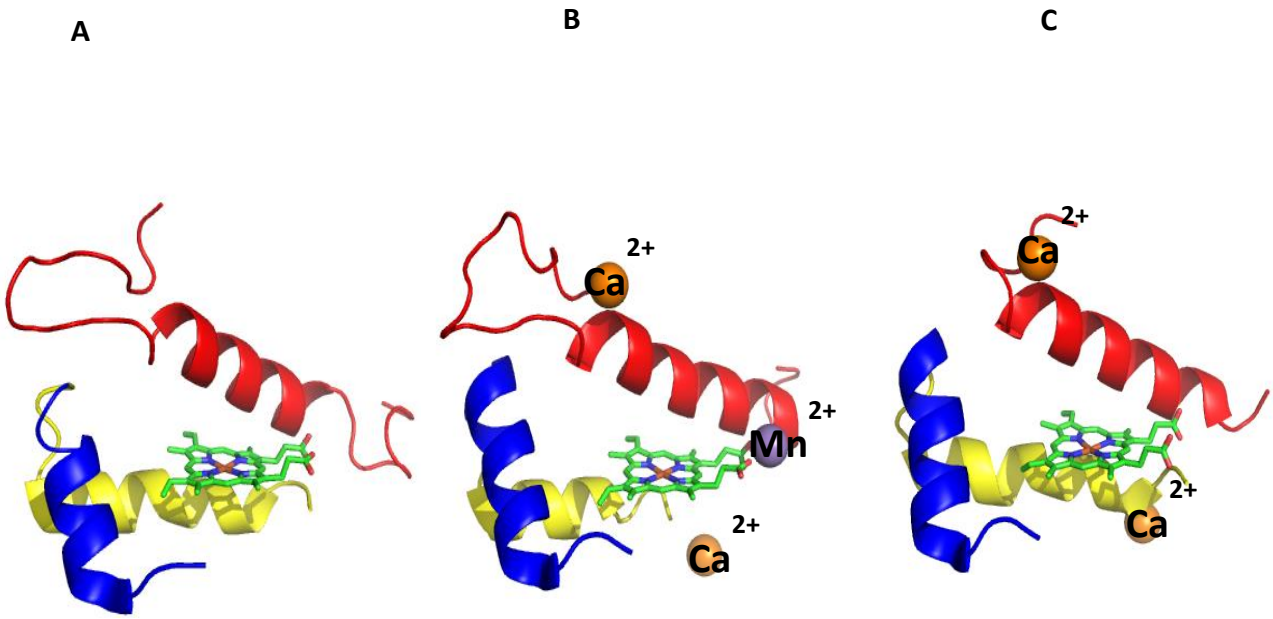

Figure 1.11. Three helix structures around the active sites of non-animal peroxidases. Helical structure of cytochrome c peroxidase (A), manganese peroxidase (B) and horseradish peroxidase (C). Helix B is shown in red, helix E is shown in yelow and helix F is shown in blue. Ca^{2+} are shown in orange while Mn^{2+} is shown in purple Structures were taken from PDB accession domain 2CYP [65], 1MNP [66], and 1H5A [67] respectively.

mechanism (Fig. 1.12 B).

Another important characteristic of peroxidases is that they have optimum activity at acidic pH (i.e., pH < 4.5) and relatively low concentrations of H_2O_2.

Since all non-animal peroxidase have similar active site residues, it is important to understand the basic structure of this type of active site and the intermediates it supports towards peroxidatic catalysis [68, 69]. The proximal His (H175 in CcP) serves as the ligand to the heme iron. The proximal Asp (D235 in CcP) through its hydrogen bond to the N^{δ} of the His ligand imparts a substantial anionic character to the imidazole (i.e., imidazolate) ligand. This produces a much lower reduction potential (-186 to -226 mV) compared to other histidine ligated hemes (e.g., myoglobin; + 50 mV). As such, peroxidases are consistently isolated in the ferric oxidation state, and they have the capacity to stabilize higher heme oxidation states (e.g., Fe^{IV}=O). The strictly conserved distal His (H52 in CcP) serves as a general base to facilitate the heterolytic cleavage of H_2O_2 to form H_2O and the Fe^{IV}=O porphyrin $\pi^{\bullet+}$ intermediate known as compound I [70, 71]. A strictly conserved Arg (R48 in CcP) in the distal cavity also facilitates heterolytic O-O bond cleavage by electrostatically offsetting the negative charge that accumulates on the distal oxygen as the initial peroxide complex, compound 0 (Fe^{III}-OOH), is converted to compound I. This mechanism was first put forward by Poulos-Kraut in 1980 (Fig. 1.13) [72]. Recent computational studies have revealed that the experimentally observed rates of compound I formation are not competent with the distance between the distal His and the heme iron. The distance cannot account for rapid enough H^+ transfer to support compound I formation. This problem could be resolved by conformational dynamics (i.e., may be the His can get closer than has been shown on the crystal structures). This seems unlikely because all

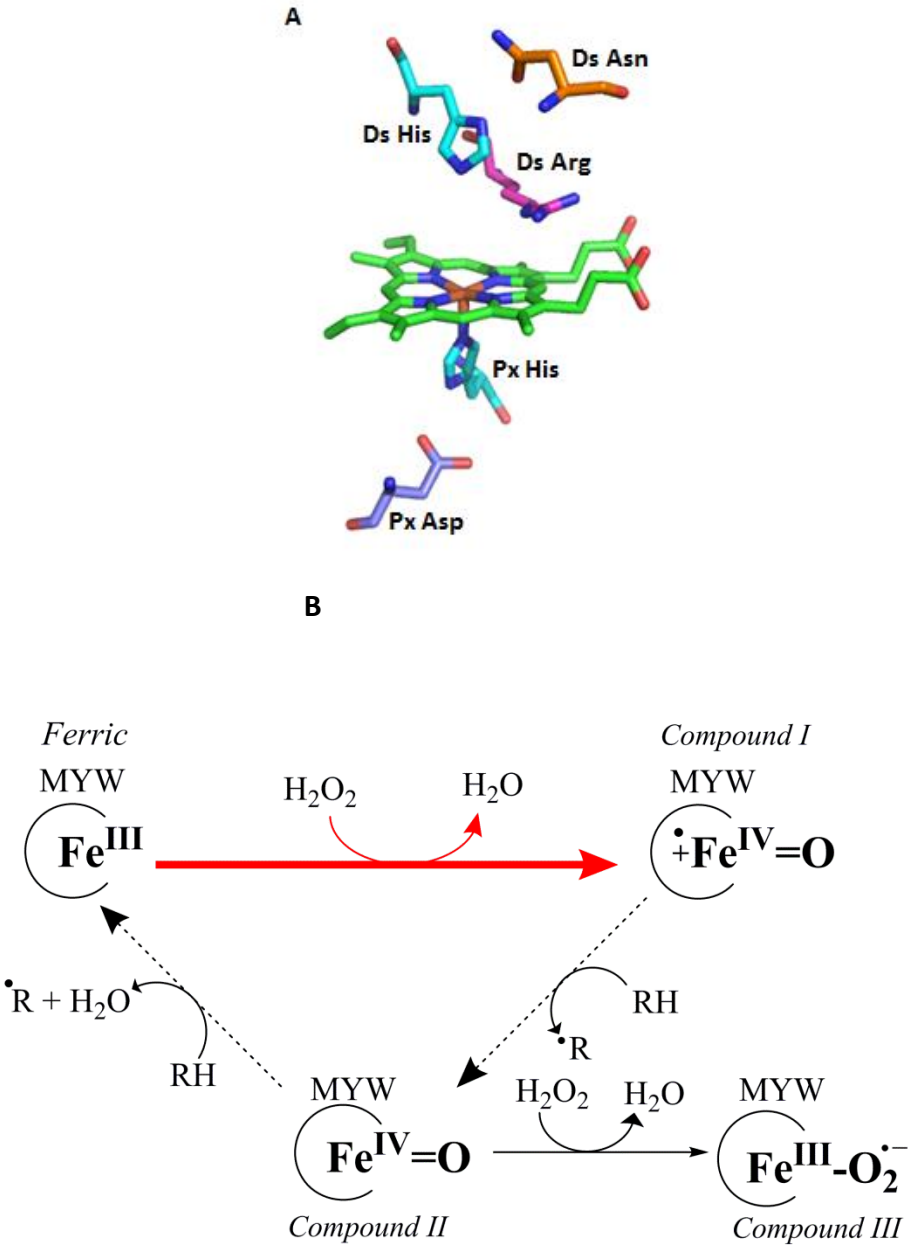

Figure 1.12. Active site of non-animal peroxidases showing five conserved residues and heme *b* prosthetic group (A) and simplified peroxidase cycle of non-animal peroxidases (B). R represents reducing substrates for various peroxides. Structure was taken from PDB accession domain 1H5A [67]. Px represents proximal side of heme while Ds signifies the distal side of heme.

indications are that the structure is rigid. The barrier was lowered by three fold when an intervening water molecule was added to serve as a H^+ relay from the peroxide to the distal histidine [73-75], accounting for the experimentally observed rates.

In contrast to catalases, compound I is reduced by two equivalents of peroxidase electron donors. A typical peroxidase completes its catalytic cycle by two sequential one-electron reductions (Fig. 1.12 B). Following the first reduction, the intermediate referred to as "compound II" is generated. The most common structure for compound II is a Fe^{IV}=O intermediate where the porphyrin radical is reduced prior to the ferryl center. Following the second electron reduction, the resting state is achieved. Thus, the return of a peroxidase to its ferric state generates two equivalents of an exogenous electron donor radical.

One important feature of typical peroxidase active site is that large aromatic electron donors have access to the δ-meso heme edge for rapid electron transfer to reduce these high oxidizing species to their resting form [68]. This site is the one which affords robust peroxidase activity [68, 69].

In the absence of peroxidase electron donors or if the electron donor concentration is very low, peroxidases are readily inactivated in the presence of excess H_2O_2 to generate a compound III (i.e., Fe^{III}-$O_2^{\bullet -}$) species (Fig. 1.12 B) [68, 69].

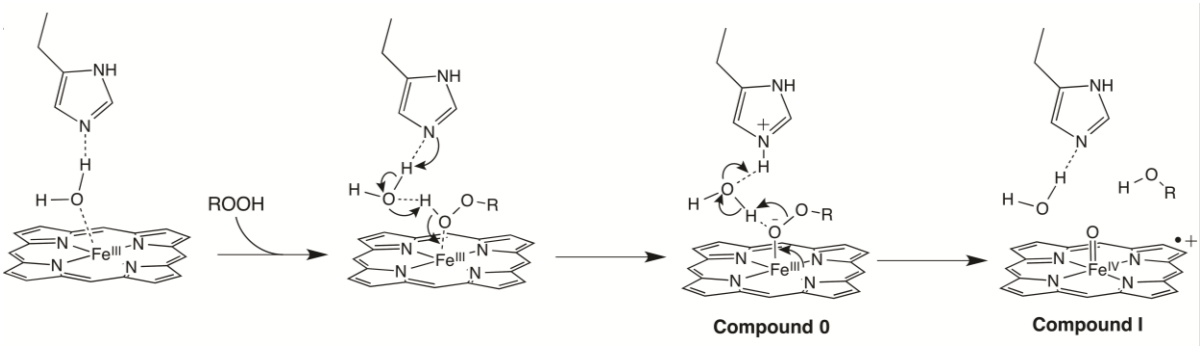

Figure 1.13. Catalytic mechanism of typical peroxidases including the Poulos Kraut mechanism for compound I formation.

Since the contours of the superfamily were first described in 1992, three subdivisions (classes) have been recognized (class I, II, and III) [59, 64]. Detailed sequence analyses reveal that all three classes originated from ancestral Negibacteria with transfer via endosymbiotic events to eukaryotic cells [59].

1.5.2.1. Class III peroxidases

These peroxidases are dominated by the plant secretory enzymes [64]. They are monomeric and glycosylated. The class III peroxidases have phenylalanines on the distal and proximal pockets of the heme which prevents intramolecular electron transfers within its active site.

Horseradish peroxidase (HRP), soybean, and guaiacol peroxidases are examples of class III peroxidases. HRP will be discussed extensively as a representative of class III enzymes because it has been extensively studied and characterize [76, 77]. It is a 44 kDa glycosylated protein with four disulfide bridges and two calcium ions are located around the active site and these stabilize its conformation [76, 77].

HRP plays an important role in the processes of the life cycle of plants such as auxin metabolism, lignin and suberin formation, cross-linking of cell wall components, defense against cell pathogens and cell elongation [68, 69]. It can also oxidize a wide range of substrates including phenols, aromatic amines, indoles, and sulfoxides.

1.5.2.2. Class II peroxidases

These are largely fungal secretory proteins with molecular weights between 41-46 kDa [59, 64, 78, 79]. Their apparent primary physiological function is to initiate the degradation of lignin in wood to CO_2 [80, 81]. Lignin, manganese, and versatile peroxidases are three enzymes secreted by *Basidiomycetes* (white rot fungi), the organisms are best

known for their unique ability to degrade lignin. Lignin peroxidases are notorious for their utilization of several electron donor substrates because they possess a high redox potential relative to the class III peroxidases [80, 81]. Indeed, it can oxidize both phenolic and non-phenolic compounds. Similar to HRP, they also have two conserved calcium binding sites and disulfide bridges. However, the way they are arranged is different from class III peroxidases [59, 64, 78, 79]. Manganese peroxidase (MnP) is an acidic glycoprotein of about 42 kDa which has been thought to play the most vital role in lignin degradation [81, 82]. It has a fifth disulfide bridge contrasting other class II peroxidases in that it helps to anchor the Mn^{2+} in place for proper binding [81, 82].

The active site of class II peroxidases is similar to class III peroxidases in that phenylalanine occupies both the distal and proximal sides of the heme (Fig. 1.14 B). Hence, intramolecular electron transfer is much less a common event in this class of enzymes. Lignin peroxidase contrasts its counterparts in that a tryptophan (W171) has been identified as the site for surface oxidation during the transfer of electrons to the heme cofactor by a long range electron transfer mechanism [83].

1.5.2.3. Class I Peroxidases

In a number of respects, the class I enzymes of the Px-Ct superfamily stand distinct from classes II and III. Indeed, it has been proposed that class I diverged from the others at an earlier point in evolutionary history [59, 79]. The class I enzymes do not bind Ca^{+}, and disulfide bonds are very rare. The only disulfide linkage identified to date is observed in an extracellular fungal KatG enzyme [84]. The distribution of class I enzymes is also considerably wider, both in terms of species and cellular compartment. There are mitochondrial and non-mitochondrial forms of cytochrome c peroxidase (CcP) found across

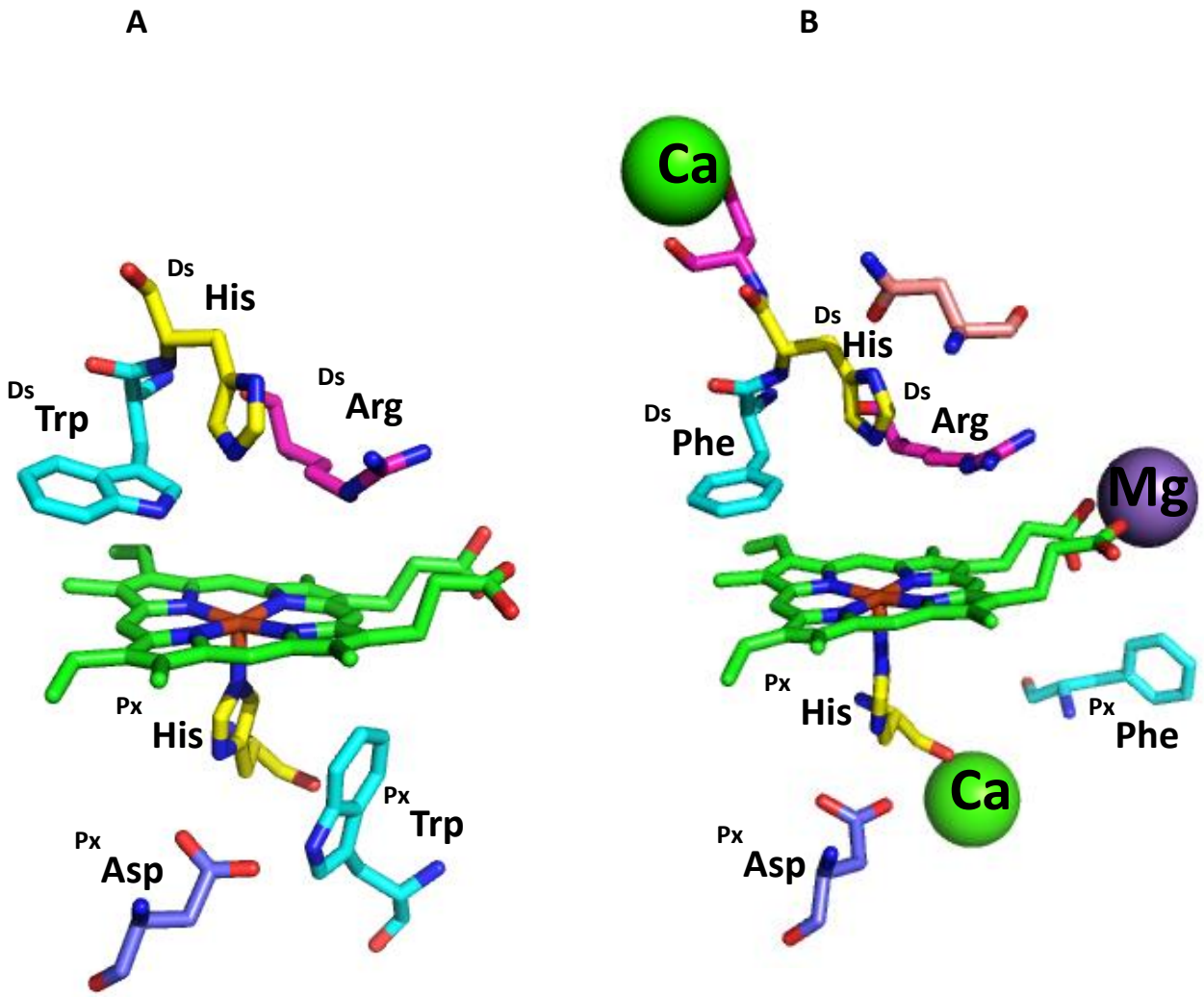

Figure 1.14. Active site comparison of cytochrome c peroxidase (class I) (A) and manganese peroxidase (class II) (B). Structures were constructed from accession domain 1BEM and 1MNP [65, 66] respectively.

the range of eukaryotes from yeast to mammals. Ascorbate peroxidase (APx) is found in plants where there is a chloroplast form and a cytosolic form [59, 64, 85-87]. The latter is particularly abundant in the root nodules of plants that house nitrogen fixing bacteria [88].

The catalase-peroxidases (KatG) are widely but not universally distributed among archaea, eubacteria, and lower eukaryotes, and across these species there are cytosolic and periplasmic/extracellular isoforms of the enzyme [52, 89-94]. Indeed, there are numerous organisms that have both a cytosolic and extracellular isoform. Interestingly, these enzymes are more closely related by cellular compartment rather than by the species in which they appear. All this appears to arise from multiple horizontal gene transfer events in the evolutionary history of these enzymes [89].

Class I enzymes are also distinct in terms of function. Where alternative metabolic functions can be identified for class II and III enzymes (e.g., lignin degradation and lignin synthesis, respectively), H_2O_2 detoxification appears to be the primary function of class I. CcP is well placed in terms of cellular location and available substrate (Fe^{II}-cytochrome c) to degrade H_2O_2 derived from misfiring of respiratory electron transport [95, 96]. APx (as opposed to catalase) is an ideal mechanism for H_2O_2 decomposition in root nodules and chloroplasts where O_2 would inactivate nitrogenase and inhibit photosynthesis [85, 88, 97]. Finally, KatG has a substantial catalase activity that imparts a capacity to degrade H_2O_2 far beyond any other members of the Px-Ct superfamily.

The class I enzymes also stand out at the active site level. The Phe residues (one distal and one proximal to the heme) found in most class II and III enzymes are replaced by Trp residues in class I. For this reason, intramolecular electron transfer to reduce Fe^{IV}=O

[porphyrin]$^{\bullet+}$ (i.e., compound I) intermediate figures much more prominently in class I enzymes than others.

For CcP, it has long been recognized that such electron transfers are essential to maximize rates of electron transfer from substrate (cytochrome c) heme to enzyme (CcP) heme, both of which are buried within their respective proteins. In APx, such intramolecular electron transfer must be specifically prevented by the binding of a K^+ adjacent to the enzyme's proximal Trp. This raises the potential of the Trp, such that the porphyrin radical form of compound I is stabilized [98, 99]. This helps maximize the specific oxidation of ascorbate by APx. Due in part to the research described in this dissertation, pathways of intramolecular electron transfer and their roles in KatG catalysis are beginning to be understood.

1.6. Catalase-peroxidases

Catalase-peroxidases (KatGs) are the third example of class I enzymes in the Px-Ct superfamily [64]. Until now, we have been discussing the independent mechanisms of H_2O_2 decomposition, *either* catalatic *or* peroxidatic. Across nature, all catalases (heme or non-heme) are poor in peroxidatic turnover while peroxidases show little or no catalase turnover. In contrast, KatG utilizes a single active site to scavenge H_2O_2 by both a catalatic and a peroxidatic mechanism [100, 101]. This unique ability has raised great interest in the study of KatG structure and function.

1.6.1. Sources of KatG

As mentioned earlier, KatG is found across a wide range of prokaryotes from archaea to gammaproteobacteria to mycobacteria to cyanobacteria [59, 93, 101, 102]. In fact, KatG is also found in several lower eukaryotes like protists (e.g., *Heterocapsa triqetra*) and fungi

(e.g., *Magnaporthe grisea*) [84, 91, 103]. Despite this wide distribution, there is very little sequence diversity among KatGs from various sources. Multiple sequence alignments show that these are very closely related enzymes despite their diverse origins. This also points toward lateral gene transfer as a common phenomenon in KatG evolution [89].

X-ray crystal structures have been solved for KatG from *H. marismortui*, *Synechocystis* PCC 7942, *B. pseudomallei*, *M. tuberculosis*, and *Magnaporthe grisea* which also solidify the conclusions that KatGs from various organisms are closely related because they contain similar features [84, 104-107]. All KatGs are multimeric (homodimers or homotetramers) and the KatG subunit is a two domain structure where each domain has a typical peroxidase scaffold (Fig. 1.15). The two domain structure of KatG is unique in the Px-Ct superfamily, even among class I enzymes and appears to be the result of a gene-duplication and fusion event.

1.6.2. Active Site of KatG's Domains

With its two peroxidase domains, the scaffold for an active site is present in each domain. However, the C-terminal domain neither binds heme nor directly catalyzes any reactions involving H_2O_2. Closer inspection of the C-terminal domain "active site" reveals that an Arg replaces what should be the His ligand. Heme binding is further precluded by a large hydrophobic side chain (Leu or Met) in the adjacent position (Fig. 1.15 C) which protrudes into the heme binding cavity. In contrast, the N-terminal domain has the typical Asp-modulated His ligand to the heme with a Gly residue found in the adjacent position. One could easily conclude that the C-terminal domain is a vestigial structure and superfluous to KatG function. However, there are no KatGs that lack this structure.

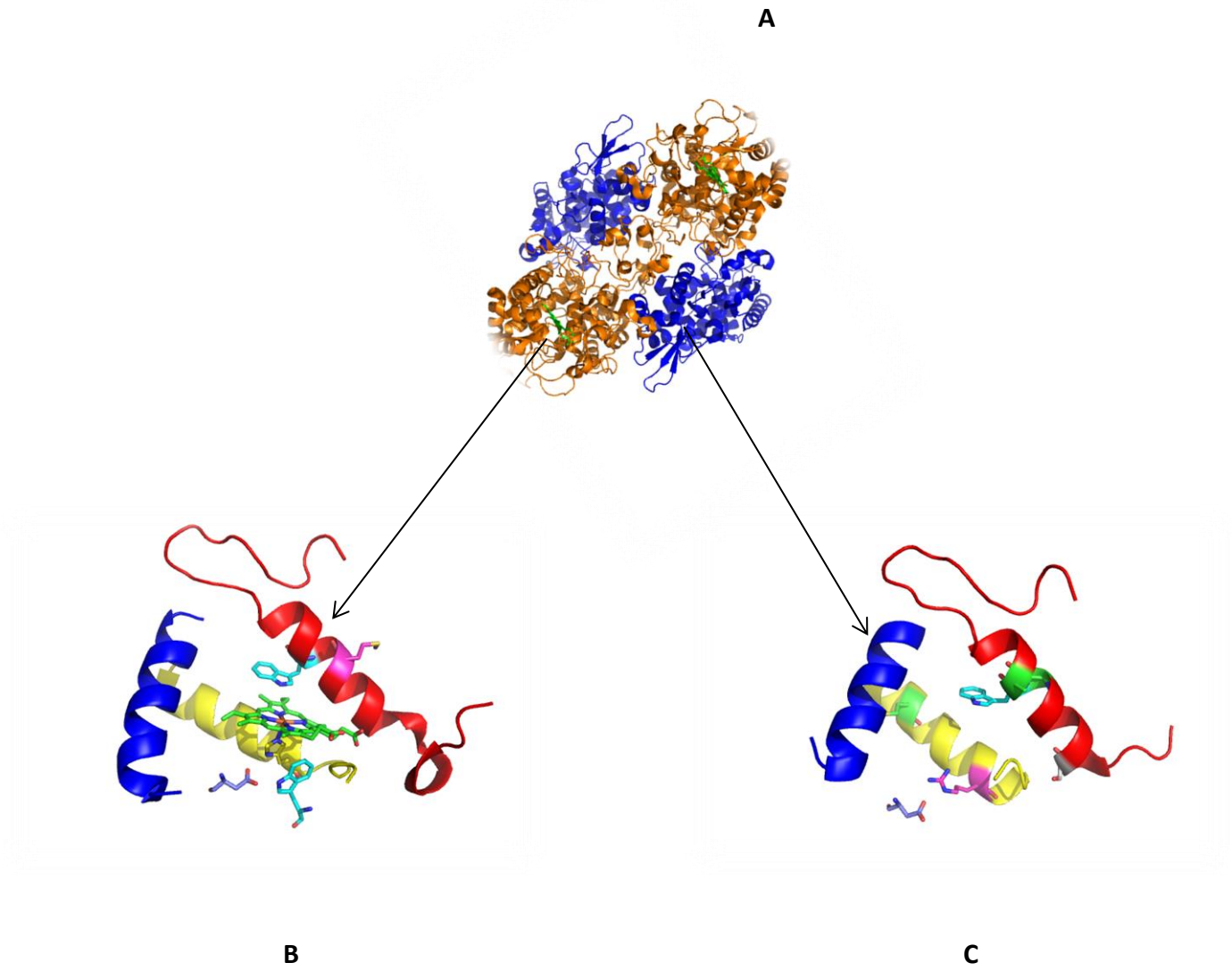

Figure 1.15. Three dimensional structure of KatG (A) and helices B, E, and F that bracket the active N-terminal domain (B) and the inactive C-terminal domain (C). Three helices are color coded as follows Helix B (Red), Helix E (Blue) and Helix F (Yellow). Structures were taken from PDB accession domain 2CCA [108].

Moreover, a KatG variant expressed without its C-terminal domain lacks both catalase and peroxidase activity. Its heme is hexacoordinate and low spin due to the introduction of the distal histidine as a sixth ligand to the heme iron [109]. A separately expressed and isolated C-terminal domain returns the enzyme to the correct active site structure and full catalase and peroxidase activity [110]. It is proposed that the C-terminal domain serve both to maintain an active environment for heme coordination and as a platform for the proper folding of the N-terminal domain despite its location 30 Å away from the active site [110]. Indeed, a recent report has shown that conserved amino acids at the N- and C-terminal domain interface are critical to maintaining correct heme coordination and active site function [111].

Contrary to the C-terminal domain, the N-terminal domain binds heme and has all the residues of a typical Px-Ct enzyme occupying its active site (Fig. 1.15 B). Consistent with its active site, KatG has robust peroxidase activity. However, in contrast to all other members of its superfamily, KatG also breaks down H_2O_2 through a catalase mechanism. This begs the question, what gives KatG this unique ability? Clearly, the answer should lie with features beyond those conserved in all peroxidases. A step back from the active site reveals that the KatG N-terminal domain has three interhelical loops that are substantially longer than their counterparts in other peroxidases. These are large loop 1 (LL1), large loop 2 (LL2) and large loop 3 (LL3) [84, 104-107].

LL3 is far from the active site and shows poor sequence conservation across KatGs. In contrast, LL2 which originates at the termination of the F helix and ends just before the G helix contributes to a more constricted active site channel than is observed in other peroxidases. Although sequence conservation is weak, its length and conformation are essentially invariant. Site-directed and deletion mutagenesis studies indicate that LL2 helps

regulate the organization of water and hydrogen bonds in the distal cavity of the active site [112]. It appears to be particularly important for ligand binding (e.g., CN^-, H_2O_2) and compound I formation and therefore, is necessary for optimal peroxidase *and* catalase activity [112].

In contrast, LL1 varies considerably in length, but portions of the structure are invariant across all KatGs. It is located between helices D and E, and also contributes to the more constricted active site access channel of KatG [84, 104-107]. The narrower channel produced by LL1 and LL2 is reminiscent of the long narrow channel observed in the typical catalases. It stands to reason that such a structure does favor catalase activity by limiting the oxidation of exogenous electron donors at the heme edge instead allowing oxidizing equivalents to be directed toward oxidation of H_2O_2 to O_2.

Although this structural arrangement favors H_2O_2 oxidation, it is not sufficient to explain KatGs catalase activity. The strictly conserved C-terminal one-third of LL1 is also critical because it includes a tyrosine (Y229 in *Mt*KatG). This tyrosine lies between the active site distal tryptophan (W107 in *Mt*KatG) and a methionine (M255 in *Mt*KatG), and it bridges the two in a novel MYW covalent adduct (Fig. 1.16) [84, 104-107]. The first evidence pointing toward this adduct as essential to catalase activity came when the distal tryptophan was replaced by phenylalanine using site-directed mutagenesis. This substitution resulted in the complete loss of catalase activity, but there was no effect on peroxidase activity [113, 114]. At the time, this result resisted a simple explanation because the analogous tryptophan was present in other class I peroxidases (see distal Trp 51 in CcP Fig. 1.14 A), all of which lacked any catalase activity. The first KatG crystal structure revealed the structure of the MYW adduct [107].

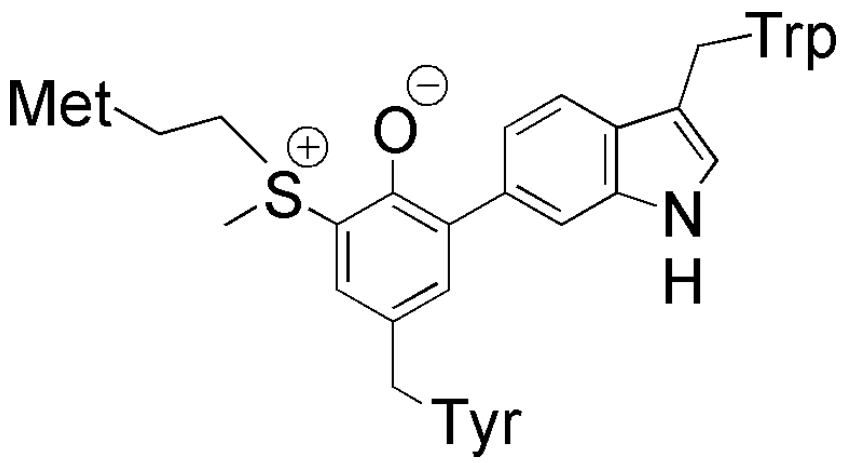

Figure 1.16. The structure of the methionine, tyrosine and, tryptophan (MYW) covalent adduct of KatG.

Electron density consistent with covalent bonds between the Cη2 of the distal tryptophan and $C_{\varepsilon}1$ of the adjacent tyrosine and between tyrosine $C_{\varepsilon}2$ and the Met S to produce a sulfonium cation was observed (Fig. 1.16) [84, 104-107].

1.6.3. Formation of the MYW adduct

One of the growing lists of post-translationally derived modifications catalyzed by a metal center could be advantageous or deleterious-remarkably frequent that it has been leveraged for a catalytic purpose. Most of these modifications frequent in enzymatic protein-based radicals. Several enzymes have the ability to harbor these protein-based radicals either temporally or in paramagnetic centers. Tyrosyl ($Y^{\bullet}$), tryptophanyl ($W^{\bullet}$), glycyl ($G^{\bullet}$), and thiyl ($S^{\bullet}$) radicals frequent in these protein-based reaction mechanisms [115, 116]. An example of such post-translational modification is seen in the tryptophan tryptophylquinone (TTQ) protein derived cofactor from the heme-dependent MauG enzyme [117-119]. TTQ is used by Methylamine dehydrogenases (MADH), an oxidase which catalyzes the deamination of primary amines to ammonia and an aldehyde.

The post-translational modification of TTQ is a six electron oxidation process where Trp57 is oxidized in the first step [119]. The oxidized Trp57 forms a covalent cross-link with Trp107 to yield a quinol. The modified quinol side chain is oxidized to form the unique TTQ cofactor (Figure 1.17). The reaction is known to occur when MauG forms a bis Fe^{IV} state in which one of the heme is in a unique Fe^{IV} state ligated by His and Tyr while the second is a more typical Fe^{IV}=O state [117-119].

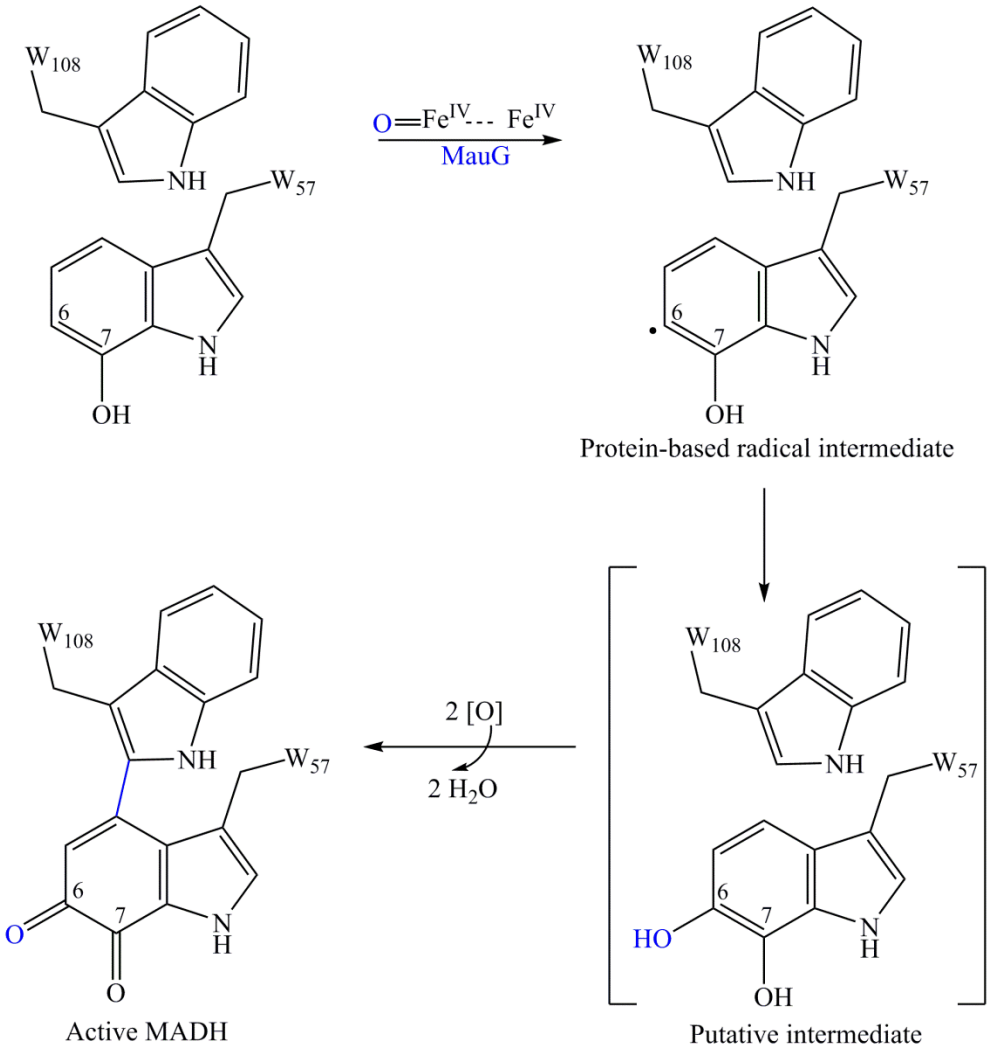

Figure 1.17. MauG-dependent oxidation of two tryptophans to yield tryptophan tryptophylquinone (TTQ) cofactor.

The KatG MYW adduct has numerous similarities to these systems housing protein-based radicals and it plays an integral role in the catalytic mechanism of KatG. The formation of the MYW adduct requires heme and the inclusion of peroxide (Fig. 1.18). The adduct is constructed from oxidizable amino acid side chains and has all the marks of a free radical-based mechanism. Though many details remain to be sorted out and only fully covalent intermediates have thus far been detected, a reasonable mechanism for MYW formation has been proposed [120, 121] (Fig. 1.18). The proposed mechanism requires the formation of compound I as an oxidizing intermediate. It has been proposed that the MYW adduct is formed in sequential steps. First, the adduct Tyr and Trp are been oxidized to their radical states. Next, a bond is formed between the Cε1 of Y and the Cη2 of W [i.e.,Y(Cε1)-W(Cη2)]. The second oxidation converts the Tyr-Trp partial adduct to a quinoid state. This creates an electrophilic milieu for the Y(Cε2)-Met(Sδ) sulfonium cation to complete the entire Met-Tyr-Trp covalent adduct [120, 121].

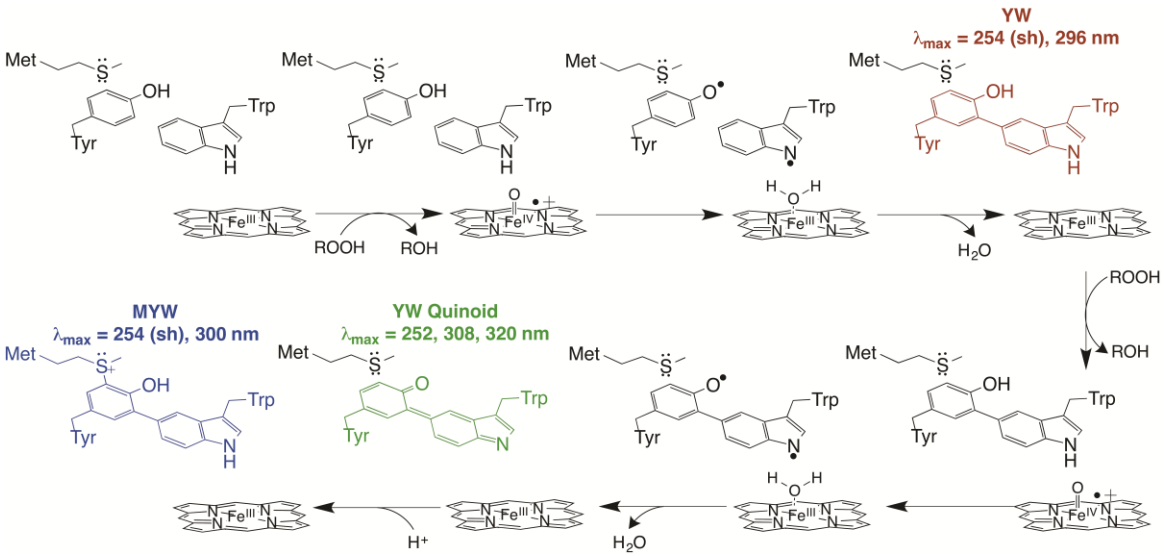

Figure 1.18. Proposed mechanism for the formation of the MYW cofactor. The YW (red) andYW quinol (green) intermediates have been identified in KatG variants where the adduct Met has been replaced by Ile [120, 121].

1.6.3.1. Diagnosis of the MYW covalent adduct by SDS-PAGE and LC-ESI-MS.

An early concern was that the MYW adduct may be an artefact of X-ray irradiation. Tryptic peptide mapping of KatG from several sources by LC-mass spectrometry has shown that the covalent adduct is present in KatG as isolated following protein expression, provided the protein is expressed in its holo form [120-123].

An interesting alternative procedure for evaluating the presence of the adduct has emerged which relies on SDS-PAGE to evaluate the effect of the cross-link on the hydrodynamic volume of the unfolded protein. Because the adduct is not disrupted by SDS, KatG bearing the MYW adduct retains a more compact structure than KatG which lacks the adduct, including apoKatG which has never contained heme and KatG variants unable to form the adduct (e.g., Y226F KatG). These latter proteins migrate with an apparent molecular weight of ~ 3 kDa larger than mature MYW adduct-bearing KatG [112]. Interestingly, LC-ES-MS spectra protein from either SDS-PAGE band show identical molecular weights, demonstrating that the molecular weight difference observed by gel is an apparent difference only (Fig. 1.19). From the procedure, it can be shown that MYW adduct formation requires the presence of heme and peroxide as an oxidant (e.g., H_2O_2, *m*-chloroperoxybenzoic acid, or *t*-butyl-OOH) (Figs. 1.19-panel B & 1.20). It can also be shown that *E. coli* KatG variants can lack catalase activity because they are unable to form the adduct (e.g. Y229F KatG) or for other reasons (ΔLL2 KatG).

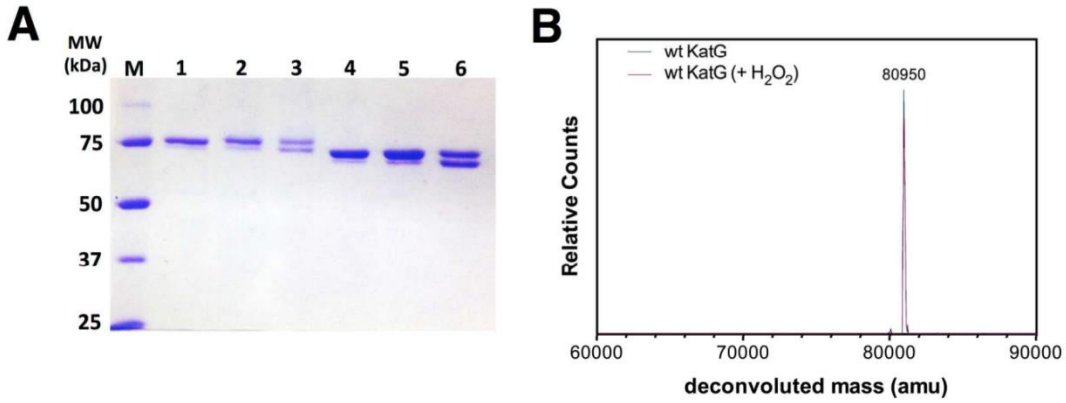

Figure. 1.19. Effect of reconstitution and treatment with H_2O_2 on SDS-PAGE separation (A) and ESI-MS (B) of wild-type KatG. Wild-type KatG (lanes 1 – 3) and ΔLL2 KatG (lanes 4 – 6) were separated as unreconstituted proteins (lanes 1 and 4), proteins reconstituted with 0.9 eq. hemin (lanes 2 and 5), and reconstituted proteins reacted for ten minutes with 20 eq. H_2O_2 (lanes 3 and 6). All reactions contained 5 μg protein (~ 3 μM) and were carried out in 5 mM phosphate, pH 7.0, at room temperature. Reactions were quenched by the addition of an equal volume of SDS-PAGE loading buffer (2% SDS final concentration), and 2.5 μg protein was loaded into each lane. Reconstituted *wt*KatG was evaluated by LC-ESI-MS before and after reaction with 20 eq. H_2O_2.

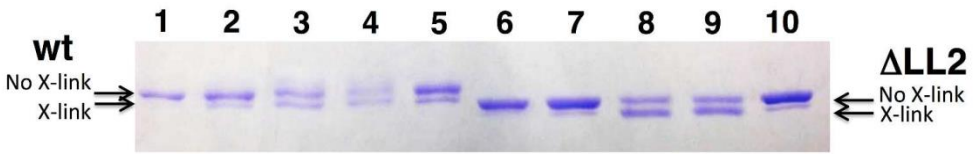

Figure 1.20. Effect of reconstitution and treatment with peroxides on SDS-PAGE separation of wild-type and ΔLL2 KatG. Wild-type KatG (lanes 1 – 5) was compared to ΔLL2 KatG (lanes 6 – 10). Unreconstituted proteins (lanes 1 and 6) were run next to proteins reconstituted with 0.9 eq. hemin (lanes 2 and 7). Each reconstituted protein was reacted for ten minutes with 20 eq. H_2O_2 (lanes 3 and 8), 10 eq. *m*-chloroperoxybenzoic acid (lanes 4 and 9), or 10 eq. *t*-butyl-OOH (lanes 5 and 10).

1.6.4. Catalatic Mechanism of KatG

More recently, a catalatic mechanism for KatG has been proposed in which the covalent adduct redox cycles between a fully covalent (reduced) and free-radical (oxidized) state. Upon the formation of compound I like canonical catalases and peroxidases, KatG undergoes an intramolecular electron transfer to form a Fe^{IV}=O[protein]$^{\bullet+}$ intermediate. Indeed, the unique MYW covalent adduct is proposed as the electron donor, giving a Fe^{IV}=O[MYW]$^{\bullet+}$ intermediate referred to as compound I* [124, 125]. Compound I* reacts with the second equivalent of H_2O_2 yielding a compound III (i.e., Fe^{III}-$O_2^{\bullet-}$) species typical of canonical peroxidases. This species also has the radical on the covalent adduct associated to it, (i.e., Fe^{III}-$O_2^{\bullet-}$[MYW]$^{\bullet+}$) referred to compound III* [124-126]. With the MYW adduct radical only about 3.4 Å from the heme, another intramolecular electron transfer is proposed wherein the Fe^{III}-$O_2^{\bullet-}$ species reduces the MYW adduct radical to its fully covalent state. In principle, this produces a transient Fe^{III}-O_2 state which undergoes facile dissociation to release O_2, leaving the enzyme in its initial ferric (resting) state (Fig. 1.21, bold black and blue).

The MYW adduct radical (narrow-doublet) is the sole radical produced when KatG reacts with steady-state concentrations of H_2O_2 in the millisecond time range [127]. An elaborate study of site-directed mutagenesis of all 21 Tyr of KatG, deuterium labeling of the β-methylene protons and 3,5-ring protons of the adduct tyrosine, along with rapid-freeze quench and manual quench EPR were done to assign the narrow-doublet radical. All these data pointed towards the tyrosyl radical located on the MYW covalent adduct [124, 127]. Indeed, all tyrosines of *Mt*KatG which were mutated to phenylalanine produced the narrow doublet radical and produced wild-type levels of catalase activity except that located on the

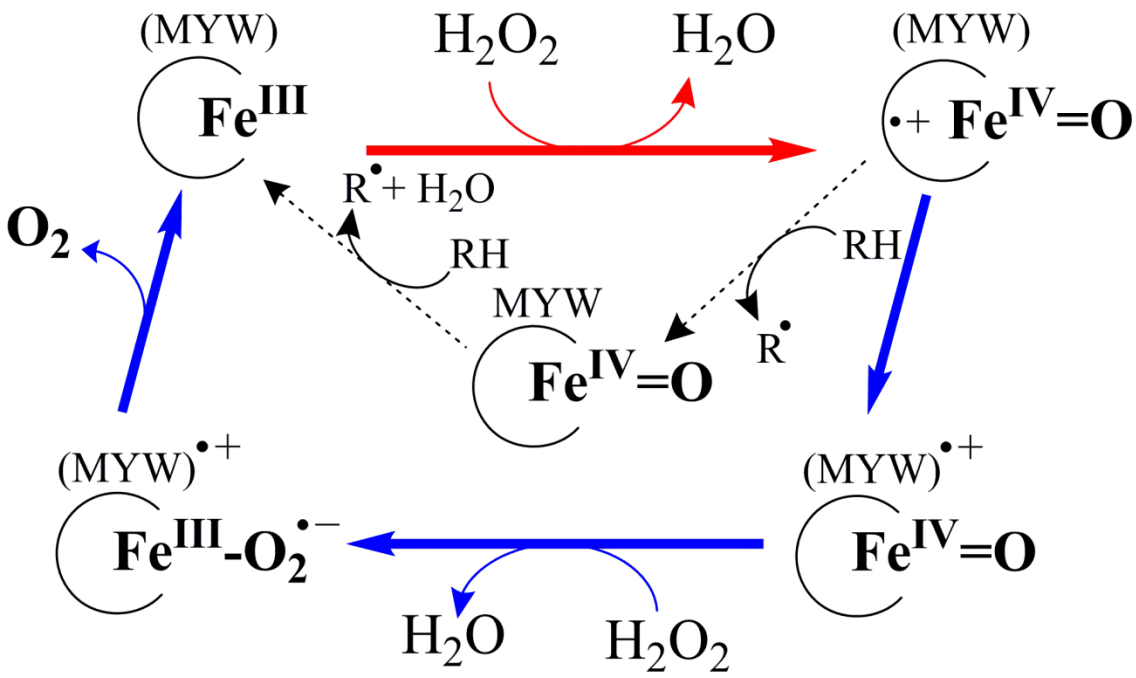

Figure 1.21. KatG catalatic and peroxidatic reaction cycles. Reaction common to both cycles are shown in red. Proposed route for catalatic turnover is shown in blue by way of a Fe^{III}-$O_2^{\bullet-}$ $[MYW]^{\bullet+}$ intermediate. Peroxidatic turnover is completed through dashed arrows.

located on the MYW adduct. Further, deuterium labeling of the β-methylene protons did produce a singlet radical which contrasted the narrow-doublet radical. The collapse of MYW narrow doublet radical supports that the radical was tyrosyl based. Deuterium labelling of the 3,5-ring protons produced the narrow-doublet radical like wild-type KatG. This also supports that the protons at that position had been replaced by neighboring groups of the Met and Trp to form the entire MYW covalent adduct. KatG variants targeting the covalent adduct lack the ability to produce the unique MYW narrow-doublet radical along with their loss in catalase activity.

Alternative radicals are observed when KatG is treated with other hydroperoxides just like other members within its peroxidase class [128-130]. For example, cytochrome *c* peroxidase (a class I peroxidase) forms an exchange-coupled proximal tryptophanyl radical (Fe^{IV}=O [W191]$^{\bullet+}$) i.e., Compound ES after its reaction with H_2O_2 (Fig. 1.22) [131, 132]. Indeed, the radical located about 5.1 Å from the heme is integral in the catalytic mechanism of C*c*P. The proximal tryptophanyl radical serves as a mediator for electron transfer from the ferrocytochrome c donor to the cytochrome c peroxidase acceptor. In addition to the proximal tryptophanyl radical formed by C*c*P, it can also readily form compound III in the presence of excess H_2O_2 and low concentrations of ferrocytochrome c. The compound III intermediate is known to be stable and readily inactivates C*c*P. The compound III intermediate is also known to play an active role in KatG catalase mechanism but CcP does not perform catalase activity.

KatG also loses its catalase activity by forming the exchange-coupled proximal tryptophanyl radical along with other protein-based radicals when it is reacted with peracetic acid. The presence of these alternate protein-based radicals may be detrimental to KatG cat-

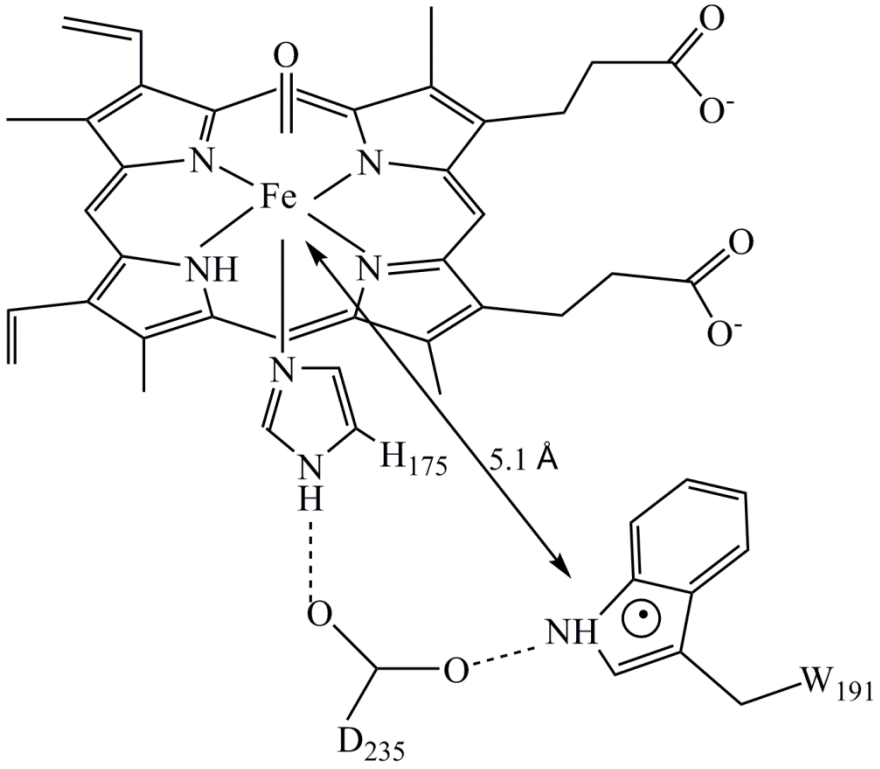

Figure 1.22. The exchange-coupled proximal tryptophan cation radical from yeast cytochrome c peroxidase.

alase activity, hence converting KatG back to its peroxidase roots. For KatG optimum catalase activity, oxidation of the protein has to take place during turnover and the oxidizing equivalent have to stay close to the heme. There are potential consequences of this type of mechanism where other amino acids can get oxidized and there is a loss in the catalase activity. This idea brought forth the basis of this research with purpose of evaluating routes for off-pathway protein oxidation events and KatG inactivation.

All KatGs isolated have an invariant conformational dynamic arginine switch which is also an important participant in its catalase mechanism. R418 (*Mt*KatG numbering) located about 20 Å from the heme center is known to occupy two conformational dynamic positions as pH changes. Structures resolved for *Bp*KatG reveal that an 'out' conformation formerly known as 'R' state is favored at acidic pH (i.e., pH < 4.5) [133, 134]. This state is known to favor the MYW adduct oxidation. In contrast, an 'in' position formally known as a 'Y' conformation is favored at a pH > 6.5. This conformation has been suggested to favor the MYW adduct radical reduction. At a pH where both conformations are equally populated (i.e., pH = 6.5), KatG has optimum catalase activity. This pH-dynamic Arg switch is also connected to KatGs catalase and peroxidase activities which are also known to be pH-dependent [135, 136].

1.6.5. Interrelationship between KatG's Catalase and Peroxidase Mechanisms

It is also important to understand the nature of interaction between the catalase and the peroxidase activities of KatG. This is because this thesis also cuts across the mechanism by which peroxidase reducing substrates are hypothesized to rescue catalase-inactive intermediates. Indeed, KatG is capable of using a single active site to degrade H_2O_2 through a catalatic and a peroxidatic mechanism [100, 101]. The fascinating question is that how do

these activities interact? This is especially important as they share the same active site and the same type of intermediate i.e., compound I, (Fig. 1.21, black arrows). Historically, both activities have simply been superimposed within a single scheme. The consequence of this arrangement is both activities are mutually competitive with one another. Specifically, peroxidatic electron donors would be predicted to inhibit the catalase activity of KatG. Consistent with this model, conditions which favor KatG catalase activity (pH = 7.0, high [H_2O_2]) do not favor its peroxidase activity (pH = 4.5, relatively low [H_2O_2], and vice versa [100, 101]. Further, catalase-negative variants almost always show enhanced peroxidase activity [113, 114, 121, 125]. Finally, the first characterization of KatG reported that a common peroxidatic electron donor, *o*-dianisidine did inhibit the catalase activity at pH 7.5 [137].

Contrary to all these observations, the Goodwin lab reported that PxEDs *stimulated* the catalase activity of KatG. The effect was most pronounced under conditions where catalase activity is normally diminished and peroxidase activity increases (i.e., acidic pH and low [H_2O_2]) [138]. This result has three implications. First, the model for understanding the interplay of these two activities is clearly flawed. Second, it points toward a mechanism for far more efficient detoxification of H_2O_2, and third, it broadens the conditions under which vigorous H_2O_2 decomposition can be accomplished, especially with respect to pH. In this thesis, we used site-directed mutagenesis, steady-state and transient-state kinetics, UV-visible and EPR spectroscopies to explore the mechanisms by which PxEDs stimulate KatG catalase activity. We observed that PxEDs stimulate KatG catalase activity by rescuing inactive intermediates which result from off-pathway protein oxidation events and the proximal tryptophan is a major conduit for such misdirected electron transfer events.

1.7. Implications for the Physiological Function of KatG

In addition to its role in H_2O_2 degradation to protect cells against the harmful effects of ROS, KatGs have also been consistently linked as virulence factors to a wide range of pathogenic organisms. These organisms range from extracellular pathogens (plasmid encoding *E. coli* O157:H7 and *Magnaporthe grisea*) to intracellular facultative pathogens (*Legionella pneumophila* and Yersinia pestis) [45, 84, 91, 103]. Further, the enzyme from the intracellular facultative *Mycobacterium tuberculosis* is widely known to activate isoniazid, a frontline drug in the treatment of tuberculosis (Fig. 1.23) [100]. The mechanism of activation is not fully understood but it is proposed to oxidize the prodrug to its active isonicotinoyl acyl radical form which further reacts with NADH to form an INH-NADH adduct (Fig. 1.23).

Several KatG protein-based radical mechanisms have been proposed for INH activation which can be divided into two main groups (Fig. 1.23 B). The first is a peroxide-dependent mechanism which uses a compound I-like intermediate or its equivalent as the prominent species [135-137]. The second is a peroxide-independent mechanism where a compound III intermediate is proposed as central player [135, 137, 138]. Both mechanisms can be formed in the presence or absence of added oxidants like peroxides.

As such, a clear understanding of KatG protein-based radical mechanisms will open possibilities on how the pro-drug could be oxidized by KatG. It has been initially proposed that electron donors like isoniazid act to reduce remote protein-based radicals formed in KatG catalysis [130]. This thesis also sheds light on the protein-based radical types observed during KatG reactions with H_2O_2.

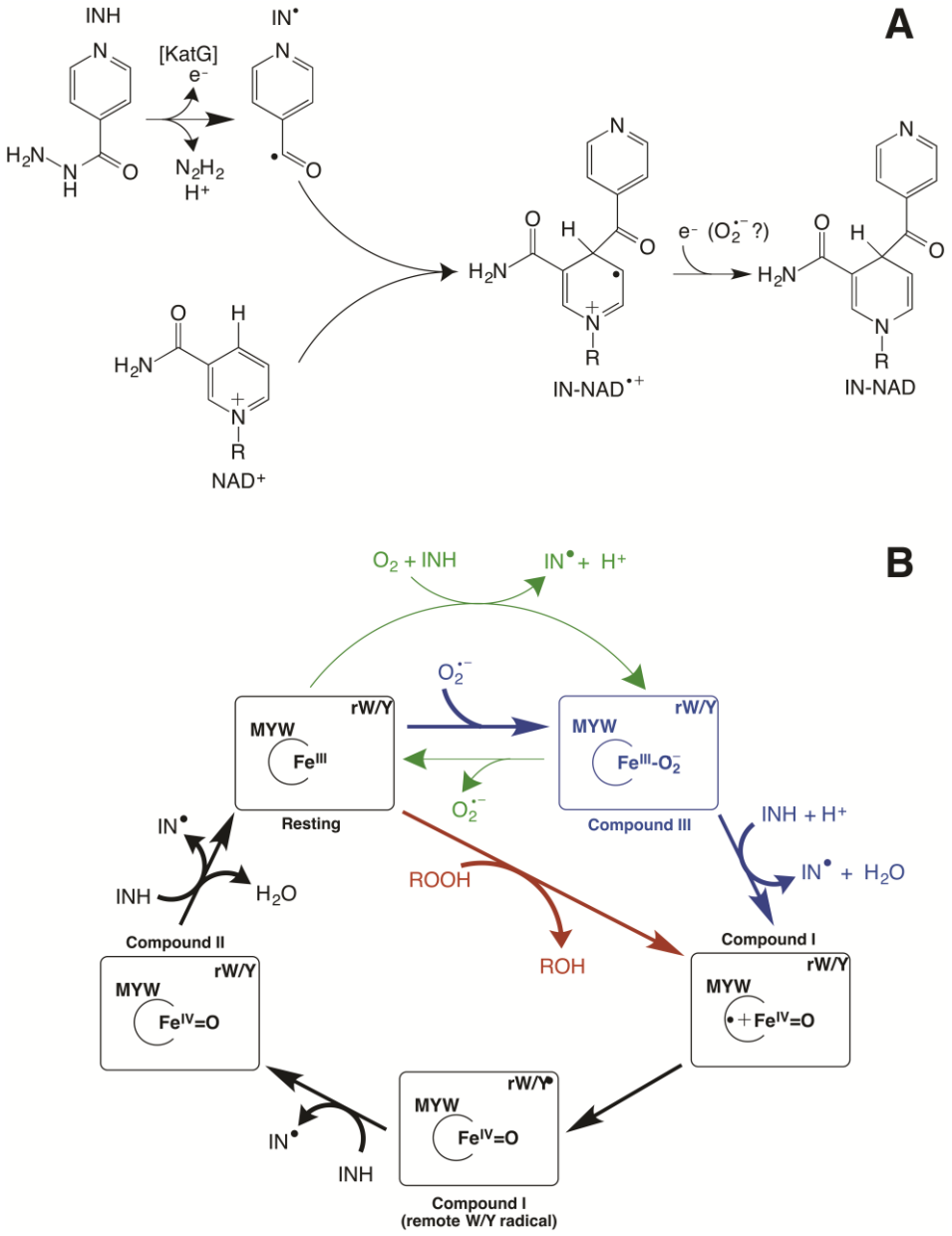

Figure 1.23. Isoniazid (INH) structure and activation. Formation of IN-NAD adduct (A) and three mechanisms proposed for KatG-dependent oxidation of INH to IN$^{\bullet}$ (first step indicated in panel A). Steps in green are proposed to represent the oxidation of INH in the absence of any oxidant. Steps in blue indicate the presence of an endogenous oxidant while steps in red are indicative of endogenous peroxide.

The INH-NADH adduct is a potent inhibitor of InhA, an enoyl acyl carrier protein reductase necessary for mycolic acid biosynthesis (a long chain fatty acid for the organism's cell wall). Mutations which disrupt the *katG* gene occur in the large majority of isoniazid resistant cases, though the mechanism of inactivation has not been fully comprehended [100].

1.8. Protein-based Radicals in Catalase-Peroxidases (KatG)

KatGs are an exciting system to consider the use of protein-based radicals for its unique catalytic abilities. As mentioned before, KatGs fall into the class I of non-animal peroxidase superfamily of enzymes. KatG contrasts all other members within its superfamily in that it uses a single active site to catalyze the decomposition of H_2O_2 by two distinct mechanisms as suggested by its name. The active site of KatG is almost superimposable with that of cytochrome c peroxidase. Also, the active N-terminal domain of KatG has far more oxidizable amino acid residues than other proteins including 18 Trp, 12 Tyr and 13 Met. Figs. 1.24 A and B show Trp (red) and Tyr (orange) contributions to the *Mt*KatG surface viewed from substrate access channel side (A), and its opposite (B). The N-terminal domains are blue, and the C-terminal domain domains are gray. The presence of far more oxidizable residues present in KatG makes protein-based radicals frequent in its catalytic mechanism.

It has been agreed that radical transfer migrates from the active site to the solvent exposed surface to remote Trp and Tyr residues. Also, H-bonding network within the active site plays a pivotal role in KatG intramolecular electron transfer processes [139, 140]. KatG from various organisms are known to stabilize different protein-based radicals when the

enzyme is reacted with peracetic acid. For example, *Sy*KatG forms a radical on Trp105 and a Tyr radical while *Mt*KatG and *Bp*KatG rather form the exchange-coupled proximal Trp and a Tyr radical (Fig. 1.25) [126, 129, 140]. KatG uses two distinct protein-based radicals to catalyze two distinct mechanistic activities: The MYW narrow doublet radical and the proximal tryptophanyl radical.

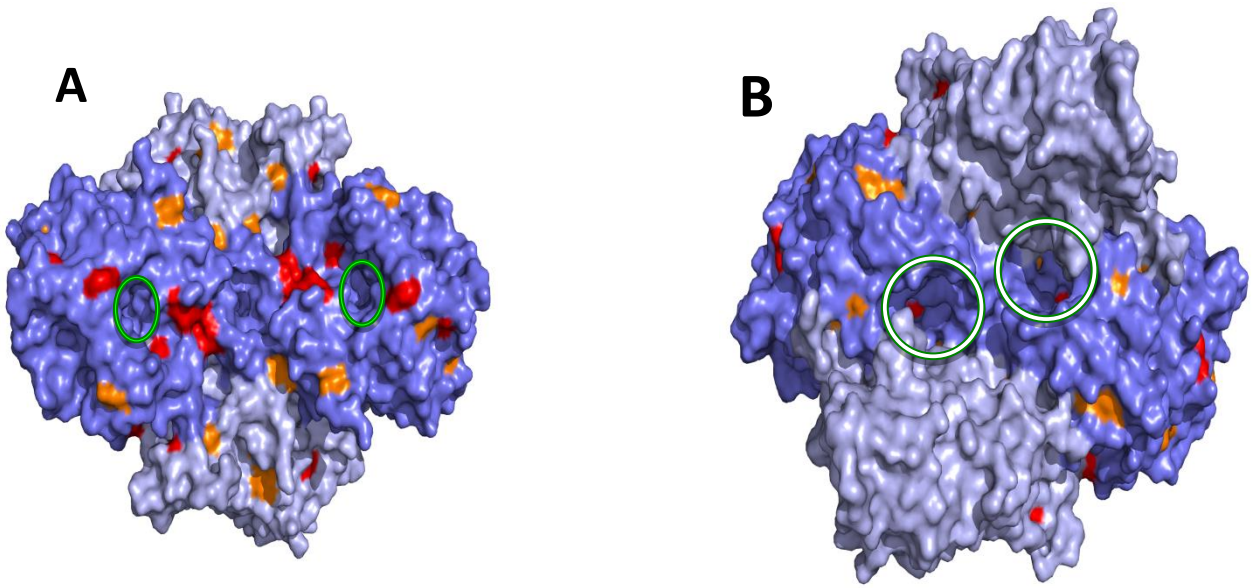

Figure 1.24. Trp (red) and Tyr (orange) contributions to MtKatG surface viewed from H_2O_2 access channel side (A) and its opposite (B). The N-terminal domains are blue, and the C-terminal domains are gray. Green circles indicate the access channel opening. White circles indicate a cavity where INH has been detected in another KatG [141]. Image constructed using PyMOL v.1.6.0.0.

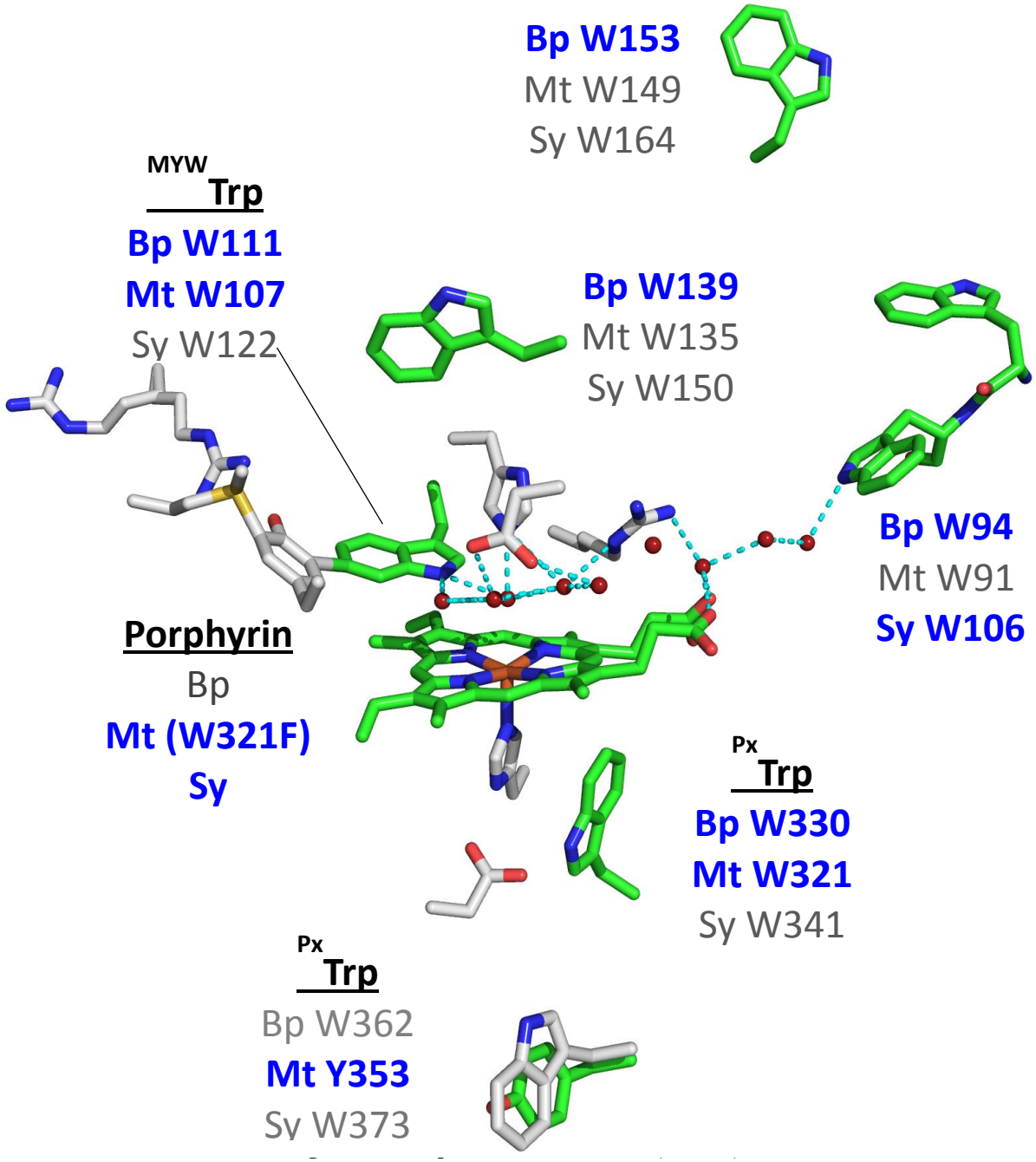

Figure 1.25. Tryptophanyl and tyrosyl radicals identified in MtKatG (Mt), BpKatG (Bp), and SyKatG (Sy). Radicals assigned in each KatG are annotated in blue. If a radical has not been detected in a given position, it is annotated in gray. Image constructed using PyMOL v.1.6.0.0.

1.8.1. The MYW cofactor protein-based radical

Evidence is accumulating that a unique narrow doublet (MYW) radical cofactor is essential for the catalase activity of KatG [124, 127, 142]. This radical is known to have a tyrosyl-like character. It is the sole radical observed by RFQ-EPR when KatG is reacted with steady state concentrations of H_2O_2 in the millisecond time range. The radical persist through out the conclusion of H_2O_2 consumption. Mutations on these residues constituting the covalent adduct lack catalase activity and the ability to generate the narrow doublet radical. The radical is formed in the presence of heme and peroxide. It has been proposed to be formed by heme catalyzed free-radical chemistry (Fig. 1.18) [120, 121].

1.8.2. The Proximal Trp protein-based radical

The proximal Trp protein-based radical persists during conditions of peroxidase turnover (Fig. 1.21, dashed arrows). As mentioned before, this radical has been consistently detected when KatG reacts with PAA [129, 130, 140, 143]. Due to its proximity to the heme iron, it has been hypothesized to form an exchange-coupled interaction with a nearby ferromagnetic center, presumably the heme. This idea support the proximal tryptophan as the first residue to be oxidized if the porphyrin radical or MYW adduct radical gets off-track the catalatic mechanism. The radical will subsequently migrate to the surface of KatG to remote residues. It has also been thought that because of the narrow substrate access channel for KatG, peroxidase electron donors like isoniazid may not have full access to the active site or access to the δ-meso heme edge as utilized by canonical peroxidases. Hence, they might act to reduce the remote protein-based radicals.

1.8.3. Interrelationship between the two protein-based radicals in KatG

Two protein-based radicals observed in KatG catalysis participate in two distinct mechanisms of H_2O_2 detoxification. The catalase (MYW radical) and peroxidase (proximal Trp radical) activities of KatG are performed in the same active site where the ferric enzyme is reacted with one equivalent of H_2O_2 to form an oxo ferryl π cation radical known as compound I. The route by which both cycles are completed are distinct. For its peroxidase cycle, two equivalents of exogenous electron donors return compound 1 back to its resting state at the expense of two equivalents of an electron donor radical and water. The physiological electron donor of KatG has not been identified yet. In contrast, for KatG catalase activity, it has been proposed that compound I undergoes an intramolecular electron transfer and the porphyrin radical is reduced by a protein-based radical. Indeed, the unique MYW adduct has been proposed as the electron donor to achieve this intramolecular electron transfer process to form a compound I* intermediate. This intermediate reacts with a second equivalent of H_2O_2 to form a compound III* species. A second intramolecular electron transfer is proposed to occur from the ferric superoxide species to neutralize the MYW adduct radical making feasible the release of oxygen for the enzyme to return to its resting ferric state and a close shell MYW adduct. Hence for all intents and purposes, both KatG protein-based radicals should be mutually exclusive. Up to this point, it is still not clear how both protein-based radicals participate in these dual mechanisms of H_2O_2 degradation. This dissertation gives bearing to these two protein-based radicals in KatG catalysis, thereby unraveling a conundrum in KatG chemistry.

1.9. Heme, Structure, and Signatures

Heme is composed of a highly conjugated tetrapyrrole macrocycle and an iron ion ligated by the N of each pyrrole (Fig. 1.26) [144-146]. As such, the range of heme states that participate in the wide range of chemistry facilitated by heme-dependent proteins can be monitored by a truly vast range of spectroscopic techniques: UV-visible absorption, circular dichroism, magnetic circular dichroism, resonance Raman, Mössbauer, Electron Paramagnetic Resonance (EPR), and others. With respect to the work presented here, we have made extensive use of UV-visible absorption and EPR in conjunction with rapid mixing kinetic techniques to evaluate protein-based radicals and heme intermediates in KatG catalatic mechanisms. In order to provide some background and a context for the interpretation of the results, an overview of heme-state evaluation by UV-visible absorption and protein-based radical evaluation by EPR is presented.

1.9.1. Evaluation of heme states by UV-vis absorption spectroscopy

Two types of transitions (i.e., $\pi \rightarrow \pi^*$ and charge transfer) are the most frequently detected by UV-visible absorption with heme and heme-dependent proteins. The $\pi \rightarrow \pi^*$ transitions arise due to the absorption and excitation of porphyrin π electrons, and the second type are observed when there is charge transfer between the d electrons of iron and the orbitals of the porphyrin (Fig. 1.27). In some cases, there might also be axial ligand to metal charge transfer bands. The alpha (α or Q_{00}), beta (β or Q_{0v}), and gamma (Soret or γ) absorptive bands all arise from porphyrin $\pi \rightarrow \pi^*$ transitions. The Soret band is the highest energy transition (lowest λ_{max}) because it originates from a lower π energy level (i.e., a_{1u}), and excites to a higher π^* energy level (i,e., e_g). It is also the most prominent feature of the

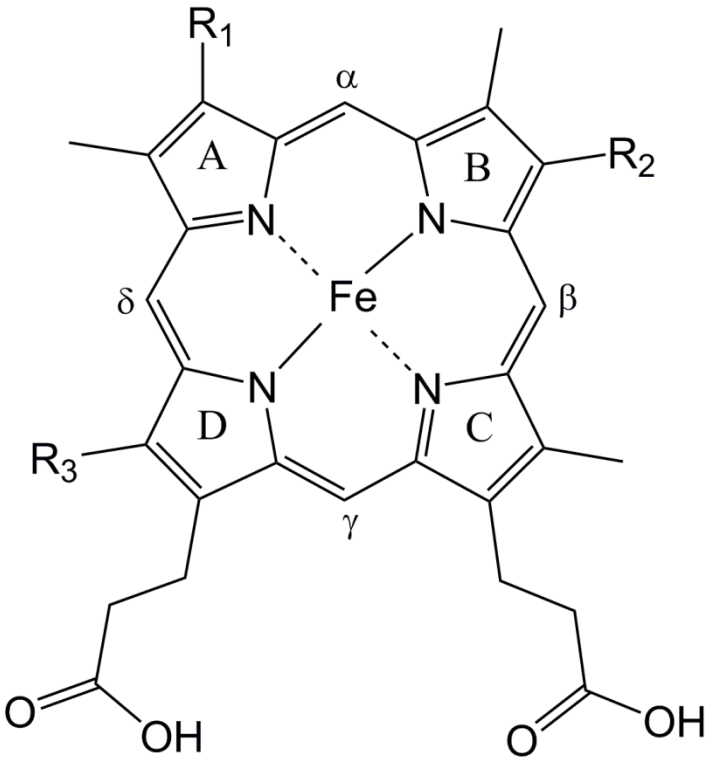

Hemes	Chemical formula	Functional group (R_1)	Functional group (R_2)	Functional group (R_3)
Heme *a*	$FeC_{49}H_{56}O_6N_4$	-CH(OH)CH_2Farnesyl	-CH=CH_2	-CH=O-
Heme *b*	$FeC_{34}O_4N_4$	-CH=CH_2	-CH=CH_2	-CH_3
Heme *c*	$FeC_{34}H_{36}O_4N_4S_2$	-CH-(Cystein-Syl)-CH_3	-CH-(Cystein-Syl)-CH_3	-CH_3
Heme *d*	$FeC_{34}H_{30}O_{10}N_4$	-CH=CH_2	-CH=CH_2	-CH_3

Figure 1.26. General structure for hemes and the various types. Heme types were taken from PubChem Open Chemistry Database using the CID numbers; 5288529 for heme *a*, 444098 for heme *b*, 444125 for heme *c*, and 49800103 for heme *d* respectively.

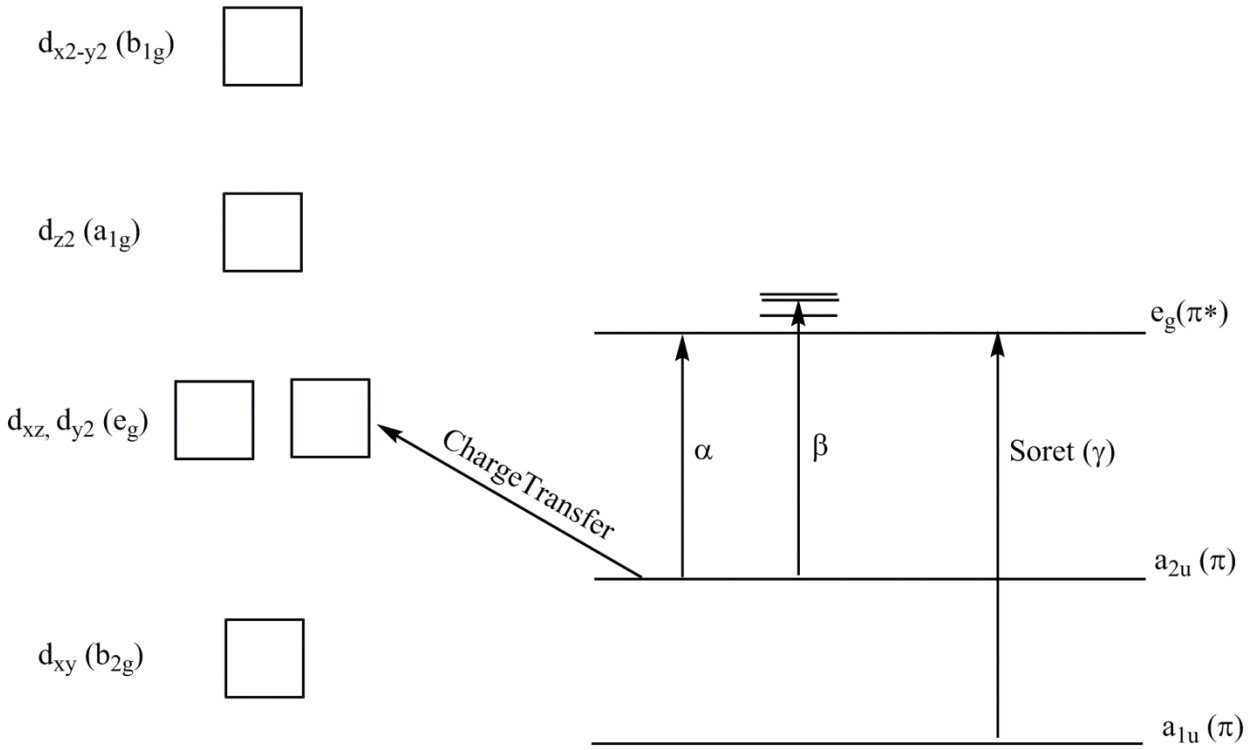

Figure 1.27. Types of transitions observed for heme peroxidases. The energy levels for both the d-d transitions for the iron are shown on the left while the energy levels typical for the porphyrin are shown on the right.

heme spectrum. In contrast, the α and β transitions originate from a higher π energy level (i.e., a_{2u}) and terminate at the π * energy level (i.e., e_g), translating into longer wavelength spectral features. The β transition is of slightly higher energy than the α transition because it terminates at vibrationally excited energy levels in e_g. Thus, the β band is observed at shorter wavelength (~ 520 - 540 nm) than the α band (~ 550 - 580). When the porphyrin electrons are excited from their highest–filled energy levels to their lowest unoccupied d-orbital of the iron, a charge transfer transition is observed. The wavelength range for the charge transfer transitions overlaps with that of the α and β bands. The nature and type of ligands have a dramatic influence on the optical properties of both types of transitions, but for different reasons. The impact of axial ligands is to alter the redox and spin-states of the metal center which is indirectly captured by alterations to the energies of π to π* transitions. Obviously, the ligands have a more direct impact on the ligand and metal charge transfer bands.

Through the long accumulation of substantial empirical spectral data, UV-visible absorption spectra provide a useful gauge of the oxidation state and coordination environment of heme proteins. For ferric heme not complexed in proteins, the Soret band appears at wavelength of about 380 nm. This is due, at least in part, to the formation of μ-oxo hemin dimers in solution, a structure that cannot be accommodated in most heme-enzyme active sites. Thus, ferric heme ligated to its requisite protein produces a red shift of the Soret band to a wavelength of about 400 nm. Factors that could affect this wavelength include spin and oxidation states of iron and the identity of ligands. Indeed, the ferric resting state of KatG has a Soret maximum band near 408 nm. The charge transfer bands are typically observed with high spin states but not low spin states. For the high spin heme, the λ_{max} for the CT transitions varies with the identity of the weak field ligand. For example, if fluoride is

the ligand, it has CT1 and CT2 bands at 612 and 448 nm respectively. If hydroxide is the ligand, no CT bands are detected [144]. The absence of CT transitions in low spin states is because an electron is dropped from the porphyrin π^* orbital into a d-orbital of the iron to completely fill it. Ferric KatG is dominated by high-spin states. Its charge transfer bands appear at 502 nm (CT2) and 630 nm (CT1) respectively.

As discussed previously, the proximal His ligand modulated through the proximal Asp H-bond acceptor produces a substantial imidazolate character to the ligand and a relatively low Fe^{III}/Fe^{II} reduction potential (-200 mV) [103]. As such, KatGs are routinely isolated in the ferric state. UV-visible absorption spectra usually display a Soret band maximum near 408 nm. The λ_{max} and line-shape of the spectrum both suggest a mixture of ferric states. Pentacoordinate high-spin peroxidases (e.g., HRP) tend to show lower λ_{max} and molar absorptivities in the Soret band (λ_{max} 403 nm) [144, 147]. Hexacoordinate high-spin peroxidases (where H_2O or a halide ion is the sixth ligand) show red-shifted Soret bands (~410 nm) with greater (by ~25%) molar absorptivities. In the ferric high-spin states, charge transfer bands at ~ 500 nm and ~ 640 nm are plainly evident, and they tend to obscure the ferric α and β transition which fall in between them [144, 147]. The λ_{max} of the CT band at 640 nm will shift depending on the identity of the sixth ligand. As isolated, ferric KatG is dominated by high-spin ferric states with a mixed population of hexacoordinate and pentacoordinate states [100, 112, 148]. The former appears to dominate, and the sixth ligand in question is most likely a water molecule. On occasion, a strong field ligand can be introduced into the KatG heme ligand sphere. This produces a substantial red shift in the Soret band to ~ 418 nm, the loss of the CT bands, and as a result, increasing prominence of the β and α transition at ~ 535 nm and ~ 570 nm, respectively. This can also be accomplished

with exogenously added strong field ligand like CN^- or N_3^-, but it is also observed in some KatG variants where an active site structural shift allows the distal His to coordinate to the heme iron [109, 110]. As isolated, the hexacoordinate low-spin state makes little if any contribution to the KatG absorption spectrum. From UV-visible absorption, a general sense of the distribution of spin and coordination states of the ferric enzyme can be discerned. In order to get a more definitive picture of the states represented and their relative abundances, other spectroscopic techniques, most especially EPR, must be employed.

In addition to determining the ferric state of KatG, UV-visible absorption can also be used to detect the higher oxidation state intermediates formed when KatG is reacted with its substrates by rapid reaction kinetics. Indeed, when ferric KatG reacts with peroxides, a new species is formed. If one equivalent of H_2O_2 or peracetic acid is used, there is little or no shift in the Soret band, but about a 40% hypochromicity is observed along with a broad increase in absorbance above 520 nm (Fig. 1.28) [126, 144]. These are signatures of a ferryl compound I-like intermediate. If m-chloroperbenzoic acid or 2-methyl-1-phenyl-2-propyl hydroperoxide (MPPH) is used, the Soret band red shifts to ~ 416 nm and the subsequent β and α transitions are detected at ~ 530 and ~ 560 nm respectively. These transitions are typical of a compound II-like intermediate [120, 126, 149]. Also, the one-electron reduction of compound I readily forms compound II. These species for compound I and II contain a ferryl (i.e., Fe^{IV}=O) heme intermediate. In contrast, a ferric superoxide (i.e., Fe^{III}-$O_2^{\bullet -}$) intermediate can also be detected when KatG is reacted with excess concentrations of H_2O_2. Here, the Soret band also red shifts to ~ 418 nm and the β and α transitions are also red shifted to ~ 540 and ~ 570 nm respectively [120, 126, 149]. So, both ferryl and ferric superoxide KatG heme states are low spin states (Fig. 1.28).

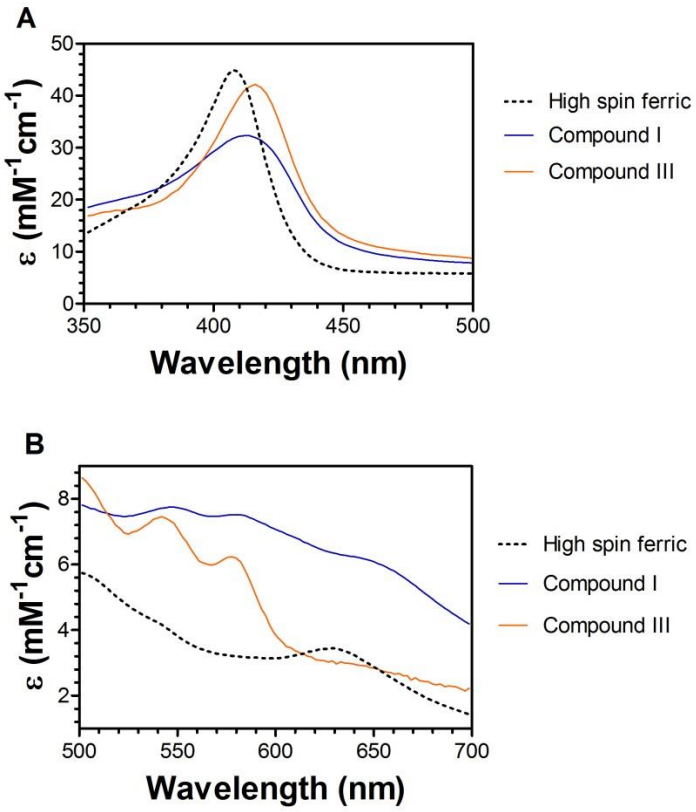

Figure 1.28. Typical absorption spectra of KatG in the Soret (A) and charge transfer (B) regions.

1.9.2. Evaluation of heme states by EPR

While UV-visible absorption provides a largely qualitative understanding of the population of spin and coordination states which contribute to the ferric form of a given heme protein, EPR is able to provide a much more definitive description of the states present, and their relative contribution to the whole. Simultaneously, UV-visible spectra can be obtained for ferryl (Fe^{IV}=O), ferrous (Fe^{II}) and compound III or oxyperoxidase (i.e., Fe^{III}-$O_2^{\bullet -}$) states where these forms are silent to at least standard perpendicular mode EPR measurements. Integer spin systems (e.g., high-spin Fe^{II} [S = 2] and Fe^{IV}=O [S = 1 and S = 2]) are accessible by parallel mode EPR measurements, but these will not be addressed here.

For the purposes of this dissertation, EPR was useful for evaluating the structural specifics of the ferric KatG state, and from a kinetic perspective, its disappearance upon reaction with H_2O_2 and reemergence upon H_2O_2 depletion. Although the other iron states were not observable in our EPR experiments, KatG protein-based radicals formed as a result of reactions with H_2O_2 were. EPR techniques applied to both are described in greater detail here.

EPR is a spectroscopic technique that measures the absorption of microwave radiation by a paramagnetic species within a molecule when placed in an external magnetic field. To be detectable by EPR, a species must have unpaired electrons. For this reason, evaluation of the ferric state of KatG and its protein-based radicals can be monitored using EPR.

The interactions between an applied magnetic field and the dipole moment of an unpaired electron give rise to an absorption energy called the Zeeman effect (Fig. 1.29). The Zeeman energy is dependent on both the magnitude of the applied magnetic field and a proportionality factor (*g*) specific to a given paramagnetic species (**Eqn. 1.5**).

Zeeman energy (ΔE) = $h\nu = g\beta B_0 m_s$ (**1.5**)

Here, h is Planck's constant (6.62 x 10^{34} J s^{-1}), ν is operating frequency of the radiation of the spectrometer, B_0 is the strength of the applied magnetic field in Tesla, β is the Bohr magneton (9.274 x 10^{-24} J^{-1}), and m_s is the electron spin quantum number. Each electron possess a magnetic moment and spin quantum number s = ½ with magnetic components m_s = +1/2 and m_s = -1/2 attributed to it. The electron's magnetic moment can either be aligned parallel (m_s = +½) or antiparallel (m_s = - ½) to a magnetic field.

The *g*-factor or a species specific proportionality factor relates the Zeeman splitting of a paramagnetic species to the applied magnetic field. It reflects the nature of interaction between the applied magnetic field and the unpaired electron. Also, the *g*-factor gives information on the position, neighbors, and other interactions with unpaired electrons. The *g*-factor of a free unpaired electron is isotropic with an exact value of 2.0023. In contrast, the *g*-factor for complex paramagnetic species is dependent on the orientation of the molecule in the external magnetic field, hence their *g*-factor is a tensor. So, the degree of spin orbit coupling reflects on the magnitude of *g*-anisotropy. For instance, the *g*-factor of small organic radicals all have *g*-factors very similar to that of the free electron while for transition metal ions, the *g*-factors are substantially different from that of a free electron because of a larger spin orbit coupling. Also, the spin states of metal ions can be very different from one another by EPR.

EPR spectra are recorded as the first derivative because the absorption spectrum is very broad (Fig. 1.29). Most commonly, EPR spectrometers run at constant frequency (e.g., X-band ~ 9.5 GHz), and a sweep of the applied magnetic field is performed. Given that h and β are also constant, the value of g for a given species will correspond to the magnitude of B.

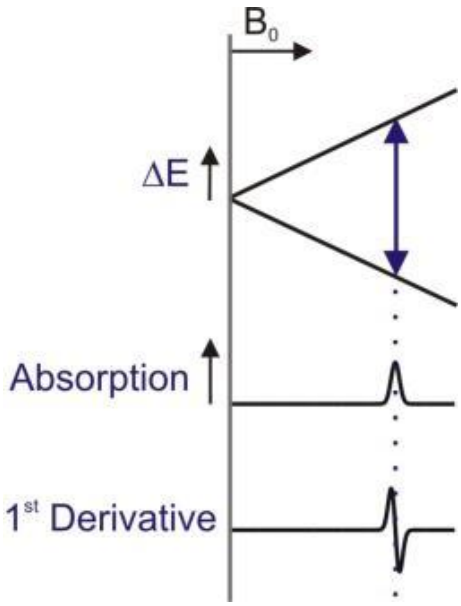

Figure 1.29. EPR spectra showing splitting of the spin states of the electron with absorption and first order derivative.

Further, the *g*-factor will also depend on orientation of the magnetic field relative to the paramagnetic species, meaning it is anisotropic. Depending on the orientation of the magnetic field along the *x*, *y* and *z* axes, the *g*-factor can divide into as many as three different *g*-values, producing three types of symmetry (isotropic, rhombic, and axial) (Fig. 1.30). The isotropic is observed when the *g*-values in the *x*, *y*, and *z* directions are equal ($g_x = g_y = g_z$). In contrast, when two *g*-values are equal, axial splitting is evident. The two equal *g*-values are perpendicular to the *x* and *y* directions ($g\perp$) while the unique *g*-value is parallel to the z-axis ($g_\parallel$). Two types of axial signals are possible ($g_\parallel > g\perp$ and $g_\parallel < g\perp$). Finally, rhombic signals arise when the three *g*-values are different ($g_x \neq g_y \neq g_z$). Hyperfine interactions give rise to splitting of EPR lines. These are interactions between the spins of electrons and their applied magnetic field.

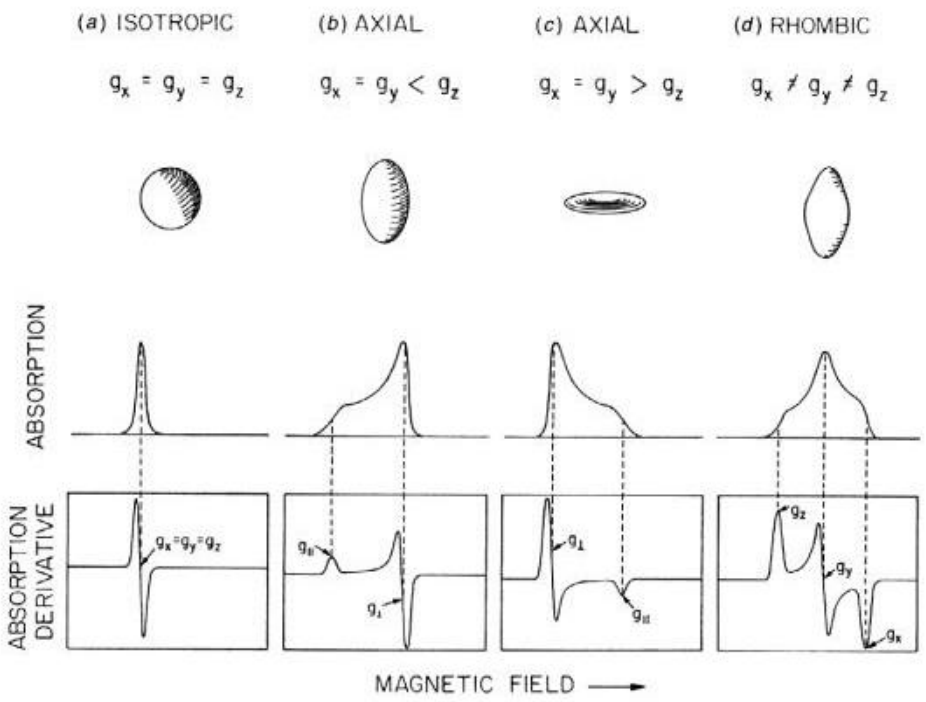

Figure 1.30. Three different classes of anisotropy showing their absorbance and first derivatives [150].

EPR spectra for KatG routinely indicate a mixture of at least two high spin states. These species are distinguished by differences in *g*-tensor anisotropy. This is most apparent in the $g \sim 6$ region of the KatG EPR spectrum. There is often substantial broad rhombic ($g_x \sim 6.6$ and $g_y \sim 5.1$, $g_z \sim 1.95$) and a narrow rhombic ($g_x \sim 6.0$, $g_y \sim 5.6$ and $g_z \sim 1.99$) contribution to the spectrum, and an intermediate species has also been detected ($g_x \sim 6.3$, $g_y \sim 5.3$ and $g_z \sim 1.97$) (Fig. 1.31) [100, 112, 148]. The distribution between these different high spin states appear to correlate with the distribution of H_2O within the active site, particularly the extent to which a H_2O molecule coordinates to the heme's sixth coordination site on the distal side. As such, the distributions of these states are sensitive to buffer type, pH, age of protein, mutations around the enzyme's active site and the type of substrates used [100, 112, 129, 139, 148, 151].

1.9.3. Detection of protein-based and porphyrin-based radicals

Tyrosyl and tryptophanyl radicals are the most widely studied protein-based radicals. These types of radicals have been assigned using a combination of mutagenesis, selective deuteration of Trp and/or Tyr residues, rapid freeze quench EPR, and ENDOR spectroscopies. For example, a tyrosyl radical has been identified in *M*tKatG after its reaction with H_2O_2, tryptophanyl radicals have been detected in *Bp*KatG and *Sy*KatG after their reactions with peracetic acid while the proximal tryptophanyl radical has been identified in CcP after its reaction with H_2O_2 [127, 129-132, 140, 143]. Most protein-based radicals have a characteristic line shape unless they are ferromagnetically coupled to a nearby paramagnetic center. For example a tyrosyl radical coupled to Cu metal has been identified in galactose oxidases, with a distinct line shape [152]. Tyrosyl radicals could have different

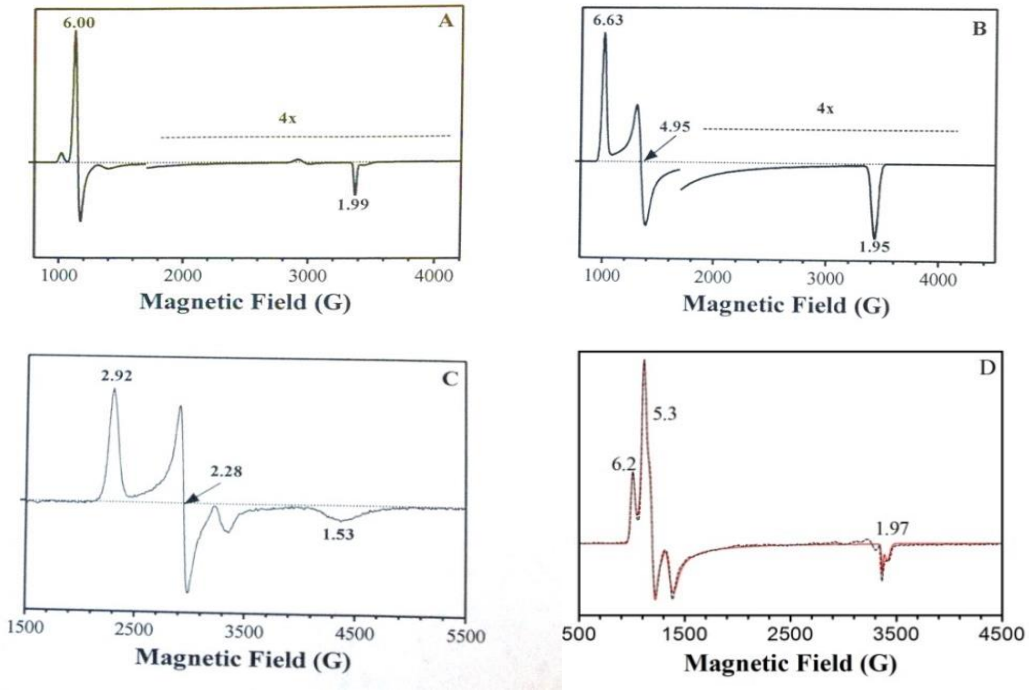

Figure 1.31. Simulated EPR spectra observed for catalase-peroxidases (KatG). Panel A shows 6 c high-spin ferric KatG. Panel B shows 5 c high spin rhombic. Panel C shows a low spin spectrum for KatG while Panel D shows a mixture of high spin rhombic (broad, narrow and intermediate) for Q293V KatG species.

line shapes even though they are not coupled to a paramagnetic center. The differences in these types of radicals have been attributed to their respective environments which translates to different *g*-values observed [153]. Despite the differences in the overall EPR spectra for tyrosyl radicals, the spin distribution between the unpaired electrons is similar. The subtle differences may only arise from dihedral angles between the β methylene hydrogens, β methylene carbons, and the p_z orbital on C1 ring of tyrosines [153].

The effect of isotope substitution on EPR spectra has been used to determine the structure, orientation and electronics of protein-based radicals. The subsequent section will focus on the use of EPR to identify protein-based radicals for the intermediates of heme. When ferric heme of a non-animal peroxidase is reacted with peroxides, a radical is formed either on the macrocyclic porphyrin ring or on an oxidizable amino acid. The former has been characterized in heme peroxidases referred to as compound I. The porphyrin π cation radical is very broad (~ 2000 G) with effective *g*-values of 2.35 for $g_{\perp}$ and 2.00 for $g_{\parallel}$ [144, 147]. The latter has been identified to be either a tyrosyl, tryptophanyl or a mixture of both radicals. The *g*-values of tyrosyl and tryptophanyl radicals at X-band (9 GHz) are similar. To unequivocally distinguish between these radical types, multi-frequency and or multi-field EPR and even isotopic labeling are required.

The most commonly used EPR frequency (i.e., 9 GHz) can be used to assign *g*-values (Fig. 1.32 A). However, it is not sufficient to resolve *g*-tensor anisotropies for different protein-based radicals because they are broadened by both field-dependent and independent terms. As such, it is somewhat difficult to distinguish between different organic (including protein-based radicals). Higher magnetic fields (and the higher frequencies that go with

them) permit resolution of *g*-anisotropies at the *x*, *y*, and *z*-directions, the first order spectrum is observed and the magnetic field can also quantize the electron and nuclear spins. With multi-frequency/multi-field EPR, one can more definitely identify the source of a protein-based radical (Tyr, Trp, Gly, etc) based on their line shapes and *g*-values (Fig. 1.32 B). Ivancich and coworkers have consistently utilized multi-frequency EPR to distinguish between different KatG protein-based radicals [129-131, 140]. Tyrosyl radicals have been noted to have modestly higher *g*-values (g_x = 2.009, g_y = 2.0034, and g_z = 2.0018) than tryptophanyl radicals (g_x = 2.0033, g_y = 2.0024, and g_z = 2.0021) [154]. Contrary to a regular tyrosyl radical, a structurally or electronically modified tyrosyl radical has been noted to have a lower g_x component of about 2.006 [124]. The electronic modification could be due to hydrogen bond of the radical with the phenolic oxygen. In this dissertation, X-band and multi-frequency EPR has been used to identify and distinguish between different KatG protein-based radicals that were detected in freeze-quenched samples of KatG or its variants reacted with H_2O_2 in the presence and absence of PxEDs.

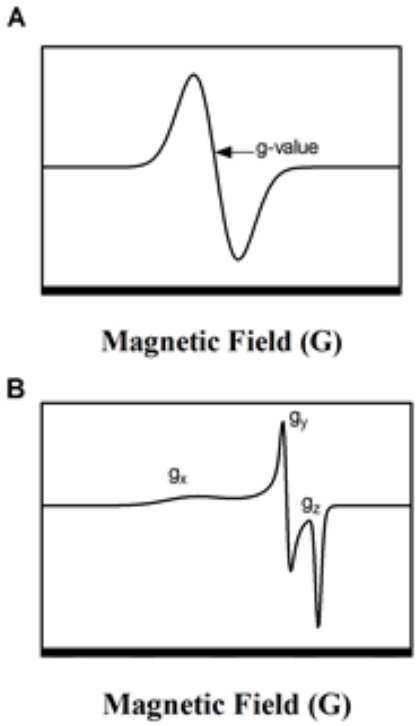

Figure 1.32. Simulated spectra of protein-based radical at 9.35 GHz, X-band (A) and at 285 GHz, J-band (B).

Chapter Two: Proximal Tryptophan Participation in Catalase-Peroxidase Inactivation: Peroxidatic Electron Donors and the Stimulation of Catalase Activity.

Abstract

Contrary to prediction, peroxidatic electron donors (PxEDs) do not inhibit but *stimulate* KatG catalase activity tenfold or more, substantially expanding the pH range of efficient catalatic H_2O_2 degradation by KatG. Without PxED, a compound III-like state corresponds to the early and most rapid rates of H_2O_2 decomposition; this gives way to a mixture of states at H_2O_2 depletion, followed by very slow re-emergence of the ferric enzyme. This suggested inactive intermediates accumulated during H_2O_2 consumption. EPR showed a methionine-tyrosine-tryptophan (MYW) cofactor narrow doublet radical early in reactions with H_2O_2. However, at H_2O_2 depletion, a broad singlet species consistent with a proximal tryptophanyl radical ($W321^{\bullet+}$) was observed. Concomitant with the return of ferric KatG, more remote and less intense radicals were detected. W321F KatG sustained rapid consumption of H_2O_2 longer than did wild-type KatG, and a more rapid return of ferric enzyme was observed after H_2O_2 depletion. Compound III-like heme and a $MYW^{\bullet+}$ narrow doublet identical to wild-type were observed early, but at H_2O_2 depletion a starkly different radical was detected. PxEDs stimulated KatG by preventing accumulation of inactive states, the primary mechanism of which is off-catalase oxidation of W321. A new paradigm of mutual synergy between KatG catalase and peroxidase is proposed that carries important ramifications for microbial defenses against peroxides.

2.1. Introduction

Catalase-peroxidase (KatG) is a bifunctional heme-dependent enzyme found in bacteria and lower eukaryotes [155] which is integral to the defense of these organisms against H_2O_2 toxicity [37, 156]. KatG function appears to carry especially important ramifications for plant and animal pathogens [90, 157, 158] because these organisms are likely to encounter excess H_2O_2 produced by their host's immune response (e.g., oxidative burst). Among these enzymes, the function of KatG in *Mycobacterium tuberculosis* (*Mt*KatG) is especially important because it is the only catalase-active enzyme carried by *M. tuberculosis* [89], and it activates the front-line antitubercular agent, isoniazid [94]. A large proportion of isoniazid-resistant *M. tuberculosis* strains carry mutations that alter KatG function [159, 160]. The mechanism of isoniazid activation and the molecular basis for how mutations to the *katG* gene interfere in said activation are the subjects of ongoing investigation [100, 124, 141, 161].

KatG catalyzes H_2O_2 disproportionation to produce H_2O and O_2 (i.e., it is a catalase). It does so with an apparent second-order rate constant similar to typical (i.e., monofunctional) catalases [101, 162] even though it bears no structural resemblance to these enzymes. Instead, it resides in the plant peroxidase-like superfamily with cytochrome *c* peroxidase (CcP), ascorbate peroxidase (APx), and even horseradish peroxidase (HRP) [64, 93]. Indeed, the active sites of CcP, APx, and KatG are virtually superimposable (Fig. 2.1) [70, 98, 104, 105, 107]. Not surprisingly, then, KatG also catalyzes H_2O_2 reduction to H_2O concomitant with the oxidation of a structurally diverse range of exogenous electron donors (i.e., it is a peroxidase). Its peroxidase activity is well within the range of other plant peroxidase-like superfamily members [101, 144, 162], but KatG is the only member of the entire

superfamily that possesses appreciable catalase activity.

Despite their striking active site similarities, KatG does possess structural features that distinguish it from other superfamily members. Among them are two large loops (LL1 and LL2) both of which are essential for KatG function [104, 105, 107, 112, 163]. Both also contribute to a much narrower channel to the active site heme, which among other things restricts access of many peroxidatic electron donors (PxEDs) to the heme edge [105, 112, 164, 165]. Additionally, LL1 bears an invariant tyrosine (Y229 by *Mt*KatG numbering) that participates in a unique methionine-tyrosine-tryptophan (MYW) adduct which serves as a protein-derived cofactor [104, 105, 107, 122, 123]. Substitutions of any of the residues of the adduct consistently produce KatG variants with very little catalase activity but peroxidase activity comparable to the wild-type enzyme [113, 120, 121, 161, 165-168].

Commensurate with an active site completely distinct from typical catalases, KatG also operates by a novel catalatic mechanism (Fig. 2.2) [100, 124-127, 135, 136, 142, 169]. The first step is common to all heme-dependent catalases and peroxidases; H_2O_2 oxidizes the ferric heme of KatG to form compound I (i.e., Fe^{IV}=O[porphyrin$^{\bullet+}$]). At this point, KatG diverges from the canonical catalase mechanism by reducing the porphyrin radical *via* an intramolecular electron transfer from the MYW adduct, generating the KatG-unique compound I* (i.e., Fe^{IV}=O[MYW]$^{\bullet+}$). Reaction of compound I* with a second equivalent of H_2O_2 produces compound III* (i.e., Fe^{III}-$O_2^{\bullet-}$[MYW]$^{\bullet+}$). A recent report posits that the generation of compound III* may be facilitated by deprotonation of the MYW$^{\bullet+}$, permitting formation of perhydroxy-MYW and bridged peroxy (Fe^{III}-OO-MYW) similar to the proposed role of the distal histidine in monofunctional catalases [136]. Finally, the MYW adduct radical is proposed to accept an electron from the heme-bound superoxide, resulting

in the formation of the resting, ferric enzyme and the release of O_2 [124, 127, 142]. This ultimate electron transfer has been linked to the conformation of an arginine residue (the so-called arginine switch) adjacent to the KatG active site. The arginine switch is invariant among KatGs (R418 in *Mt*KatG), and its conformation is pH dependent [133, 134, 139, 170]. Structures solved for KatG at pH 8.5 show the guanidinium moiety of the switch in a salt bridge with the tyrosyl phenoxide anion of the MYW cofactor (*in* Fig. 2.1). At pH 4.5, the arginine side chain is oriented away from the MYW adduct and toward KatG's surface (*out* Fig. 2.1). At pH 6.5, corresponding roughly to the optimum pH for catalase activity, this arginine equally populates both conformational states [133, 134]. Substitution of Arg418 with Leu, Ala, or Asn (but not Lys), sharply diminishes the catalase activity of KatG [134, 139, 142]. The mechanism by which Arg418 facilitates catalatic turnover is still under investigation. In general, its occupation of the *out* conformation is connected with MYW oxidation, whereas the *in* conformation is connected with $MYW^{\bullet+}$ reduction [134-136, 142, 171]. Interestingly, a recent computational investigation suggests R418 facilitates rotation of the Y and W aromatic rings with respect to one another, enabling $MYW^{\bullet+}$ reduction by a Fe^{III}-$O_2^{\bullet-}$ heme [135].

What, then, is the place of peroxidase activity and PxEDs in KatG catalysis? As both catalase and peroxidase catalytic mechanisms involve the H_2O_2-dependent formation of compound I, all that should differ between the two activities is the route by which the ferric state of the enzyme is regenerated. As outlined above, catalatic turnover requires the oxidation of a second H_2O_2, however with peroxidases, an exogenous (usually aromatic) electron donor is oxidized instead. Typically, compound I is reduced by one electron to produce compound II (Fe^{IV}=O), and the corresponding PxED radical (Fig. 2.2). A second

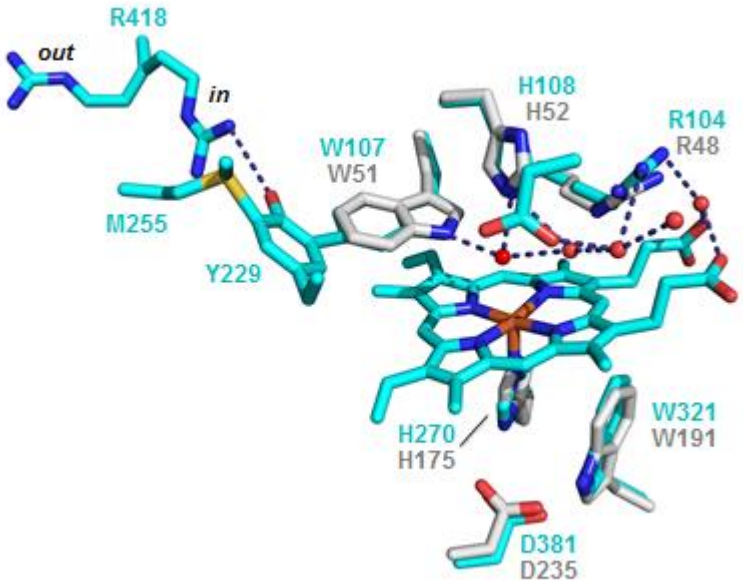

Figure 2.1. Superposition of key residues in the active sites of KatG and cytochrome *c* peroxidase and the catalase and peroxidase catalytic cycles of KatG. Residues corresponding to the structure of KatG are annotated and shown with carbons in cyan, and those corresponding to cytochrome *c* peroxidase (C*c*P) are annotated and shown with carbons in grey. The active site waters (red spheres) and heme are from KatG, and the two conformations (*in* and *out*) of the arginine switch (R418) are shown. KatG residue numbering is according to the *M. tuberculosis* enzyme *Mt*KatG. This image was generated using MacPyMOL 1.6.0.0 [172] using coordinates from PDB accession 2CCA [108] and 2CYP [173] for *Mt*KatG and yeast C*c*P, respectively.

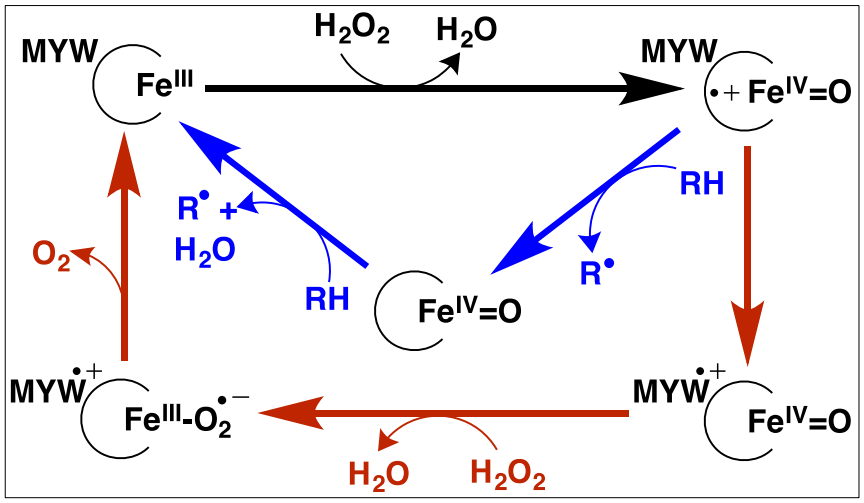

Figure 2.2. Putative superposition of the catalatic and peroxidatic cycles of KatG is shown. The reaction common to both cycles is shown with black arrows, those corresponding to catalatic turnover are shown in red, and those corresponding to peroxidatic turnover are shown in blue.

single-electron transfer returns the enzyme to the ferric state and produces a second equivalent of PxED radical. According to this model one would anticipate that peroxidase and catalase activities should be mutually antagonistic, an in particular, PxEDs should inhibit catalase activity. Indeed, the first published report on a catalase-peroxidase showed that the classical peroxidase electron donor *o*-dianisidine did inhibit catalase activity at pH 7 [137]. However, we have recently shown that a number of PxEDs can stimulate catalase activity by over an order of magnitude [138]. Interestingly, this synergistic effect is most prominent at lower pH (i.e., ~ pH 5), a condition that coincides with antimicrobial defenses like the oxidative burst. Clearly, the interrelationship between the catalatic and peroxidatic mechanisms of KatG is more complex than has been previously appreciated.

In this report, we investigate the mechanism by which PxEDs stimulate KatG catalase activity. In the absence of a PxED, there was a stark disparity between the conclusion of H_2O_2 consumption and re-emergence of the enzyme's ferric state, suggesting the accumulation of catalase-inactive intermediates. We surmised that inactivation might occur due to off-catalase electron transfer, and the enzyme's proximal tryptophan (W321) seemed to be a likely candidate for such off-pathway events. To test these hypotheses, we replaced the proximal tryptophan with non-oxidizable phenylalanine (W321F KatG) and compared it to wild-type KatG (*wt*KatG). UV-visible stopped-flow, rapid freeze quench EPR, and steady-state kinetic analyses of both proteins were carried out in the presence and absence of PxEDs. Our results suggest that catalase-inactive intermediates accumulate due to off-mechanism oxidation, primarily of W321, and PxEDs stimulate KatG catalase activity by preventing the accumulation of inactive intermediates. This informs a new synergistic model

to understand the interplay of KatG's two most dominant activities.

2.2. Experimental Procedures

2.2.1. Materials. Hydrogen peroxide (30%), ampicillin, hemin, imidazole, calcium chloride hydrate, sodium dithionite, 2,2'-azino-bis(3-ethylbenz-thiazoline-6-sulfonate) (ABTS), 3,3'-dimethoxy-benzidine (*o*-dianisidine), *N,N,N',N'*-tetramethyl-*p*-phenylenediamine di-hydrochloride (TMPD), 3,3',5,5'-tetramethylbenzidine dihydrochloride hydrate (TMB), chlorpromazine (CPZ), pyrogallol, and $_{L}$-ascorbic acid, were from Sigma-Aldrich (St. Louis, MO). Mono- and dibasic sodium phosphate, sodium acetate trihydrate, sodium chloride, potassium chloride, magnesium sulfate, magnesium chloride and tetracycline hydro-chloride were purchased from Fisher (Pittsburg, PA). T4 DNA ligase, *Pfu* polymerase and *E. coli* (XL-1 Blue) were obtained from Agilent (La Jolla, CA). All oligonucleotide primers were purchased from Invitrogen (Carlsbad, CA). All restriction enzymes and Phusion High-Fidelity PCR Master Mix with GC Buffer were obtained from New England Biolabs (Beverly, MA). Bugbuster, Benzonase nuclease, nickel-nitrilotriacetic acid (Ni-NTA) resin were obtained from Novagen (Madison, WI). Isopropyl-β-$_{D}$-thiogalactopyranoside (IPTG) was obtained from Gold Biotechnology (St. Louis, MO). Macro-Prep High Q resin and Buffer Exchange columns (10DG) were purchased from BioRad (Hercules, CA). Centrifugal filter units (50 kDa cutoff) were acquired from Millipore (Billerica, MA). All buffers and media were prepared using water purified through a Barnstead EASYpure II UV ultrapure water system (18.2 MΩ/cm resistivity).

2.2.2. Mutagenesis. Site-directed mutagenesis was carried out by applying the "Round-the-Horn" approach [174] to the construct we use for the expression of wild-type *Mt*KatG. This construct, pMRLB11, is a pET23b-derived plasmid bearing the *M. tuberculosis katG*

gene and was obtained from the TB Vaccine Testing and Research Materials Contract at Colorado State University. The sense strand primers designed for M255I (5'-CGC**ATC***GCA*ATGAACGACGTCGAAACAGCGGC-3'), Y229F (5'-GGGCTGATC**TTT**GTGA-ACCCGGAGGCG-3'), W107F (5'-CG**TTT**CAC-GCT*GCA*GGCACCTACCGCATCC-3'), and W321F (5'-GAG*GTG*GTA**TTT**ACGAACACCC-CGACGAAATGGGAC-3') substitution indicate the sites of codon replacement (bold) as well as mutations designed to introduce diagnostic restriction digest sites for screening (italics). This approach allowed us to generate reverse primers without substitutions for M255I 5'-CCGAAA-CGTCTCGCGAATGTCGACCGCC-3', Y229F 5'-CCCATC-TGCACGCGGCCAGCG-3', W107F 5'-CCATCCGGATAAACAGCGGCCC-GTAGTGGC-3', and W321F 5'-GATGCCGC-TGGTGATCGCGTCCTTACCG-3'. All primers were modified by 5'-phosphorylation to allow for blunt-end ligation of PCR products. PCR for generation of all variants was carried out using *Phus*ion High Fidelity polymerase (New England Biolabs, Beverly, MA) in GC Buffer-containing Master-Mix and 3% DMSO. The PCR products were treated with *Dpn* 1 to eliminate the starting template and ligated using T4 DNA ligase. The ligation products were used to transform *E. coli* (XL-1 Blue) by a standard heat shock procedure. Transformants were selected using ampicillin-containing media, and candidate plasmids were screened by *Bsa*AI restriction digest. Successful candidates were sent for full DNA sequence analysis (Davis Sequencing, Davis CA) to verify that the intended mutations were present and that no unintended mutations were generated.

2.2.3. Protein expression and purification. *E. coli* C41(DE3) cells bearing the heme protein expression plasmid pHPEX3 [175] were transformed with the appropriate expression

construct, and transformants were selected on the basis of tetracycline/ampicillin resistance. Expression of wild-type *Mt*KatG and all variants was carried out as previously described [138]. As with wild-type *Mt*KatG, all variants were expressed in a soluble form. Thus, their purifications were carried out as reported previously [138], with the exception that lysis was carried out by sonication. A Branson 250 Sonifier (Danbury, CT) fit with a standard tip was set to constant output and 3.5 duty. Sonication was carried out in eight cycles (42 s on, 42 s off). Benzonase nuclease (250 U) was added to the lysate following sonication.

2.2.4. UV-visible spectra and activity assays. Following purification, UV-visible spectra for wild-type *Mt*KatG and its variants were evaluated as previously described [138]. Molar absorptivities were determined using the pyridine hemichrome assay [176]. The absorption features, Soret band, molar absorptivities, optical purity ratios A_{408}/A_{281} (i.e., R_Z values) for wild-type *Mt*KatG and its variants are provided in Table 2.1.

Table 2.1. UV-visible absorption characteristics of MtKatG and variants

Protein	Absorption Features			
	Soret (λ)	CT[a] 2	CT 1	RZ[b]
MtKatG	408	500	633	0.62
W321F KatG	408	500	633	0.62
W107F KatG	407.5	500	633	0.4
Y229F KatG	407.5	500	633	0.43
M255I KatG	407.5	500	633	0.4

[a]CT = charge transfer transition. CT1 is usually near 640 nm, and CT 2 is usually near 500 nm.

[b]RZ = Reinheitzahl ratio: Ratio of absorbance at the Soret λ_{max} versus absorbance at 280 nm.

Peroxidase activity was evaluated as previously described [138] by monitoring ABTS (the PxED) oxidation to $ABTS^{\bullet+}$ (ε_{417} = 34.7 mM^{-1} cm^{-1}) [177]. In evaluating the effect of H_2O_2 concentration on peroxidase activity, ABTS concentration was held constant at 0.1 mM. In experiments evaluating the effect of ABTS concentration, H_2O_2 concentration was held constant at 1.0 mM. All peroxidase assays were carried out at room temperature in 50 mM acetate, pH 5.0. The concentration of the enzyme used in all assays was 20 nM. Unless otherwise specified, catalase activity was evaluated by monitoring O_2 production over time using a Clark-type O_2-sensitive electrode (Hansatech, Pentney, Norfolk, England) as previously described [138]. In specified experiments, catalase activity was evaluated spectrophotometrically by monitoring a decrease in H_2O_2 concentration over time at 240 nm (ε_{240} = 39.4 M^{-1} cm^{-1}) [178]. Analyses of steady-state kinetic data were carried out as described previously [138] to obtain kinetic parameters k_{cat}, K_M, and k_{cat}/K_M. In all situations where these terms are applied, k_{cat} is the asymptotic maximum rate divided by the concentration of holo-enzyme as estimated by heme concentration. The apparent K_M is not intended to refer to anything more than the concentration of substrate necessary to produce ½ of the maximum rate, and k_{cat}/K_M is considered the catalytic efficiency.

2.2.5. Yield of $ABTS^{\bullet+}$ vs. H_2O_2 consumed. The extent of ABTS oxidation was measured by setting up reactions containing 0.1 mM ABTS, 20 nM enzyme, and varying concentrations of H_2O_2 (i.e., 0.1 – 5 mM) and allowing them to proceed to completion (at least 10 minutes) as previously described [138].

2.2.6. Stopped-flow. Heme intermediates formed by wild-type and W321F *Mt*KatG under steady-state conditions were observed using a PC-upgraded SX18.MV rapid reaction analyzer from Applied Photophysics (Leatherhead, UK). As described previously [138], in

order to more clearly observe absorption due to heme intermediates, we included ascorbate to scavenge the radical oxidation products of peroxidatic electron donors (e.g., $ABTS^{\bullet+}$) [138, 179, 180]. Single-mixing experiments were set up such that 6 μM wild-type or W321F KatG was placed in syringe A in 5 mM phosphate buffer, pH 7.0. Syringe B contained 0.2 mM ascorbate, 0.2 mM ABTS, and varying concentrations of H_2O_2 in 100 mM acetate buffer, pH 5.0.

2.2.7. Freeze-quench preparation of EPR samples. Wild-type and W321F KatG were each concentrated to ~300 μM using an Amicon Ultra-4 centrifuge filter (MW cutoff of 50 kD). One syringe contained ~300 μM enzyme in 5 mM phosphate, pH 7.0, and the other syringe contained 667 molar equivalents of H_2O_2 in 100 mM acetate buffer, pH 5.0. Reactions testing the impact of PxED included ABTS (2.0 mM) and ascorbate (4.0 mM) along with H_2O_2.

EPR samples were prepared by mixing equal volumes of solution from each syringe. Each reaction was quenched by freezing after the appropriate time following mixing. Samples frozen less than 1 s after mixing were quenched by spraying the reaction mixture directly into liquid ethane (-150°C) by a standard rapid quench procedure using a System 1000 Chemical/Freeze Quench Apparatus (Update Instruments, Inc.), and the sample age was determined by the length of the ageing loop and velocity of the motor driving the syringes. For reactions between 1 and 30 s, the samples were still quenched with liquid ethane, however, a modified flow-pause-flow freeze-quench procedure was used in which the quenching time was determined by the pause duration. For reaction times longer than 30 s, reactions were initiated by hand mixing. The samples were centrifuged to remove excess bubbles, transferred to quartz EPR tubes, and quenched manually in cold isopentane (-130

°C). Samples were packed into EPR tubes and stored in liquid N_2 until EPR spectra could be recorded.

2.2.8. EPR measurements. All X-band (9 GHz) EPR spectra were collected using a Bruker EMX spectrometer operating in perpendicular mode at 100 kHz modulation frequency in a 4119HS resonator. The spectrometer was equipped with an ESR910 liquid helium cryostat and an ITC503S temperature controller (Oxford Instruments), and unless otherwise indicated, spectra were recorded at 4.5 K. Instrument parameters, unless otherwise indicated, were as follows: microwave frequency, 9.393 GHz; modulation amplitude, 2 G; modulation frequency, 100 kHz; microwave power, 1 mW; time constant, 163.84 ms; sweep time 335.54 s; number of scans, 1; conversion, 327.68 ms; resolution, 1024 point; harmonic 1st; receiver gain, 1.0 x 10^4; and phase 0 deg. Power saturation for select species was examined by fitting normalized signal intensities using equation **1**, where $P_{½}$ is the microwave power at half saturation and *b* describes the contribution from inhomogenous broadening [181].

$$\left(I/\sqrt{P}\right)\Big/\left(I/\sqrt{P}\right)_o = 1\Big/(1 + P/P_{1/2})^{b/2} \qquad [\mathbf{1}]$$

2.3. Results and Discussion

2.3.1. PxEDs not redox-cycling surrogates for the MYW adduct. We previously reported that several classical peroxidatic electron donors (PxEDs) stimulate the catalase activity of *Mt*KatG [138]. The effect was most dramatic (up to 15-fold) under conditions conducive to peroxidase activity (i.e., low pH and $[H_2O_2]$ ~1 mM). In addition, the ratio of PxED oxidized to H_2O_2 consumed (i.e., $[ABTS^{\bullet+}]/[H_2O_2$ consumed]) was less than 0.01. One

possible mechanism for PxED-dependent stimulation would have the PxED redox cycle in place of MYW. We produced W107F, Y229F, and M255I KatG variants. As has been demonstrated elsewhere [113, 114, 120, 121, 166, 168], all of these variants lacked catalase activity but retained peroxidase activity (Table 2.2). Catalatic O_2 production could not be imparted to any of these variants by inclusion of PxEDs. Thus, we concluded that PxEDs do not stimulate KatG catalase activity by acting as redox-cycling surrogates for the MYW adduct.

2.3.2. Conclusion of H_2O_2 consumption vs return of resting KatG. Alternatively, PxEDs may stimulate KatG catalase activity by preventing the accumulation of catalase-inactive intermediates. Using optical stopped-flow methods, we monitored the KatG heme state concomitant with catalatic H_2O_2 consumption. We have consistently observed that the return of the enzyme's ferric state lags far behind the cessation of H_2O_2 consumption. For example, in reactions of 3 μM KatG with 667 molar equivalents of H_2O_2 at pH 5.0 (Fig. 2.3), H_2O_2 consumption (monitored at 240 nm) ceases at about 6 s, but it takes more than 50 s for the ferric enzyme (monitored at 408 nm) to completely reemerge. These data are consistent with the progressive accumulation of catalase-inactive intermediates during turnover.

Recent mechanisms proposed for KatG catalatic turnover invoke intramolecular electron transfer from and to the MYW covalent adduct, transiently forming a catalytically essential MYW cation radical ($MYW^{\bullet+}$) [135, 136]. Thus, we propose that off-pathway electron transfers may account for accumulation of inactive intermediates, a problem that could potentially be resolved by inclusion of PxEDs. Given its propensity (observed experimentally and computationally) toward oxidation to form a radical intermediate [128, 130-132, 171], we also propose that the proximal tryptophan (W321 in *Mt*KatG) is a likely

Table 2.2. Catalase and peroxidase kinetic parameters of *Mt*KatG and variants.

Activity	KatG	Parameter			
		k_{cat} (s^{-1})	K_M (mM)	k_{cat}/K_M ($M^{-1}s^{-1}$)	k_{app} ($M^{-1}s^{-1}$)
Catalase (pH 7.0)[a]	*Mt*KatG	7736 ± 82	7.0 ± 0.3	1.1×10^6	-
	W321F	7830 ± 81	3.1 ± 0.2	2.5×10^6	-
Peroxidase[b] (H_2O_2)[c]	*Mt*KatG	17.2 ± 0.8	0.63 ± 0.04	2.7×10^4	-
	W321F	9.9 ± 1.44	0.26 ± 0.08	3.8×10^4	-
	W107F	72 ± 4	6.9 ± 0.08	1.0×10^4	-
	Y229F	2.7 ± 0.9	0.004 ± 0.001	6.8×10^5	-
	M255I	3.1 ± 0.1	0.28 ± 0.06	1.1×10^4	-
Peroxidase (ABTS)[d]	*Mt*KatG	25.0 ± 0.1	0.135 ± 0.002	1.9×10^5	-
	W321F	13.7 ± 0.1	0.118 ± 0.003	1.2×10^5	-
	W107F	28.2 ± 1.6	0.012 ± 0.001	2.4×10^6	-
	Y229F	2.75 ± 0.093	0.004 ± 0.0009	6.9×10^5	-
	M255I	1.89 ± 0.056	0.005 ± 0.0007	3.8×10^5	-
Catalase (pH 5.0)[e]	*Mt*KatG	168 ± 9	0.6 ± 0.1	2.8×10^5	$(9.2 \pm 0.3) \times 10^3$
	W321F	1390 ± 40	9 ± 1	1.5×10^5	-

[a]Activity was determined by H_2O_2 consumption observed at 240 nm at 23 °C in 100 mM phosphate buffer, pH 7.0.
[b]All peroxidase activity assays were performed at 23 °C in 50 mM acetate buffer, pH 5.0.
[c]Peroxidase parameters with respect to H_2O_2 were determined using 0.1 mM ABTS.
[d]Peroxidase parameters with respect to ABTS were determined using 1.0 mM H_2O_2.
[e]Activity was determined by O_2 production at 23 °C in 50 mM acetate buffer, pH 5.0.
[f]Kinetic parameters for the low-K_M component.
[g]Apparent second-order rate constant for the high-K_M component.

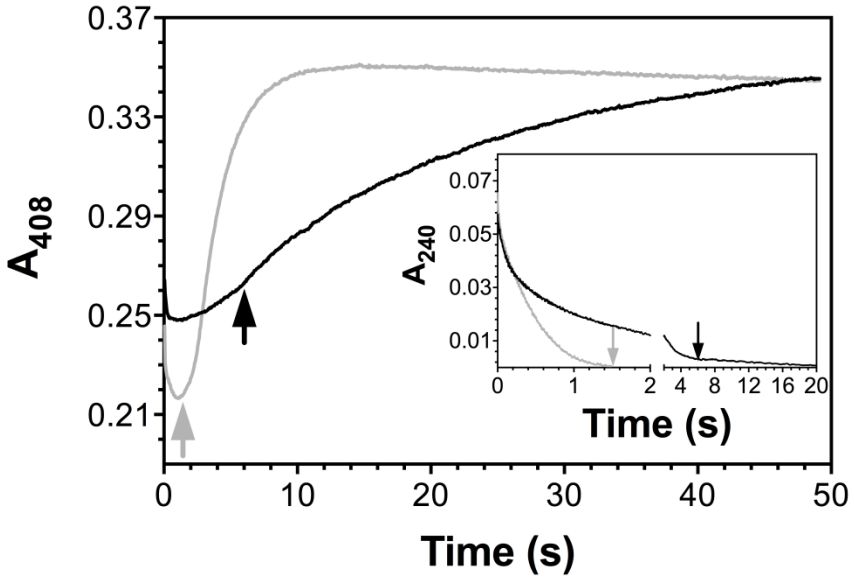

Figure 2.3. H_2O_2 consumption (inset) and return of the ferric state for *wt*KatG (black lines) and W321F KatG (gray lines). Reactions were carried out by stopped-flow and after mixing contained 3 μM enzyme and 2 mM H_2O_2. All reactions were carried out in 50 mM acetate buffer, pH 5.0, at 4°C. The arrows indicate the times in each trace corresponding to cessation of H_2O_2 consumption.

participant in off-pathway electron transfers and KatG catalase inactivation. In order to evaluate these hypotheses, we eliminated the proximal tryptophan as a site of oxidation by producing the W321F KatG variant and compared its properties to those of the wild-type enzyme.

2.3.3. wtKatG vs W321F: H_2O_2 consumption and heme states. Under standard catalase assay conditions (i.e., pH 7.0), our W321F KatG showed kinetic parameters nearly identical to the wild-type enzyme (Table 2.2). However, at pH 5.0, W321F KatG actually showed greater catalase activity (k_{cat} = 1390 ± 40 s^{-1}) than the wild-type enzyme (k_{cat} = 168 ± 9 s^{-1}). Evaluation of the reaction of 3 μM W321F KatG with 2 mM H_2O_2 by optical stopped-flow showed the same initial rate of H_2O_2 consumption as that observed for the wild-type enzyme (Fig. 2.3 - inset). However, the rate of peroxide consumption decreased more rapidly for the wtKatG than the W321F variant such that it took *wt*KatG roughly four times longer than W321F to consume a comparable quantity of H_2O_2. Furthermore, the return to the ferric state after H_2O_2 was consumed was nearly ten-fold faster for W321F than *wt*KatG.

Wild-type and W321F KatG showed nearly identical spectra 2.5 ms after mixing with 2.0 mM H_2O_2 (Fig. 2.4, blue traces). The Soret (λ_{max} near 415 nm) and Q bands at 542 and 578 nm are consistent with the putative Fe^{III}-$O_2^{\bullet-}$ intermediate compound III* [125, 126, 142]. However, at the time corresponding to H_2O_2 depletion (6 s for wild-type and 1.6 s for W321F), the spectra were distinct for each protein. For *wt*KatG, there was little if any shift in the Soret band (Fig. 2.4 A) and a broad nondescript increase in absorption at wavelengths above 520 nm (Fig. 2.4 B). Traces of a compound III-like species were still observable at 544 and 582 nm. Conversely, W321 showed a decrease in Soret intensity and blue-shift to about 410 nm (Fig. 2.4 C). There was a similar broad nondescript increase in absorption

Table 2.3. Effect of PxED on the apparent catalase k_{cat} of wild-type and W321F KatG.

PxED[a]	KatG k_{cat} (s^{-1})[b,c]	W321F k_{cat} (s^{-1})[b,c]
None	168 ± 9	1390 ± 40
ABTS	1601 ± 8	4760 ± 60
CPZ	2769 ± 75	3940 ± 40
TMPD	3835 ± 64	3770 ± 10
TMB	1774 ± 57	2640 ± 70
o-dianisidine	1756 ± 60	1620 ± 10
pyrogallol	227 ± 9	2690 ± 30
ascorbate	184 ± 21	570 ± 20

[a]PxEDs, when present, were at 0.1 mM.

[b]All catalase activities from O_2 production.

[c]All assays at 23 °C in 50 mM acetate, pH 5.0.

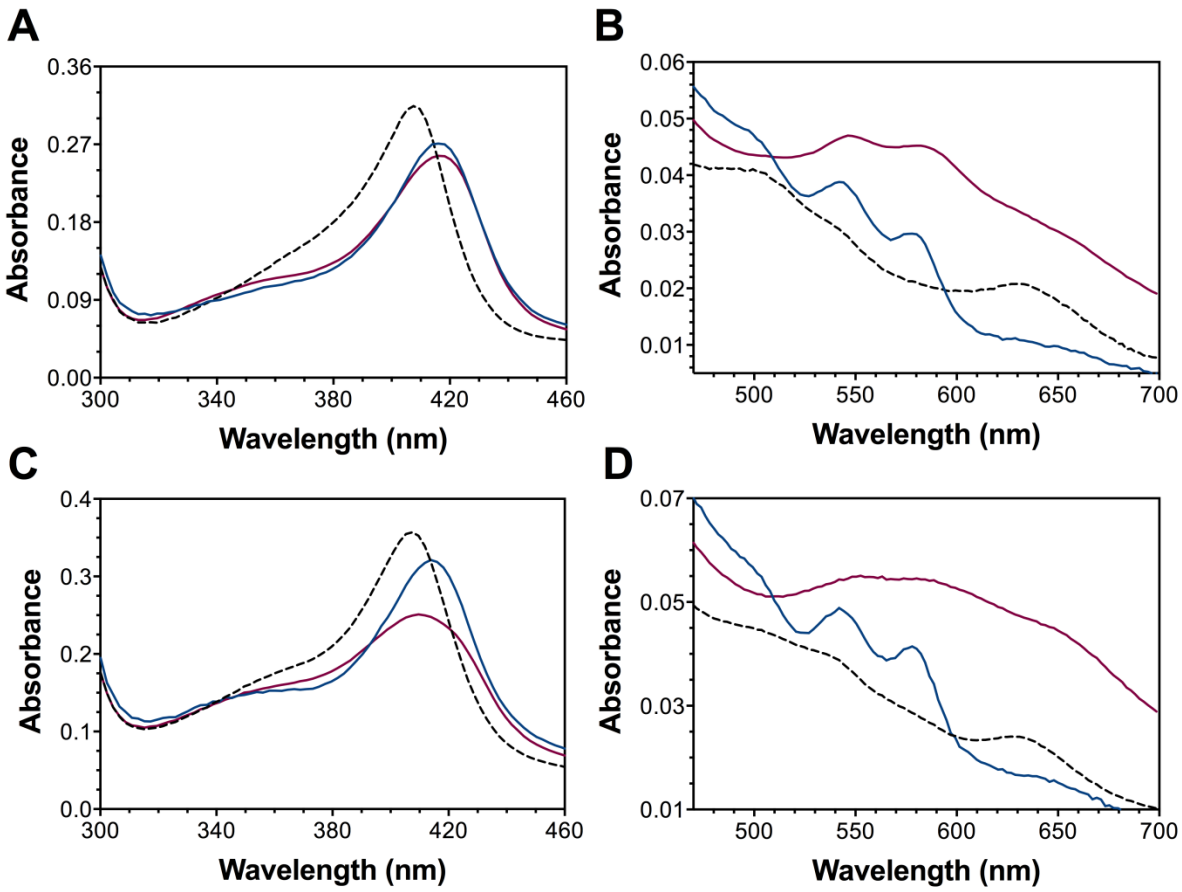

Figure 2.4. Spectra from reaction of wild-type and W321F KatG with H_2O_2. Wild-type (A and B) and W321F KatG (C and D) were reacted with 2 mM H_2O_2 by stopped-flow and spectra for the Soret band (A and C) and Q bands (B and D) were recorded throughout the reaction by diode array. Spectra obtained 2.5 ms after reaction with H_2O_2 are shown in blue. Spectra recorded at the time corresponding to H_2O_2 depletion (6 s for wild-type and 1.6 s for W321F) are shown in red. Spectra recorded for the ferric enzyme following mixing with buffer alone are shown by dashed lines. All reactions were carried out as described for Fig. 2.2.

intensity above 520 nm, but absorption bands near 540 and 580 nm were not observed. Instead there was a shoulder near 650 nm (Fig. 2.4 D). These features are consistent with a Fe^{IV}=O[porphyrin]$^{\bullet+}$ (i.e., compound I) species [144].

2.3.4. wtKatG protein-based radicals upon reaction with H_2O_2 alone. EPR evaluation of *wt*KatG freeze-quenched 10 ms after mixing with H_2O_2 showed a complete loss of signals corresponding to the ferric state (Fig. 2.5 A) concomitant with formation of an intense doublet radical signal (Fig 2.5 B). This species was consistent with the so-called narrow doublet (Fig. 2.5 B) reported by others [182-184]. It showed a relatively high $P_{½}$ value (~0.006 mW) consistent with its close proximity to the heme yet mitigated by substantial delocalization of the radical over the phenol and indole rings of the MYW adduct. This signal has been connected with the catalase activity of KatG and has been assigned as the MYW covalent adduct cation radical [124, 127]. Thus, at the earliest reaction times when *wt*KatG shows its most rapid rates of H_2O_2 consumption, the dominant intermediate was a putative Fe^{III}-$O_2^{\bullet-}$[MYW]$^{\bullet+}$ state.

At the time corresponding to H_2O_2 depletion (6 s), the ferric state had yet to return (Fig. 2.5 A), but the doublet radical had been replaced by a singlet signal (Fig. 2.5 B). In contrast to the narrow doublet, this spectrum was very broad (~400 G), indicating an exchange-coupled interaction with the heme iron (Fig. 2.5 B). The large $P_{½}$ value (~ 0.012 mW at 4.5 K) from power saturation studies was consistent with this conclusion (Fig. 2.6). Furthermore, a similar radical species has been observed with KatG from *M. tuberculosis* and *Burkholderia pseudomallei* upon their reaction with peracetic acid. In both cases, this radical has been assigned to the proximal tryptophan (W321 and W330, respectively) [128, 130]. When the reaction was quenched 1 minute after mixing with H_2O_2, a signal correspon-

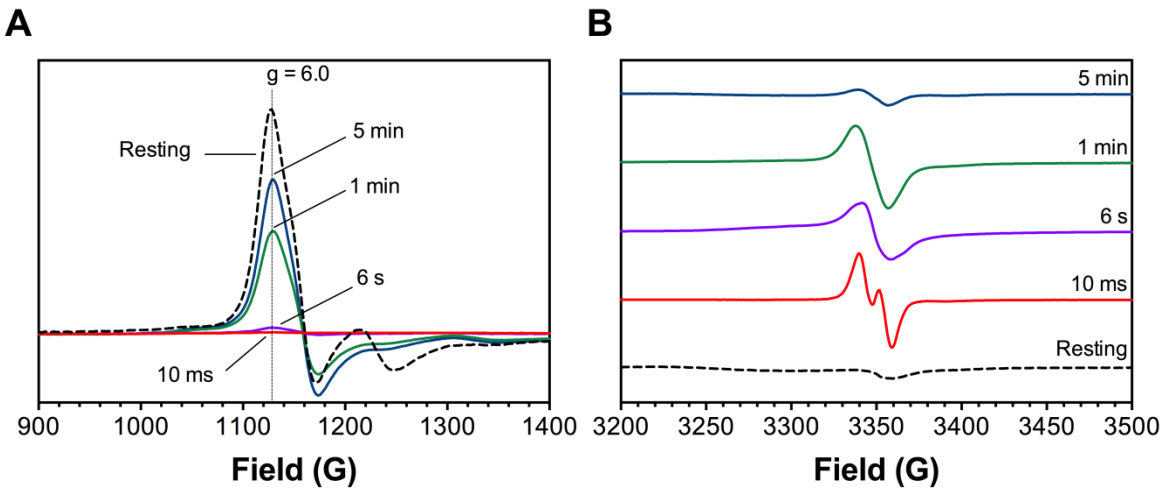

Figure 2.5. EPR spectra recorded for freeze-quenched samples from reaction of *wt*KatG with H_2O_2. The contribution of high-spin ferric species typical of the KatG resting state are shown in the g~6 region (center field = 1525 G) (A), and the g_z component of the resting state as well as protein-based radicals are shown in the g~2 region of the spectrum (center field 3355 G) (B). The molar proportions of enzyme to H_2O_2 used for stopped-flow experiments (1:667) were maintained for these experiments. Consequently, ferric KatG (150 μM after mixing) was reacted with H_2O_2 (100 mM after mixing) for the time indicated prior to freeze-quenching. Reactions were carried out at 25°C in 100 mM acetate, pH 5.0. All spectra were recorded at 4.5 K. Spectrometer settings were as described in *Experimental Procedures.*

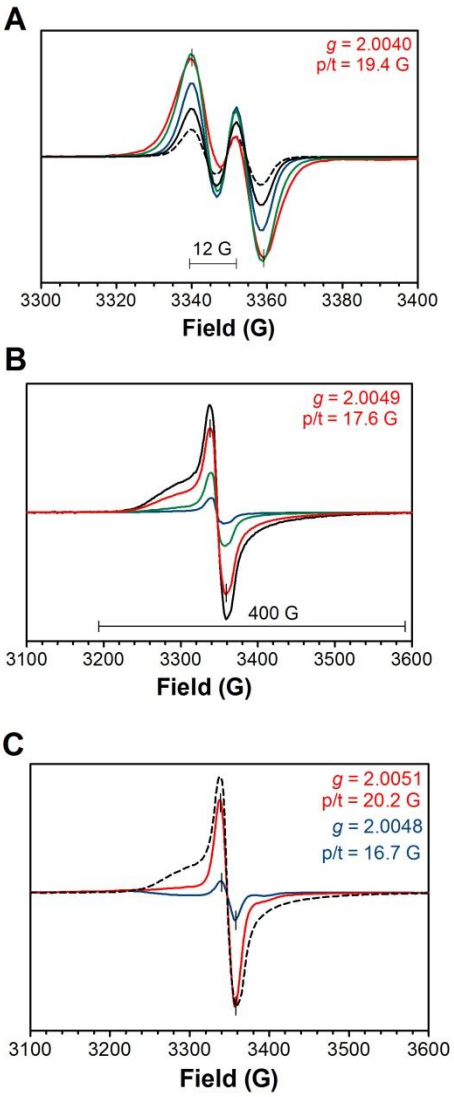

Figure 2.6. Evaluation of protein-based radicals detected during *wt*KatG reaction with H_2O_2. The doublet radical observed 10 ms after mixing with H_2O_2 (A) was recorded with microwave power of 1.0 mW (red line), 0.127 mW (green line), 7.9 μW (blue line), 1.0 μW (black line), and 0.3 μW (dashed line). The broad singlet radical observed 6 s after mixing with H_2O_2 (B) was recorded with microwave power of 3.9 mW (black line), 1.0 mW (red line), 0.063 mW (green line), and 3.9 μW (blue line). The broad singlet species observed at 6 s (dashed line) is compared to the narrow singlets observed 1 (red line) and 5 (blue line) minutes after mixing with H_2O_2 (C) with all three recorded using 1.0 mW microwave power. All spectra were recorded at 4.5 K with all other spectrometer settings as described in *Experimental Procedures*.

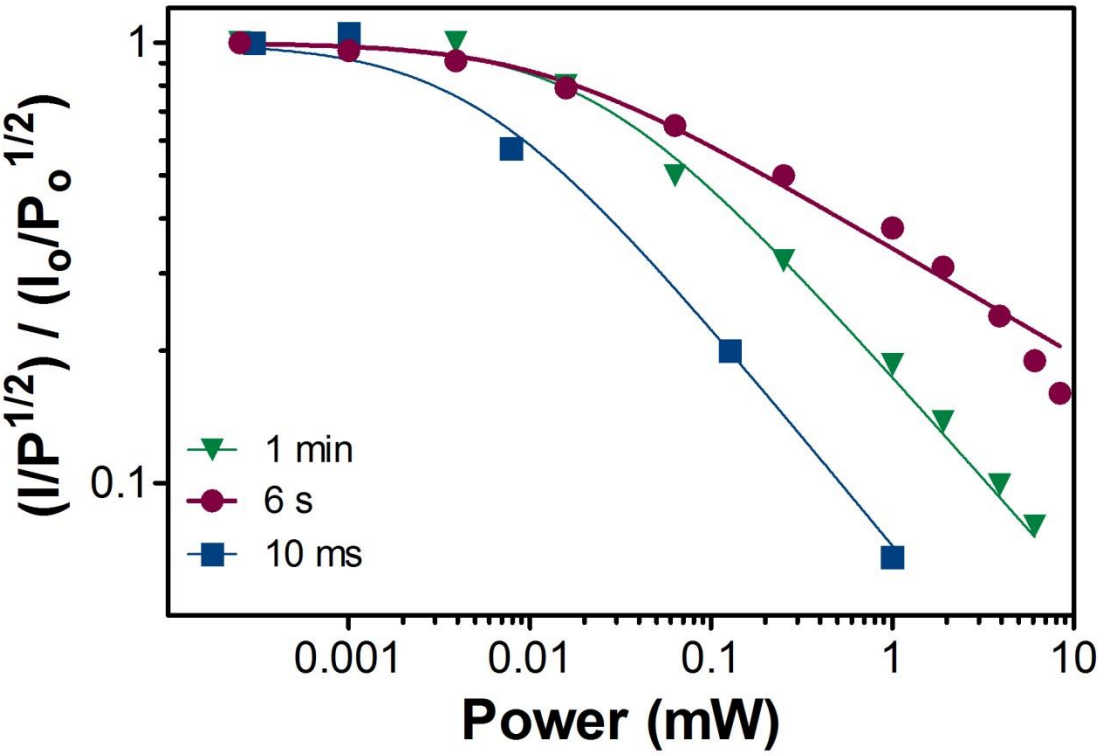

Figure 2.7. Effect of power on the radicals observed for *wt*KatG after its reactions with H_2O_2 at 10 ms (blue trace), 6 s (red-brown trace) and 1 min (green trace).

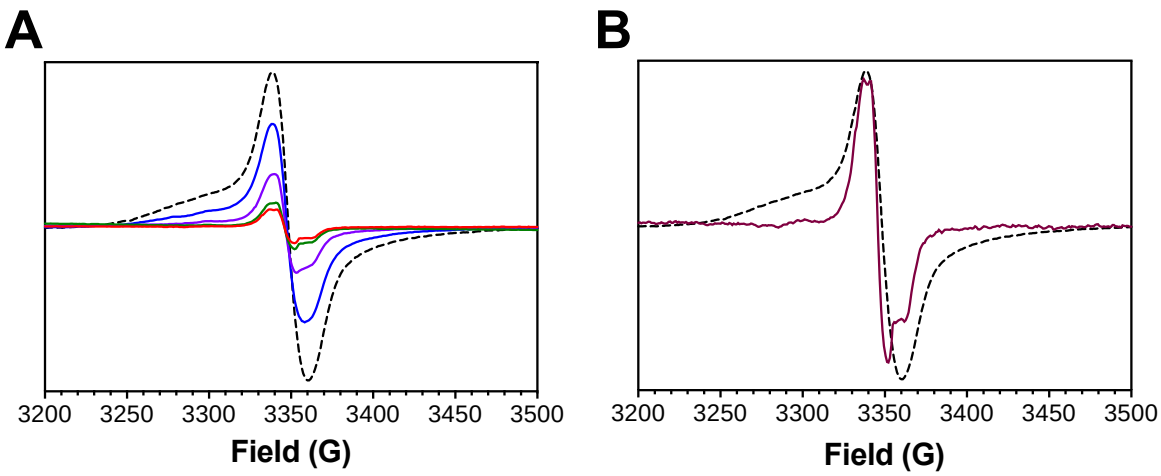

Figure 2.8. Effect of temperature on EPR spectra observed for *wt*KatG at the cessation of H_2O_2 consumption following reaction with H_2O_2 alone. Samples were prepared and evaluated as described for Fig. 2.5 and 2.6 B. Spectra were recorded at 4.5 K (dashed line), 8 K (blue line), 20 K (purple line), 50 K (green line), and 77 K (red-brown line) (A). Spectra recorded at 4.5 K (dashed line) and 77 K (red line) are also scaled for comparison (B).

ding to the ferric state (g ~ 6) was clearly present (though at diminished intensity compared to the resting state) along with a singlet protein-based radical (Fig. 2.5). Some broadening, though considerably less prominent than the species observed at 6 s, was evident (Fig. 2.6 C). These data are consistent with radical transfer wherein the radical observed at 6 s has been reduced at the expense of a more remote oxidizable amino acid residue. In samples quenched 5 minutes after reaction with H_2O_2, a greater contribution from the ferric state (Fig. 2.5 A) was observed along with a protein-based radical similar to that detected at 1 minute albeit with lower intensity (Figs. 2.5 B and 2.5 C). Thus, freeze-quench EPR data were in good agreement with our stopped-flow results where the re-emergence of the ferric state was only observed after the depletion of H_2O_2 (at 6 s post-mixing), and it occurred at a rate far below that which achieved the preceding catalatic consumption of >500 equivalents of H_2O_2. These data suggest that the primary inactive intermediate to accumulate contained a protein-based radical distinct from the $MYW^{\bullet+}$ narrow doublet. The exchange-coupling observed from this species is consistent with the proximal tryptophan (W321) as the site of protein radical accumulation with subsequent radical migration away from the active site.

2.3.5. W321F protein-based radicals upon reaction with H_2O_2 alone. To further examine the participation of W321 in accumulation of protein-based radical species, we carried out RFQ-EPR experiments with the W321F variant. Reaction of W321F KatG with the same concentration of H_2O_2 (Fig. 2.9) produced a nearly identical doublet radical spectrum at 10 ms. Similar to *wt*KatG, the narrow doublet was replaced by a protein-based singlet radical species at the time anticipated for the completion of H_2O_2 consumption (1.6 s) (Fig. 2.9 A). However, in contrast to the wild-type enzyme, this species was less intense

(Fig. 2.9 A), lacked any broadening associated with exchange coupling (Fig. 2.9 B), and though a radical was detected nearly a full minute later, its intensity was far less than that observed for the wild-type enzyme at the same time point (Fig. 2.9 C). Finally, where a weak radical signal was observed for wild-type even 5 minutes after H_2O_2 depletion, no radical was observed for W321F KatG at the same reaction time. Power saturation of the radical observed for W321F at 1.6 s was almost superimposable with that observed for wild-type KatG at 1 min (Fig. 2.10).

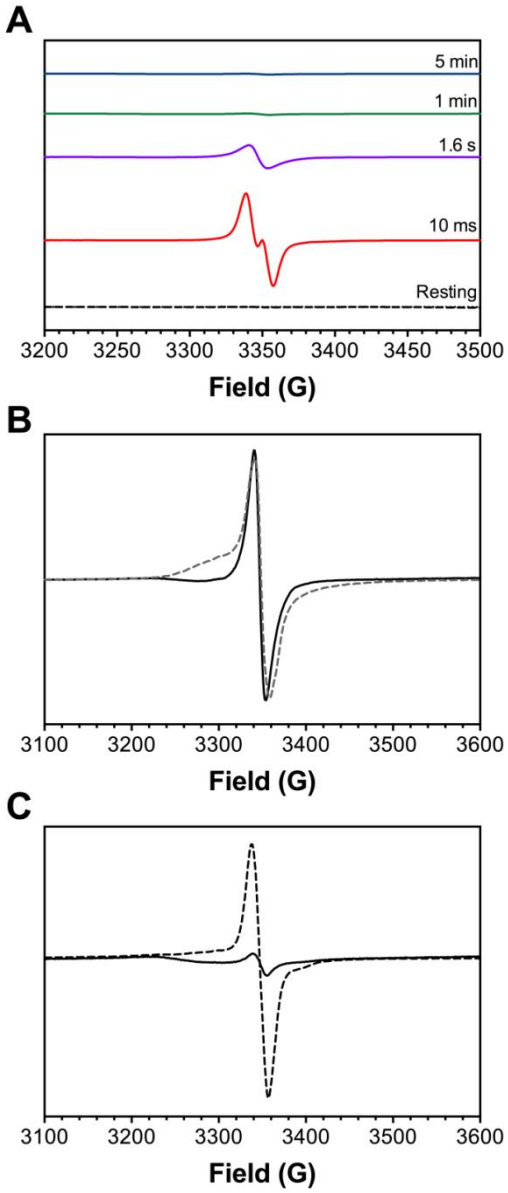

Figure 2.9. EPR spectra recorded for freeze-quenched samples from reaction of W321F KatG with H_2O_2. The contribution of protein-based radicals in the g~2 region of the spectrum for samples quenched after mixing with H_2O_2 at the times indicated are shown (A). The radical observed for W321F (solid line) at the time of H_2O_2 depletion (1.6 s) is compared to that recorded for wild-type KatG (dashed line) at the analogous time (6 s) (B). Likewise, the radical observed for W321F (solid line) and wild-type (dashed line) 1 minute after mixing with H_2O_2 are compared (C). Reaction conditions and spectrometer settings are the same as those described for Figure 2.5.

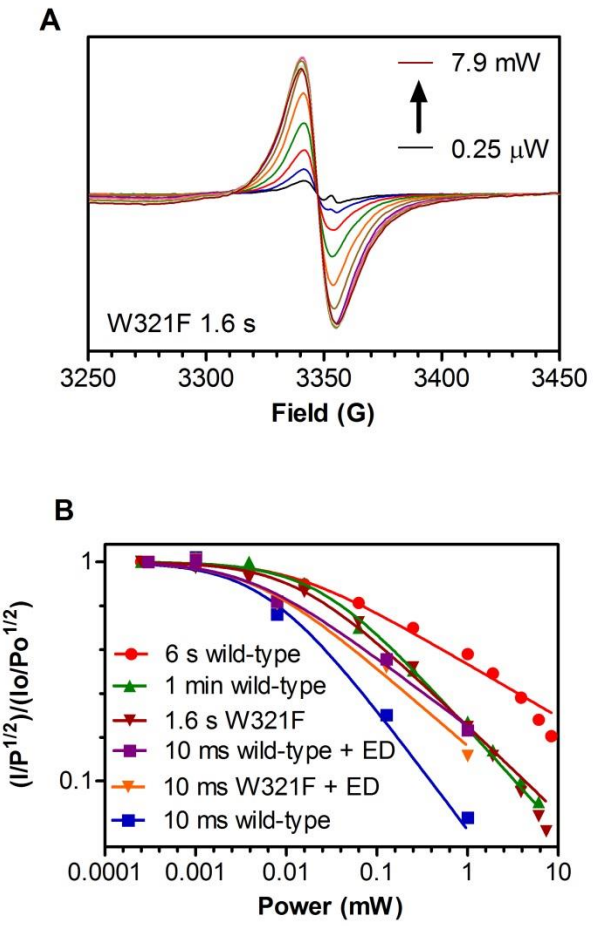

Figure 2.10. Effect of power on the radicals observed for W321F KatG after reaction with H_2O_2 at 1.6 s (A) and power saturation for radical observed for W321F with H_2O_2 alone at 1.6 s (dark red), ABTS/Asc included; 10 ms (orange trace), *wt*KatG after its reactions with H_2O_2 at 10 ms (blue trace), 6 s (red trace) and 1 min (green trace) and with ABTS/Asc included; 10 ms (purple trace).

2.3.6. Effect of PxEDs on wtKatG and W321F. Inclusion of the PxED, ABTS, stimulated the consumption of H_2O_2 and subsequent return of the ferric state for wild-type and W321F KatG (Fig. 2.11), but the effect was far more pronounced for the wild-type enzyme (Fig. 2.11 A). Consistent with these stopped-flow data, we observed that a range of PxEDs were able to stimulate wild-type catalatic O_2 production to a greater extent than for the W321F variant (Fig. 2.12).

We have proposed that PxEDs enhance catalase activity by preventing the accumulation of catalase-inactive intermediates. KatG's narrow active site access channel is purported to prevent access of PxEDs like ABTS to the heme edge for oxidation. This would imply that PxED oxidation only occurs to the extent that there is off-catalase electron transfer. In other words, PxED oxidation would be a manifestation of conversion of catalase-inactive states to active enzyme. Accordingly, evaluation of the ratios of ABTS oxidation to the concentration of H_2O_2 consumed would be a reflection of the need for inactive intermediate restoration. For both wild-type and W321F KatG, these ratios were low (Fig. 2.13), indicating that off-mechanism electron transfer is a relatively rare event (< 1 in every 60 catalase turnovers). However, for W321F the ratio (<0.003) indicates such an event occurs no more than once every 170 turnovers (Fig. 2.13). In order to examine the effects of PxEDs on the intermediates formed for wild-type and W321F KatG, similar RFQ EPR experiments were performed as those presented earlier.

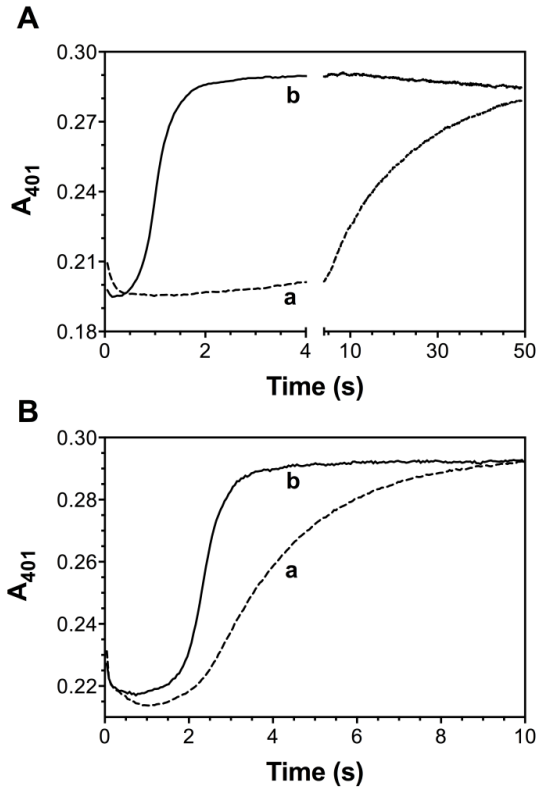

Figure 2.11. Effect of ABTS on the return of the KatG ferric state following H_2O_2 consumption. Wild-type (A) and W321F KatG (B) were reacted with 2.0 mM H_2O_2 in the absence (a) and presence (b) of 0.1 mM ABTS/0.1 mM ascorbate by stopped-flow at 401 nm to monitor the return of the ferric state following H_2O_2 depletion. The final concentration of enzyme in each reaction was 3 μM. All reactions were carried out in 50 mM acetate buffer, pH 5.0, at 4 °C.

With PxED (ABTS/ascorbate) included in the reaction mixture, wild-type and W321F KatG both show the same narrow doublet 10 ms after mixing with H_2O_2. Spectra recorded for samples quenched at the time anticipated for H_2O_2 depletion or any time thereafter showed minimal, if any, contribution from protein-based radicals for either wild-type or W321F KatG (Fig. 2.14).

A comparison of the narrow doublet obtained in the presence and absence of PxED from wild-type and W321F KatG, showed very little difference among all four samples (Fig. 2.15 A and 2.15 B). The narrow doublet was the predominant feature at 10 ms in all four reactions. Importantly, inclusion of a PxED with either protein did not interfere with the accumulation of the narrow doublet. Indeed, if anything, inclusion of the PxED increased its intensity. These observations are consistent with the putative role of the $[MYW]^{\bullet+}$ in the catalatic mechanism of KatG and the stimulatory effect of PxEDs on KatG catalatic activity. In contrast, W321 substitution and the inclusion of PxED both have a substantial influence on the radical species observed at the conclusion of H_2O_2 consumption (i.e., radicals that accumulate over the course of hundreds of turnovers) (Figs. 2.9 & 2.14 A). The broad, exchange-coupled radical observed with wild-type and its conspicuous replacement by a much narrower signal in W321F KatG suggest that W321 is a prominent site of oxidation.

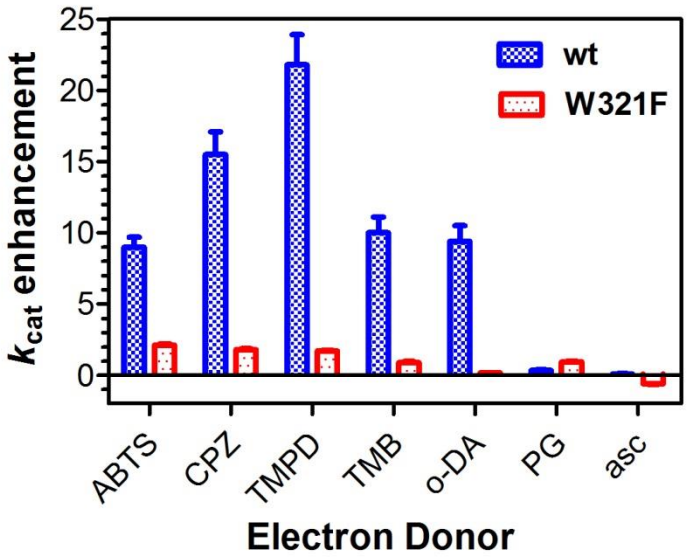

Figure 2.12. Effect of PxEDs on catalase apparent k_{cat} for wild-type and W321F *Mt*KatG. All activity measurements were on the basis of O_2 production as described in *Experimental Procedures* and were carried out in 50 mM acetate buffer, pH 5.0, at 23 °C. All electron donors were present at 0.1 mM. 2,2'-azino-bis[3-ethylbenzthiazoline-6-sulfonate], chlorpromazine, *N,N,N'N'*-tetramethyl-*p*-phenylenediamine, 3,3',5,5'-tetramethylbenzidine, *o*-dianisidine, pyrogallol, and ascorbate are indicated by ABTS, CPZ, TMPD, TMB, *o*-DA, PG, and asc, respectively. The individual k_{cat} determinations used for are presented in Table 2.3.

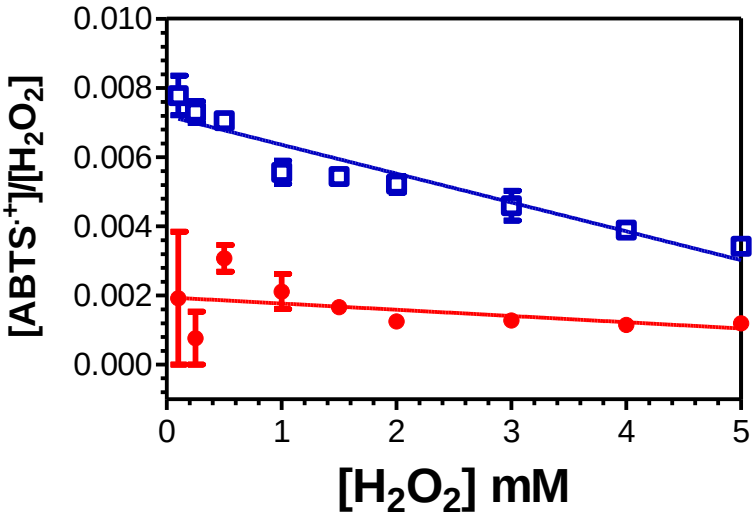

Figure 2.13. Yield of $ABTS^{\bullet+}$ generated to H_2O_2 consumed for wild-type (blue) and W321F (red) *Mt*KatG.

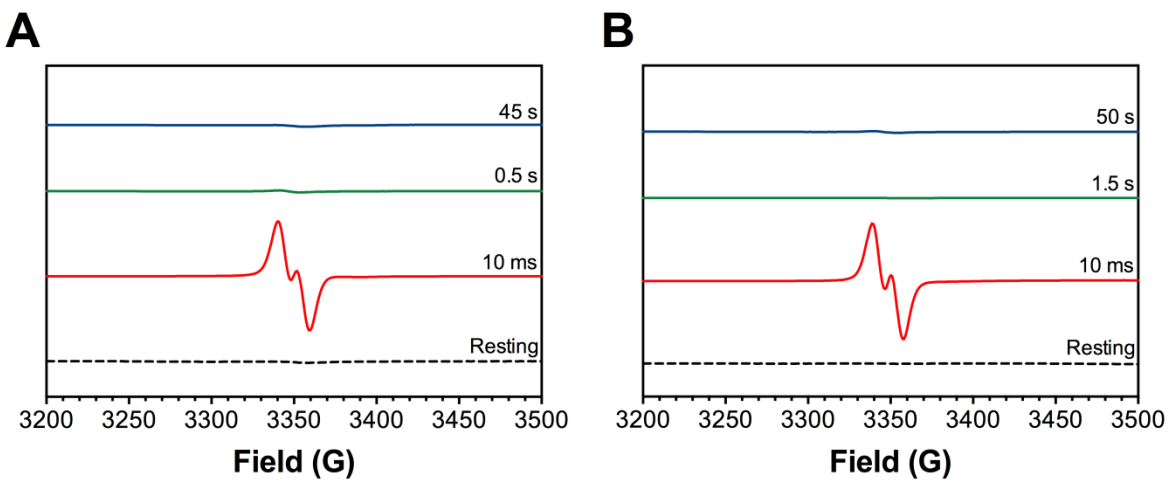

Figure 2.14. EPR spectra from freeze-quenched samples for wild-type (A) and W321F (B) upon reaction with H_2O_2 in the presence of PxED. Reactions were carried out as described in Figure 2.5, except that ABTS (1.0 mM final concentration) and ascorbate (2.0 mM final concentration) were also included. The reactions were quenched at the times indicated for each protein. All spectrometer settings were as described for Figure 2.5.

That a protein-based radical forms even with non-oxidizable Phe in place of the proximal Trp indicates that other residues can also be oxidized. The absence of exchange coupling with these radicals suggests they are further from the heme iron. Inclusion of a PxED prevents the accumulation of non-MYW protein-based radicals generated during turnover of either wild-type or W321F KatG, presumably by acting as a sacrificial reductant (Fig. 2.17).

2.3.7. Off-pathway electron transfer through W321. A model accounting for these data is presented in Fig. 2.17. KatG progressively loses catalase activity over time. Concomitantly, an exchange-coupled radical consistent with $W321^{\bullet+}$ accumulates and is the dominant species observed at the time H_2O_2 consumption ceases. Spectra recorded at 77 K indicate that more remote protein-based radicals are present as well (Fig. 2.8), and these are observed more clearly at 4.5 K as the ferric state slowly returns (Fig. 2.5 A and 2.6 C). These data suggest radical transfer from W321 in the active site to more distant oxidizable residues.

Strikingly, inclusion of a PxED does not diminish (if anything, it enhances) the $MYW^{\bullet+}$ narrow doublet associated with catalatic turnover. Simultaneously, PxEDs essentially abrogate the accumulation of all other protein radical species. This indicates that the PxED does not directly access the active site, rather W321 is the first step in a radical transfer pathway that delivers oxidizing equivalents to an exterior site where electron transfer from the PxED can occur. This is consistent with KatG structures that invariably show the active site access channel is too narrow for molecules like ABTS to navigate. It is also consistent with conclusions drawn from EPR spectra of KatG reacted with peracetic acid [128, 130].

The identity of the heme state to accumulate during inactivation is more difficult to discern, owing to the inherent ambiguity of heme absorption spectra [126]. Nevertheless, these spectra show the clear markings of a compound III-like (i.e., Fe^{III}-$O_2^{\bullet-}$) state during the

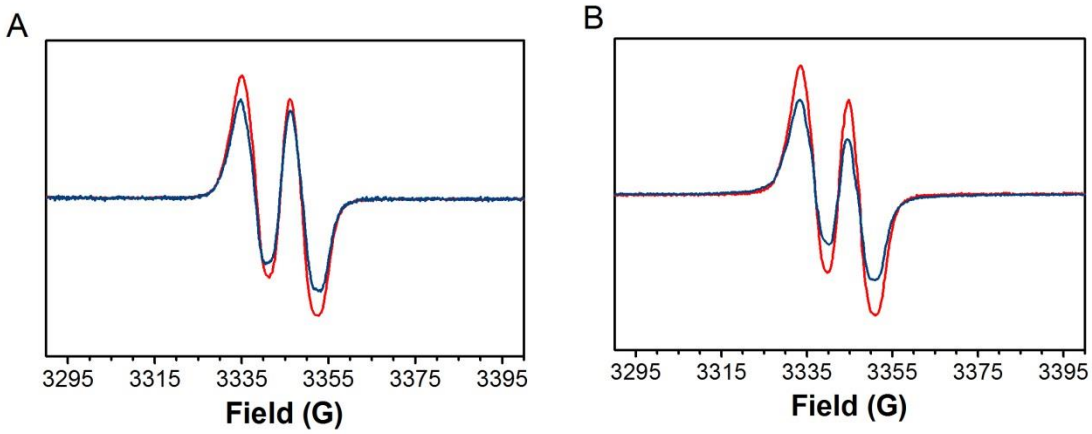

Figure 2.15. Comparison of EPR spectra for protein-based radicals 10 ms after mixing with H_2O_2 (A and B). Spectra were recorded for wild-type KatG (A) and the W321F variant (B) in the absence (blue lines) and presence of ABTS/ascorbate (red lines). Reaction conditions were as described for Figure 2.5. Spectra shown in panels A and B (10 ms after mixing with H_2O_2) were recorded at 77 K.

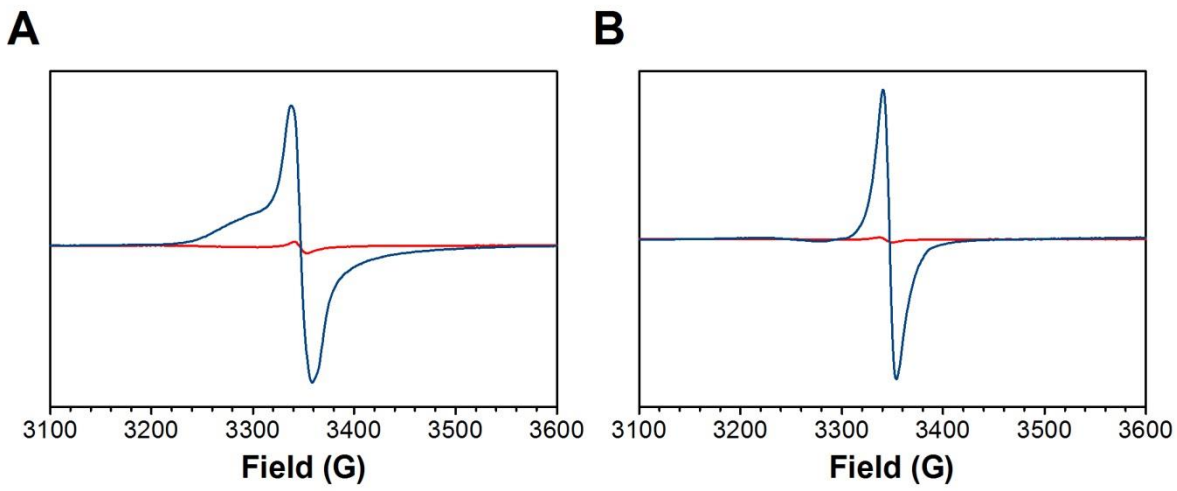

Figure 2.16. Comparison of EPR spectra for protein-based radicals at H_2O_2 depletion (A and B). Spectra were recorded for wild-type KatG (A) and the W321F variant (B) in the absence (blue lines) and presence of ABTS/ascorbate (red lines). Reaction conditions were as described for Figure 2.5. When included, the concentrations of ABTS and ascorbate were 1.0 and 2.0 mM, respectively. Spectra were recorded at 4.5 K.

enzyme's most active catalatic turnover. That is, during the earliest stages of reaction with H_2O_2. Over time, this spectrum is progressively obscured by the apparent accumulation of other species. Bands near 540 and 580 indicate the presence of Fe^{III}-$O_2^{\bullet-}$ heme. However, contributions from a compound II-like Fe^{IV}=O cannot be ruled out. In keeping with the long known greater reactivity of PxEDs toward Fe^{IV}=O species relative to Fe^{III}-$O_2^{\bullet-}$ states, we propose PxEDs short circuit formation of an inactive Fe^{III}-$O_2^{\bullet-}$[non-MYW]$^{\bullet}$ (compound[s] III^{i} in Fig. 2.17) and reduce Fe^{IV}=O[non-MYW]$^{\bullet}$ (compound[s] I^{i} in Fig. 2.17) back to the ferric state to rejoin active catalatic O_2 production. With a protein-based radical centered at a site other than the MYW cofactor, the Fe^{III}-$O_2^{\bullet-}$, once formed, would be expected to display the same abysmal rate of catalatic O_2 production observed for the Fe^{III}-$O_2^{\bullet-}$ state in typical peroxidases [169]. All our data point toward the proximal tryptophan (W321) as the primary starting point for off-catalase electron transfer. Though substantially less than wild-type, PxEDs do show a modest stimulatory effect on W321F catalase activity, and remote protein-based radicals are detected in this protein at the cessation of H_2O_2 consumption. It is possible that in the absence of W321, more remote W or Y residues are still oxidized albeit at a slower rate/lesser extent without the intervening W321 to facilitate electron transfer. Alternatively, other off-catalase radical transfers may be involved. For example, the MYW$^{\bullet+}$ of compound 1* may be reduced prematurely by more remote protein-based electron donors. These make a much smaller contribution to the catalase inactivation; however, PxEDs are able to prevent the accumulation of these species in any case.

In light of these data and conclusions drawn from them, it is reasonable to ask: Why does KatG have a proximal tryptophan rather than a phenylalanine? More distant plant peroxidase-like superfamily members like HRP and manganese peroxidase have a Phe in the analogous position [185, 186], but the proximal Trp is invariant across all KatGs. In C*c*P, the redox cycling of this residue is an integral part of the mechanism of cytochrome *c* oxidation. Interestingly, the anticipated distance between the acceptor and donor heme centers of the reaction necessitates through-protein radical transfer, the first step of which is proximal tryptophan oxidation by Fe^{IV}=O[porphyrin]$^{\bullet+}$ to form the well-known CcP compound ES (i.e., Fe^{IV}=O[W_{191}]$^{\bullet+}$) [131, 132]. KatG does not oxidize ferrous cytochrome *c* [137]. The W321F substitution showed no deleterious effect on catalase activity at neutral pH, and its absence *enhanced* catalase activity at acidic pH.

So, if at best this residue has no impact on the dominant activity of the enzyme, and at worst detracts from it, why is it still there? We can only speculate. However, it is noteworthy that the proximal tryptophan facilitates the essentially simultaneous and mutually synergistic operation of catalase *and* peroxidase functions. Our data show that PxEDs reduce non-MYW radicals, leaving the MYW$^{\bullet+}$ required for catalatic turnover essentially untouched. This explains why the traditional antagonistic model of catalase and peroxidase interplay does not hold, and why PxEDs stimulate rather than inhibit catalase activity. The potential implications of a synergistic rather than the traditional antagonistic model are potentially far-reaching. For example, by antagonism PxEDs must necessarily inhibit catalase activity. Further, control of activity is based largely on external factors: [H_2O_2], [PxED], etc. In contrast, in a model of mutual synergism, *control of activity distribution rests with the enzyme itself*. The degree to which off-catalase electron transfer is permitted is the degree to

which radical transfer produces PxED oxidation. From its exterior location and *by* its own oxidation, the PxED ensures that catalase-active states are restored, simultaneously optimizing catalatic H_2O_2 degradation. In such a model, the appropriate PxED for KatG need only be present to fulfill a stimulatory role, and by this mechanism peroxidatic activity would never interfere with catalatic turnover.

The advantage, then, would be in leaving open the possibility for PxED oxidation, and this would imply that such a process served an essential need of the organism. To date, the identity of a physiological electron donor for KatG is unknown let alone what essential function its oxidation may serve. However, the distinct behaviors resulting from a synergistic model (e.g., stimulation not inhibition of catalase activity) may provide insight into the properties to anticipate for KatG's physiological PxED. These matters are intimately connected with the effective application of KatG for H_2O_2 detoxification by the organisms that carry it.

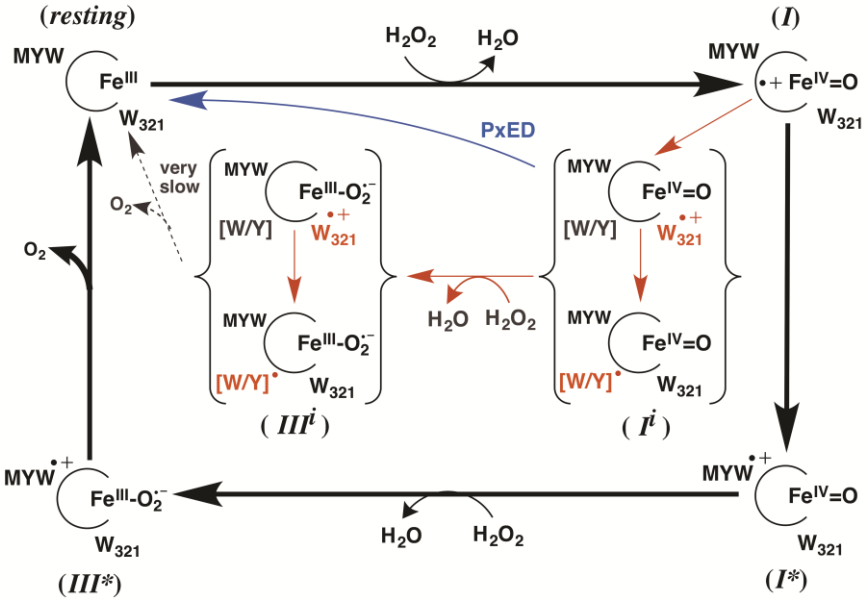

Figure 2.17. Scheme representing the proposed mechanism for inactivation of KatG catalase activity and its prevention by a peroxidatic electron donor (PxED). The KatG *catalase* cycle proceeds by way of the ferric or resting enzyme, compound I (*I*), compound I* (*I**), and compound III* (*III**). Off-pathway reduction of the porphyrin π radical of compound I by the proximal tryptophan (W_{321}) produces the catalase-inactive intermediate compound I^i (I^i). Subsequent reaction of I^i with H_2O_2 is expected to produce a catalase-inactive compound III-like intermediate (III^i) where the protein based radical is unable to facilitate oxidation and O_2 release from the Fe^{III}-$O_2^{\bullet-}$ complex. Species derived from radical migration from W_{321} to oxidizable residues further from the active site (W/Y) could occur with either Fe^{IV}=O or Fe^{III}-$O_2^{\bullet-}$ intermediates. The conversion of I^i to the active ferric state by a peroxidatic electron donor (PxED) is proposed. The Met-Tyr-Trp covalent adduct and its corresponding radical are represented by MYW and $MYW^{\bullet+}$, respectively. The proximal tryptophan and its corresponding radical are represented by W_{321} and $W_{321}^{\bullet+}$, respectively. An unspecified KatG oxidizable amino acid and its corresponding radical are represented by [W/Y] and $[W/Y]^{\bullet}$, respectively.

Chapter Three: Arginine Switch control of KatG intramolecular electron transfer: Activity, Inactivation, and Restoration

Abstract.

PxEDs have the ability to increase the efficiency of KatG as a catalase by over an order of magnitude. Indeed, the stimulatory effect of PxEDs is pH-dependent such that it mimics the conformational shift of an arginine residue (R418) away from the KatG-unique Met255-Tyr229-W107 covalent adduct. To understand the role of R418 in the control of intramolecular electron transfers in KatG active site, we disrupted the dynamic switch by mutagenesis. The R418A variant showed a diminished catalase activity (k_{cat}/K_M = 7.9 × 10^3 $M^{-1}s^{-1}$) at pH optimum for catalase activity (i.e., pH ~ 7.0). However, lowering the pH to 5.0, the catalase activity for R418A increased by nearly two orders of magnitude (k_{cat}/K_M = 5.2 × 10^5 $M^{-1}s^{-1}$). PxEDs were able to stimulate R418A KatG to an extent similar to wild-type KatG and R418K KatG. That the R418A KatG variant also produced a narrow-doublet radical at 10 ms of nearly equal intensity as that observed for wild-type KatG suggests that R418A KatG utilizes the MYW adduct radical for its activity. At the time where R418A KatG ceased consumption of H_2O_2, the narrow doublet radical was replaced by an exchange-coupled signal similar to the proximal tryptophanyl radical observed for wild-type KatG. The inclusion of a peroxidatic electron donor (PxED) increased the intensity of the MYW narrow doublet radical by two fold but nearly completely eliminated the exchange-coupled radical detected at H_2O_2 depletion. Thus PxEDs appear to prevent accumulation of non-MYW radicals, returning catalase-inactive intermediates to active turnover, thus producing higher steady state concentrations of $MYW^{\bullet+}$-bearing states. Further, we show that R418A KatG

catalase turnover produces far more $ABTS^{\bullet+}$ than wild-type KatG at all H_2O_2 concentrations. This also implies that R418A required an extensive participation of PxEDs for its rescue mechanism. Taken together, these data demonstrate that R418 acts as a modulator of intramolecular electron transfer events in KatG catalysis.

3.1. Introduction

Catalase-peroxidases (KatGs) are hemoproteins found in a wide range of prokaryotes and lower eukaryotes [140, 187]. They have been implicated as virulence factors for a number of pathogenic organisms including *Magnaporthe grisea* and *Mycobacterium tuberculosis* [93, 103, 188]. Indeed, KatG from the latter has also garnered interest because it is the only catalase-active enzyme carried by *M. tuberculosis*, and it is required to activate the isoniazid prodrug to its antibiotic form [89, 94]. Mutations affecting the *katG* gene appear in a large majority of isoniazid resistant *M. tuberculosis* strains. However, neither the mechanism of isoniazid activation nor the role of KatG mutations in imparting resistance have been fully elucidated [100, 159, 160].

KatG is able to degrade H_2O_2 by peroxidatic ($H_2O_2 + 2\ RH \rightarrow 2\ H_2O + 2\ R^{\bullet}$) and catalatic ($2\ H_2O_2 \rightarrow 2\ H_2O + O_2$) mechanisms [100, 101, 137, 162]. KatG is the sole catalase-active member of its peroxidase-catalase (Px-Ct) superfamily. As a member of this superfamily, KatG has an overall active site structure of a typical peroxidase (e.g., C*c*P), not a typical catalase (Fig. 3.1). As such, it should not be surprising to find that KatG uses a novel catalase mechanism, one that hearkens back to its peroxidatic roots. Indeed, reaction of KatG with H_2O_2 alone produces a visible absorption spectrum consistent with a Fe^{III}-$O_2^{\bullet-}$ heme intermediate. This is rarely if ever observed in typical (i.e., monofunctional) catalases, but is very common among peroxidases.

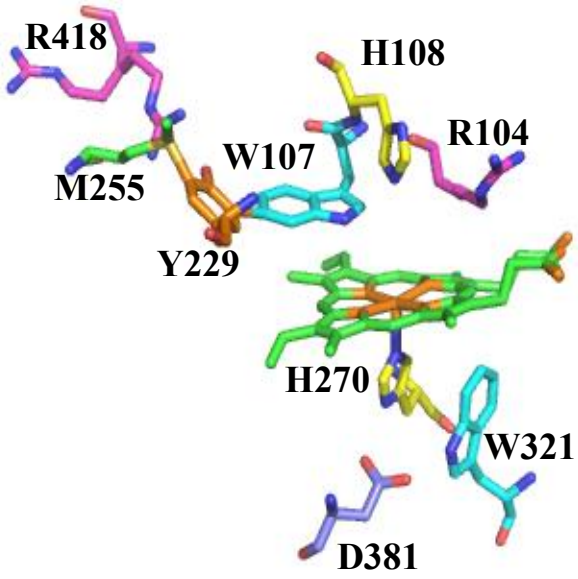

Figure 3.1. Active site structure of *M. tuberculosis* KatG active site showing the two conformations of R418. Amino acid oxygen and nitrogen elements are colored in red and blue, respectively. Structural image was produced using PDB accession domain 2CCA [108].

What distinguishes KatG from other peroxidases is that the robust O_2 production is purported to emerge from the KatG Fe^{III}-$O_2^{\bullet-}$ state, but the same intermediate in other peroxidases is inactive [100, 169]. What then converts an otherwise inactive intermediate into an essential step in catalase turnover? KatG has a unique post-translationally generated protein-derived cofactor between the side chains of M255, Y229, and active site W107 (*Mt*KatG numbering) (Fig. 3.1) [104, 105, 107, 163, 165]. The covalent adduct has been demonstrated to be essential for catalase activity. For example, KatG variants targeting the covalent adduct have no catalase activity and peroxidase activity equal to or greater than wild-type KatG [113, 114, 139, 166]. The MYW covalent adduct can be oxidized to a free radical ($MYW^{\bullet+}$) intermediate in the presence of H_2O_2. This radical has been identified as a unique narrow-doublet species by freeze-quench EPR [124, 127, 142, 187]. It is only observed during active *catalatic* turnover, and it persists until H_2O_2 is depleted from a reaction. KatG variants that disrupt the covalent adduct are unable to produce the unique narrow doublet radical.

For the KatG catalase cycle, the ferric enzyme reacts with a first equivalent of H_2O_2 to form an oxo ferryl porphyrin π cation radical (i.e., compound I) intermediate. This highly unstable species undergoes an intramolecular electron transfer where the porphyrin radical migrates to the MYW adduct forming a compound I* species (i.e., Fe^{IV}=O[$MYW^{\bullet+}$]) [51, 101, 144]. Previous studies have revealed that the tyrosine of the MYW covalent adduct should be in its deprotonated state for this conversion because this is the only stable state for the $MYW^{\bullet+}$ while the arginine switch occupies its ‘out’ position [136, 171]. Calculations on KatG compound I also suggest that the spin density of two-electron oxidized KatG (i.e., compound I, compound I*, etc.) is distributed between the covalent adduct and the proximal

Trp, -and this distribution is pH-dependent. At conditions when the MYW adduct is protonated and the arginine switch occupies its 'out' position (i.e., pH < 6.5), the $MYW^{\bullet+}$ dominates while at conditions when the MYW adduct is deprotonated and the switch is predominantly in its 'in' position (i.e., pH > 6.5), the proximal tryptophanyl (i.e., $W321^{\bullet+}$) radical is the dominant intermediate [171]. For the second step, compound I* reacts with a second equivalent of H_2O_2 to form a (Fe^{III}-$O_2^{\bullet-}$[MYW]$^{\bullet+}$) intermediate termed compound III*. Another intramolecular electron transfer is proposed to occur from the Fe^{III}-$O_2^{\bullet-}$ intermediate to neutralize the $MYW^{\bullet+}$, thereby releasing O_2 and return the ferric enzyme along with the closed shell MYW adduct [100, 124, 125, 127, 136].

The continuing elucidation of the reaction mechanism of KatG has not been without controversy. First, this represents the only observation of a Fe^{III}-$O_2^{\bullet-}$ state as an active intermediate in catalase turnover, and it has only been detected by UV-visible spectroscopy, a notoriously ambiguous spectroscopic technique. With KatG from *Burkholderia pseudomallei*, an apparent peroxoindole derivative of the MYW adduct has been detected by x-ray crystallography upon reaction of the enzyme with H_2O_2 [136]. Along with computational evaluation of MYW adduct radical deprotonation and derivatization with O_2, a mechanism for conversion of compound I* to compound III* has been proposed [136]. Further, reaction of KatG with an alternative peroxide, peracetic acid (PAA), produces an entirely different set of KatG intermediates [114, 120, 126, 134]. An oxoferryl state has been detected by UV-vis and X-ray crystallography [114, 120, 126, 134]. The KatG narrow doublet associated with the MYW radical is not observed, but instead, a series of porphyrin, tryptophanyl- and tyrosyl- radicals are detected. In some cases, the porphyrin radical of a canonical compound I is detected, but the most prominent species is a radical centered on

the proximal tryptophan. A combination of mutagenesis, expression of deutero-Trp- and/or deutero-Tyr-labeled KatG along with evaluation with multifrequency EPR has produced a radical transfer sequence of

Fe^{IV}=O[porphyrin] $^{\bullet+}$ → Fe^{IV}=O[proximal Trp] $^{\bullet+}$ → Fe^{IV}=O [remote W/Y]$^{\bullet}$ [129, 131, 140, 189]. This sequence bears a strong resemblance to the reactions of C*c*P where the proximal tryptophan (W191) is known to be oxidized to a radical state, and this is integral to the peroxidase activity of the enzyme [131, 132]. Our research draws a connection between these two disparate sets of results.

The catalase and peroxidase mechanisms of KatG were initially thought to be mutually exclusive. However, we recently observed a mutual synergism between both activities [138]. We have also demonstrated that one possible mechanism for peroxidatic electron donor stimulation of KatG catalase activity is by rescuing inactive intermediates which result from off-pathway protein oxidation events and the proximal tryptophan is a primary conduit for such events [187]. Our results suggest that off-pathway electron transfer and the corresponding need for PxED-based restoration of inactive states increases as pH decreases from 7 toward 5. This pH change mirrors the conformational shift in KatG arginine switch (i.e., R418) and the propensity of the proximal tryptophan oxidation [171].

The so-called Arg switch modulates KatG catalase activity despite its location about 20 Å away from the active site. This residue's conformational state is pH-dependent [133, 134]. Crystal structures available for *Bp*KatG reveal that at pH 4.5, the guanidinium moiety of the switch is directed away from the MYW covalent adduct towards two other arginine residues ('R' or 'out' conformation). At a pH of 8.5, the side chain of the arginine is pointed to and interacts with the phenolic moiety of the MYW adduct through a salt bridge

association ('Y' or 'in' conformation). At pH ~ 6.5, near the observed optimum for catalase activity, the switch equally populates both conformations. It has been suggested that the 'R' conformation favors MYW oxidation while the 'Y' conformation favors $MYW^{\bullet+}$ reduction [133, 134].

The R418 residue was recently suggested to play a vital role in the release of O_2 in KatG catalase activity [135, 136, 142]. The importance of R418 in the KatG catalase mechanism is demonstrated by a substantial loss in catalase activity when it is changed to any other residue except lysine [133, 134]. The R418L variant readily produces the $MYW^{\bullet+}$ and Fe^{III}-$O_2^{\bullet-}$ species throughout the time corresponding to H_2O_2 consumption [142]. Its low catalatic turnover was attributed to the inability of the steady state intermediate to release O_2 for the enzyme to return to the ferric state. Radical transfer away from the active site is also apparent over the course of reaction with H_2O_2 is also apparent as observed by increased oxidative protein oligomerization [142].

The pH-dependence of the stimulatory effect of PxEDs, the pH-dependence of the invariant arginine switch and the postulated ability of the arginine switch to influence the electronic structure of the MYW adduct and proximal tryptophan, taken together, point toward the arginine switch (R418 by *M*tKatG numbering) as a modulator of intramolecular electron transfers within the KatG active site. Therefore, we investigated the participation of the arginine switch in active site intramolecular electron transfer by preparing the switch variants R418A, and R418K KatG. Our data indicate that the absence of the arginine switche either by pH or mutagenesis increases radical transfer away from KatG active site and that PxEDs resolve the problem by reducing catalase-inactive intermediates, returning them to active catalatic turnover, thereby stimulating KatG catalase activity.

3.2. Materials and Methods

3.2.1. Reagents. Chlorpromazine (CPZ), pyrogallol, 3,3',5,5'-tetramethylbenzidine dihydrochloride hydrate (TMB), N,N,N',N'-tetramethyl-*p*-phenylenediamine dihydrochloride (TMPD), 3,3'-dimethoxybenzidine (*o*-dianisidine), 2,2'-azino-bis (3-ethylbenzthiazoline-6-sulfonic acid) (ABTS), L-ascorbic acid, hemin, ampicillin, hydrogen peroxide (30%), imidazole, calcium chloride hydrate and sodium dithionite were purchased from Sigma-Aldrich (St. Louis, MO). Tetracycline hydrochloride, mono and dibasic sodium phosphate, sodium chloride, sodium acetate trihydrate, potassium chloride, magnesium chloride and magnesium sulfate were purchased from Fisher (Pittsburg, PA). P*fu* polymerase, Herculase polymerase, T4 DNA ligase, and all *E. coli* (XL-1 Blue) were gotten from Agilent (La Jolla, CA). Phusion High Fidelity PCR Master Mix with GC Buffer and all restriction enzymes were purchased from New England Biolabs (Beverly, MA). All oligonucleotide primers for site-directed mutagenesis as well as sequencing were purchased from Invitrogen (Carlsbad, CA). Benzonase nuclease, Bugbuster, nickel-nitrilotriacetic acid resin were bought from Novagen (Madison, WI). Isopropyl-β-D-thiogalactopyranoside was purchased from Gold Biotechnology (St. Louis, MO). Buffer exchange chromatography columns (10DG) and Macro-Prep High Q resin were acquired from BioRad (Hercules, CA). Centrifugal filters (50 kD cutoff) were obtained from Millipore (Billerica, MA). All buffers and media were prepared using water purified through a Barnstead EASY pure II UV ultrapure water system (18.2 MΩ/cm resistivity).

3.2.2. Mutagenesis. Site-directed mutagenesis was also carried out by applying the 'Round-the-Horn' approach as was described [174]. The forward primers designed for R418A and R418K KatG construction were 5'-

C***GCA***GATATGGGTCCCGTTGCGAGATACCTTG-3', and 5'-C***AAG***GATATGGGTCCCGTTGCGAGATACCTTGG-3', respectively. The nucleotide substitutions designed to produce the mutation are highlighted in bold italics. This approach allowed us to use the same reverse primer to generate both mutants (5'-TGGATCAGCTTGTACCAGGCCTTGGCGAACTC-3'). All primers were modified to include 5'-phosphoryl groups, allowing for the blunt-end ligation of the PCR products. PCR for generation of the R418K mutant was done using Herculase polymerase in manufacturer supplied buffer. In contrast, the PCR for the R418A mutant was carried out using Phusion High-Fidelity polymerase in GC Buffer-containing Master-Mix and 3 % DMSO. All PCR products were then treated with D*pn* I to remove starting template and then ligated using T4 DNA ligase. Ligation products were used to transform *E. coli* (XL-Blue) by a standard heat-shock protocol [175]. The transformants were chosen on the basis of ampicillin-containing media and candidate plasmids were screened by P*sh*A I digestion as successful mutation would eliminate a P*sh*A I unique restriction site. Potential candidates were sequenced (Davis Sequencing, Davis CA) to verify that our intended mutations were successful and that no unintended mutations were present.

3.2.3. Protein expression and purification. *E. coli* C41(DE3) cells bearing the heme protein expression plasmid, pHPEX3, were transformed with pET-based expression constructs for R418K and R418A KatG, and transformants were selected on the basis of ampicillin and tetracyclin resistance [175]. Expression of both R418 variants was carried out as described elsewhere [138, 187]. As with wild-type KatG, the R418A and R418K variants were expressed in their soluble forms. Likewise, their purifications were done as demonstrated for wild-type KatG [138, 187]. The final purified R418K and R418A KatG

had optical ratios A_{408}/A_{281} (i.e., R_z values) of 0.61 and 0.57, respectively. The apparent kinetic parameters for both catalase and peroxidase activities were in good agreement with those reported previously for KatG from *B. pseudomallei* and *Synechocystis* PCC [133, 134].

3.2.4. UV-visible spectra and activity assays. Spectra for purified R418 variants were recorded as previously described [138, 187]. The molar absorptivity of R418K, and R418A KatG enzymes were determined using the pyridine hemichrome assay [176]. Their peroxidase activities were evaluated as previously described using ABTS as the PxED [138, 177, 187]. Catalase activity was determined by monitoring O_2 production over time using a Clark-type O_2-sensitive electrode (Hansatech, Pentney, Norfolk, England) as previously described [138, 187]. In some experiments, catalase activity was also measured spectrophotometrically by observing a decrease in H_2O_2 concentration over a period of 60 s at 240 nm (ε_{240} = 39.4 M^{-1} cm^{-1}) [178].

3.2.5. Analyses of steady-state kinetic data. One of three kinetic responses of KatG and its variants to substrate concentration is observed. If, as is often the case, a standard rectangular hyperbolic increase in rate with increasing substrate concentration is detected, the data are fit using a standard Michaelis-Menten, **Eqn. 3.1** to obtain the apparent kinetic parameters k_{cat}, K_M, and k_{cat}/K_M.

$$\frac{v_o}{[E]_T} = \frac{k_{cat}[S]}{K_M + [S]} \qquad \textbf{(3.1)}$$

In all situations where the terms are applied, k_{cat} is the asymptotic maximum rate divided by the concentration of holo-enzyme as estimated by heme concentration. The apparent K_M is not intended to mean anything more than the concentration of substrate necessary to produce

½ of the maximum rate, and k_{cat}/K_M is considered the catalytic efficiency. In some instances, substrate-dependent inhibition is apparent. To obtain an estimate of the kinetic parameters unobscured by the inhibitory effect of the substrate, the data are fit to **Eqn. 3.2**. The apparent K_I corresponds to a macroscopic apparent dissociation constant accounting for the inhibitory properties of the substrate.

$$\frac{v_o}{[E]_T} = \frac{k_{cat}[S]}{K_M + [S] + [S]^2/K_I} \qquad \textbf{(3.2)}$$

Finally, we have noted in previous studies that at low pH, (e.g., pH 5.0) wild-type KatG shows two distinct phases in its responses to H_2O_2 concentration [138]. One appears hyperbolic with a low apparent K_M for H_2O_2; the other is linear with H_2O_2 and would suggest a second hyperbolic response with very high apparent K_M for H_2O_2. Accordingly, we used **Eqn. 3.3** to fit the data. Where k_{cat} and K_M are the apparent kinetic parameters that best fit the hyperbolic (i.e., low K_M) component, and k_{app} is the slope of the linear (i.e., high K_M) component and would correspond to k_{cat}/K_M for a second H_2O_2 disproportionation mechanism.

$$\frac{v_o}{[E]_T} = \frac{k_{cat}[S]}{K_M + [S]} + k_{app}[S] \qquad \textbf{(3.3)}$$

3.2.6. Extent of ABTS oxidation vs H_2O_2 consumption. The amount of ABTS oxidized was evaluated by setting up reactions containing 0.1 mM ABTS, 20 nM enzyme, and varying concentrations of H_2O_2 (i.e., 0.1 - 5 mM) and allowing them for at least 10 minutes as previously described [138, 187]. We also used a stopped-flow method to evaluate the quantity of $ABTS^{+\bullet}$ generated during H_2O_2-dependent enzyme turnover (see below).

3.2.7. Stopped-flow kinetic studies of R418A. Dominant heme intermediates formed by R418A KatG were monitored using a PC-upgraded SX18.MV rapid reaction analyzer from Applied Photophysics (Leatherhead, UK). As demonstrated previously, we used ascorbate to scavenge the radical oxidation products of $ABTS^{+\bullet}$ [138, 187]. Single mixing experiments contained 6 μM R418A KatG in syringe A in 5 mM phosphate buffer pH 7.0. In syringe B, we had 0.2 mM ascorbate, 0.2 mM ABTS, and varying concentrations of H_2O_2 in 100 mM acetate buffer, pH 5.0. As mentioned above, we also applied stopped-flow to determine the quantity of ABTS radical generated during the consumption of a range of H_2O_2 concentrations. These experiments were set up in the same way except that ascorbate was excluded from syringe B. In these experiments, ABTS was quantified by monitoring absorbance at 645 nm using a molar absorptivity of 13,500 $M^{-1}cm^{-1}$ [177].

3.2.8. Freeze-quench preparation of EPR samples. R418A KatG was concentrated to about 300 μM using an Amicon Ultra-4 centrifugal filter (MW cutoff of 50 kD) as was done for wild-type MtKatG. The first syringe contained ~ 300 μM R418A in 5 mM phosphate buffer pH 7.0 while the second syringe contained about 667 molar equivalents of H_2O_2 in 100 mM acetate buffer, pH 5.0. Reactions testing the effect of ABTS (2.0 mM) and ascorbate (6.0 mM) along with H_2O_2 were also prepared. EPR samples for R418A were prepared as described previously for the wild-type KatG [187].

3.2.9. EPR measurements. All X-band (9 GHz) EPR spectra were collected using a Bruker EMX spectrometer operating in a perpendicular mode as previously described [187]. Instrument parameters, unless otherwise stated were the same as had been described for wild-type KatG. Data analyses were carried out as previously described [187].

3.3. Results and Discussion

3.3.1. Steady-state kinetic evaluations of R418 variants. Intramolecular electron transfer from and to the KatG unique MYW adduct appears to be a frequent event necessary for the enzyme's unique catalase activity, its inactivation, and restoration mechanisms [127, 129, 143]. We have demonstrated in chapter 2 that the KatG proximal tryptophan is a hotspot for off-catalase oxidation leading to catalase inactive states. These states are restored by PxEDs at acidic pH, coincidentally the same conditions under which the arginine switch moves to its 'out' or 'R' conformation. In this chapter, we investigated the role of the switch in controlling KatG intramolecular electron transfer.

We performed site-directed mutagenesis and successfully expressed and isolated R418K and R418A KatG. Their spectral features were consistent with one another and with wild-type KatG (Table 3.1). The catalase and peroxidase activities of both variants were measured under standard assay conditions and compared with wild-type KatG. In every respect, wild-type and R418K showed highly similar steady-state kinetic parameters for catalase and peroxidase activities. However, R418A showed a greatly diminished catalase activity (30-fold decrease in k_{cat}; 140-fold decrease in k_{cat}/K_M) (Table 3.2). The R418A variant also showed a 75-fold *increase* in the apparent k_{cat}/K_M for *peroxidase* activity with respect to H_2O_2 concentration. These results are highly similar for those reported for the analogous variants of KatG enzymes from other organisms [133, 134, 139, 190]. The correspondence between the catalase activities of wild-type and R418K KatG was also observed at low pH (i.e., 5.0) (Table 3.2). Just as we have reported for the wild-type enzyme [138], there were also two components to the response of R418K KatG to increasing H_2O_2 concentration (Fig. 3.2) [138].

Table 3.1. Spectral features of *MtKatG* and R418 variants[a]

Protein	Absorption Feature			
	Soret (γ) (nm)	CT[b] 2 (nm)	CT 1 (nm)	RZ[c]
*Mt*KatG	408	500	633	0.64
R418K	408	500	633	0.61
R418A	407	501	632	0.57

[a]All spectra were recorded at 23 ℃ using 100 mM phosphate buffer, pH 7.0.

[b]CT = charge transfer transition. CT 1 is usually near 640 nm, and CT 2 is usually near 500 nm.

[c]RZ = Reinheitzahl ratio. Ratio of absorbance at the Soret λ_{max} versus absorbance at 280 nm.

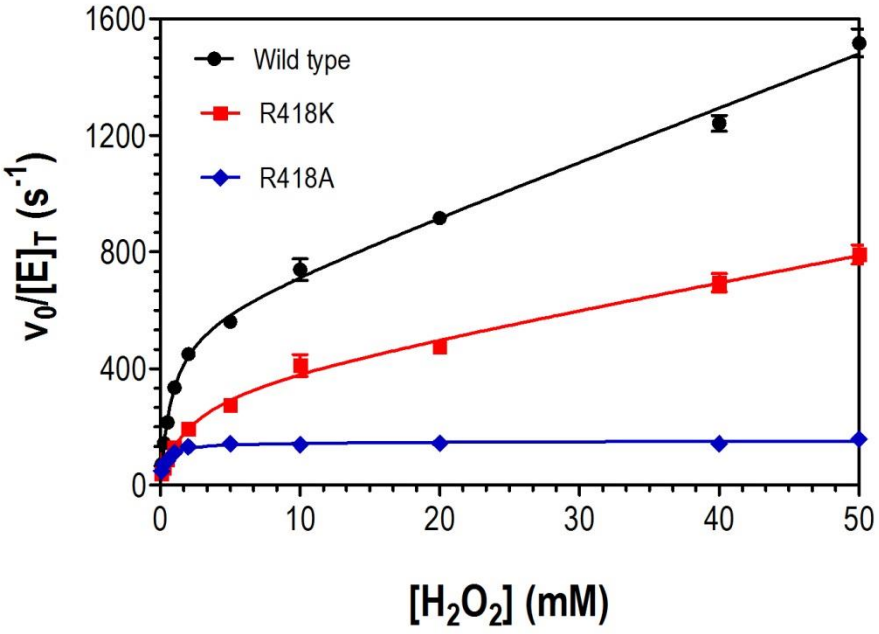

Figure 3.2. pH-dependence of the catalase activity of O_2 R418A and R418K KatG in the presence and absence of 0.1 mM ABTS. Panel A shows the catalase activity of R418K (circles) and R418A (squares) in the absence (blue) and presence (orange) of ABTS. Panel B shows the pH dependence of the difference in catalase activity with and without ABTS for R418A (blue) and R418K (orange). These values were obtained by subtracting rates obtained without ABTS from those obtained with ABTS. All reactions contained 20 nM KatG enzymes.

A hyperbolic phase at low H_2O_2 concentration (< 10 mM) (k_{cat} = 330 s^{-1}, k_{cat}/K_M = 2.0 × 10^5 $M^{-1}s^{-1}$) gave way to a linear component at higher H_2O_2 concentration (k_{app} = 9.5 × 10^3 $M^{-1}s^{-1}$). R418A KatG contrasted with this behavior by showing only a single hyperbolic response to H_2O_2. Its parameters (k_{cat} = 150 s^{-1}, k_{cat}/K_M = 5.2 × 10^5 $M^{-1}s^{-1}$) were most similar to the initial hyperbolic phases observed for wild-type and R418K KatG. This indicated that there may be two variations on the catalase mechanism of KatG, one arginine switch-dependent and the other switch-independent. The k_{cat} values were essentially the same for R418A KatG at pH 7 and pH 5 (accounting for stoichiometry 134 s^{-1} versus 150 s^{-1}, respectively) (Table 3.2). This is in close agreement with data recently reported for R461A variant of extracellular KatG (KatG2) from *Magnaporthe grisea* [190]. Strikingly, we also observed that the apparent k_{cat}/K_M for H_2O_2 for our R418A KatG variant was 66-fold higher at pH 5.0 than at pH 7.0 (Table. 3.2).

3.3.2. Catalase pH Profiles for R418 Variants. The catalase activities of R418A and R418K KatG were compared across a pH range from 3 to 8 (Fig. 3.3). This also revealed evidence of switch-dependent and -independent mechanisms for catalase activity. As we have observed for wild-type KatG [138], the R418K variant had a clear catalase optimum at pH 7.5. A shoulder was observed in the profile at pH 5.0 which diminished toward zero below pH 4.0. Conversely, R418A KatG showed an optimum only at pH 5.0. Interestingly, R418K and R418A showed virtually identical catalase-activities at pH 5.0 and below.

When a PxED, ABTS, was included, R418K KatG showed two optima for catalase activity. The one at pH 7.5 was identical to that observed without PxED. However, at pH 5.0, what appeared as a shoulder without PxEDs was now a clear maximum. Indeed, the activity at pH 5.0, was now about two-fold greater than that observed at pH 7.5. In the

presence of PxED, R418A KatG still showed an optimum only at pH 5.0, but now the activity was about eight-fold greater than in the absence of ABTS (Fig. 3.3A). Subtracting catalase activity observed without ABTS from that detected in the presence of ABTS (Fig. 3B) revealed essentially the same pH profile for the PxED stimulatory effect in both variants.

Together, these data suggest that there are two variations of the unique catalase mechanism of KatG. One variation requires a positively charged side chain (Arg or Lys) at position 418. As discussed elsewhere, the capacity of this side chain to act as a binary conformational switch is a central feature of this variation, and it appears that PxEDs have little capacity to stimulate catalatic turnover by this pathway. However, a second variation is observed at lower pH, producing an optimum activity near pH 5.0. This variation does not require the arginine switch and produces a comparatively modest catalase activity. However, inclusion of an appropriate PxED, stimulates the catalatic activity of this mechanism such that efficient catalatic H_2O_2 degradation is observed at low pH even in the absence of an arginine switch.

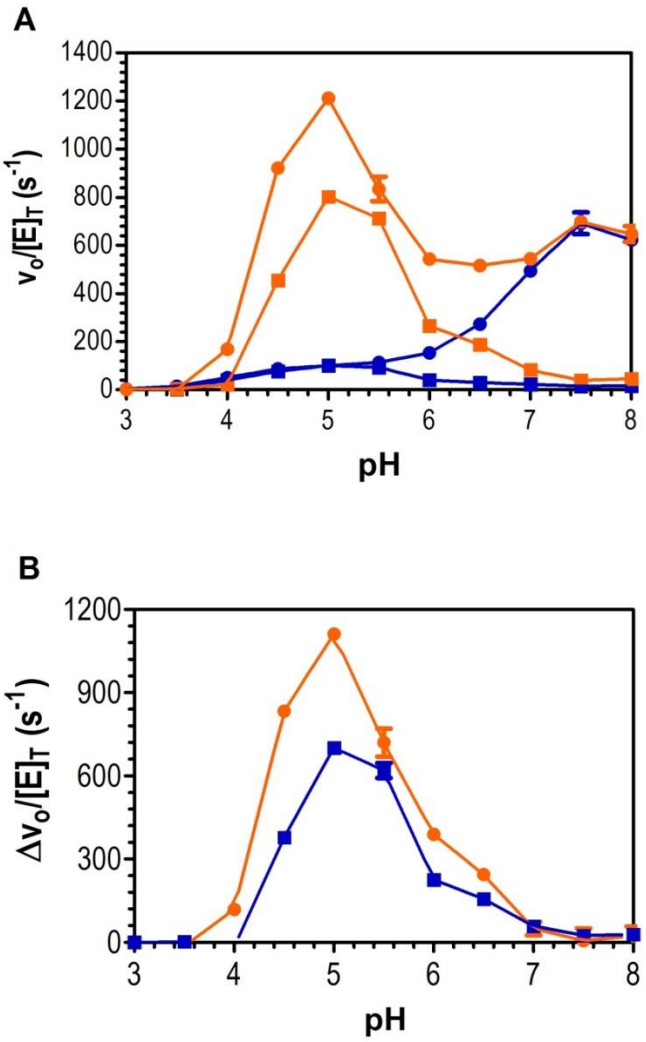

Figure 3.3. pH-dependence of the catalase activity of O_2 R418A and R418K KatG in the presence and absence of 0.1 mM ABTS. Panel A shows the catalase activity of R418K (circles) and R418A (squares) in the absence (blue) and presence (orange) of ABTS. Panel B shows the pH dependence of the difference in catalase activity with and without ABTS for R418A (blue) and R418K (orange). These values were obtained by subtracting rates obtained without ABTS from those obtained with ABTS. All reactions contained 20 nM KatG enzymes.

Table 3.2. Catalase and peroxidase kinetic parameters for *Mt*KatG and variants.

Activity (substrate)	Parameter	KatG Protein		
		*Mt*KatG	R418K	R418A
Catalase (pH 7.0)[a]				
	k_{cat} (s^{-1})	7736 ± 82	5112 ± 50	268 ± 46
	K_M (mM)	7.0 ± 0.3	4.6 ± 0.2	34 ± 13
	k_{cat}/K_M ($M^{-1}s^{-1}$)	(1.1 ± 0.06) × 10^6	(1.1 ± 0.06) × 10^6	(8 ± 4) × 10^3
Peroxidase[b] (H_2O_2)[c]				
	k_{cat} (s^{-1})	13.5 ± 0.3	16.3 ± 1.0	10.5 ± 0.1
	K_M (mM)	0.24 ± 0.03	0.30 ± 0.04	0.0025 ± 0.0001
	k_{cat}/K_M ($M^{-1}s^{-1}$)	(5.6 ± 0.8) × 10^4	(6 ± 1) × 10^4	(4.2 ± 0.2) × 10^6
Peroxidase (ABTS)[d]				
	k_{cat} (s^{-1})	29.2 ± 0.2	25.1 ± 0.4	27.4 ± 0.3
	K_M (mM)	0.14 ± 0.01	0.11 ± 0.01	0.14 ± 0.01
	k_{cat}/K_M ($M^{-1}s^{-1}$)	(2.1 ± 0.2) × 10^5	(2.3 ± 0.24) × 10^5	(2.0 ± 0.2) × 10^5
Catalase (pH 5.0)[e]				
	k_{cat} (s^{-1})[f]	570 ± 30	330 ± 30	150 ± 3
	K_M (mM)[f]	0.8 ± 0.1	1.6 ± 0.4	0.29 ± 0.04
	k_{cat}/K_M ($M^{-1}s^{-1}$)[f]	(7.1 ± 1.3) × 10^5	(2.0 ± 0.7) × 10^5	(5.2 ± 0.8) × 10^5
	k_{app} ($M^{-1}s^{-1}$)[g]	(1.8 ± 0.1) × 10^4	(9.5 ± 0.7) × 10^3	-

[a]Activity was determined by H_2O_2 consumption observed at 240 nm at 23 °C in 100 mM phosphate buffer, pH 7.0.
[b]All peroxidase activity assays were performed at 23 °C in 50 mM acetate buffer, pH 5.0.
[c]Peroxidase parameters with respect to H_2O_2 were determined using 0.1 mM ABTS.
[d]Peroxidase parameters with respect to ABTS were determined using 1.0 mM H_2O_2.
[e]Activity was determined by O_2 production at 23 °C in 50 mM acetate buffer, pH 5.0.
[f]Kinetic parameters for low K_M component.
[g]Apparent second-order rate constant for high-K_M component.

3.3.3. Stimulation of R418 Variants by PxEDs. As mentioned above, the PxED ABTS stimulated the catalase activity of R418K and R418A, producing an optimum near pH 5.0. The stimulatory effect, expressed as k_{cat} enhancement was similar for wild-type, R418K, and R418A KatG. As observed for wild-type KatG, ABTS, TMPD, and chlorpromazine all produced *at least* 5-fold stimulation of catalase activity for R418A and R418K KatG. Neither pyrogallol nor ascorbate were able to stimulate the activity of either variants (Fig. 3.4). Interestingly, in contrast to the wild-type enzyme, the benzidine derivatives TMB and *o*-dianisidine were unable to stimulate the activity of either R418A or R418K.

We have consistently observed that the stimulation of catalase activity by PxEDs (e.g. ABTS) nets very little in accumulation of the PxED in its oxidized form (e.g., $ABTS^{\bullet+}$) [138, 187]. The W321F variant produces even less $ABTS^{\bullet+}$ per H_2O_2 consumed than wild-type KatG [187]. These data are consistent with the hypothesis that formation of oxidized PxED (e.g., $ABTS^{\bullet+}$) is a manifestation of the rescue of inactive intermediates formed by off-pathway electron transfer. R418K KatG showed nearly identical behavior to wild-type enzyme; however, R418A produced substantially greater quantities of $ABTS^{\bullet+}$ at all H_2O_2 concentrations tested (Fig. 3.5). There was a substantial inverse dependence on H_2O_2 such that at 5 mM H_2O_2, R418A KatG produced 0.015 equivalents of $ABTS^{\bullet+}$, three fold greater than that produced by either wild-type or R418K KatG. At 0.25 mM H_2O_2, R418A KatG produced 0.1 equivalents $ABTS^{\bullet+}$, 14-fold greater than the 0.007 equivalents produced by either wild-type and R418K KatG. We were able to observe the same phenomenon using an alternative stopped-flow method (see *Materials and Methods*). This approach not only confirmed the results of our benchtop spectrophotometric assay, but also allowed us to evaluate $ABTS^{\bullet+}$ yields upon reaction of R418A with as little as 1 molar yields upon

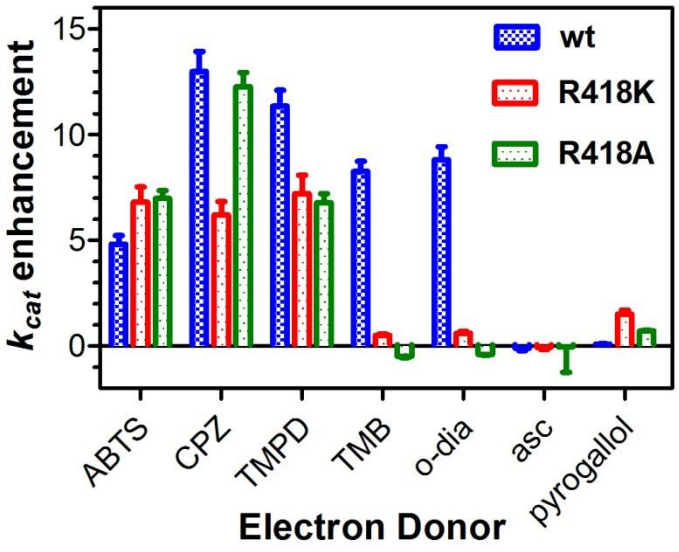

Figure 3.4. Effect of PxEDs on the apparent k_{cat} for the catalase activity of wild-type (blue), R418A (red), and R418K KatG (green). Activity was measured by O_2 production as described in in *Materials and methods*. Reactions contained 20 nM enzyme and were carried out in 50 mM acetate buffer pH 5.0, at 23℃. All electron donors were present at a concentration of 0.1 mM.

reaction of R418A with as little as 1 molar equivalent of H_2O_2. The yield continued to increase with lower H_2O_2 concentration such that 0.65 eq. $ABTS^{\bullet+}$ (1.95 μM) was generated when R418A KatG was reacted with one equivalent of H_2O_2 (i.e., 3 μM) (Fig. 3.5).

These data suggest that off-catalase electron transfer becomes a much more frequent event when the positive charge of the arginine switch is absent. Thus, while the catalase activity of the R418A variant at pH 5.0 is comparable to wild-type and R418K KatG, it comes with a larger extent of PxED oxidation. The inverse dependence of H_2O_2 concentration is also noteworthy. Although a very modest trend is observed with wild-type and R418K KatG, at low H_2O_2 concentrations, R418A KatG appears to approach a situation where an off-pathway electron transfer event occurs with nearly every other turn of the enzyme's catalase cycle.

3.3.4. Stopped-flow Evaluation of R418A KatG. We monitored H_2O_2 consumption by wild-type and R418A KatG at 240 nm. To consume a comparable concentration of H_2O_2 required R418A about 3.5 times longer than wild-type KatG (Fig. 3.6A). Given the concentration of H_2O_2 used in the experiment, this is precisely consistent with the catalase kinetic parameters recorded for each protein at pH 5.0. Interestingly, like wild-type, R418A KatG showed the characteristic slow return of the ferric state following the depletion of H_2O_2 (Fig. 3.6B). We have shown previously that catalase-inactive intermediates accumulate during turnover of the wild-type enzyme at pH 5.0. The slow return of the ferric state is an indicator of that phenomenon. Supposing R418 influences the release of O_2 for the ferric enzyme to return as has been proposed [135, 142], then wild-type KatG should show larger rates of H_2O_2 consumption (i.e., steady-state turnover) *and* a much faster return of the ferric state after H_2O_2 depletion than R418A. However, wild-type only shows greater

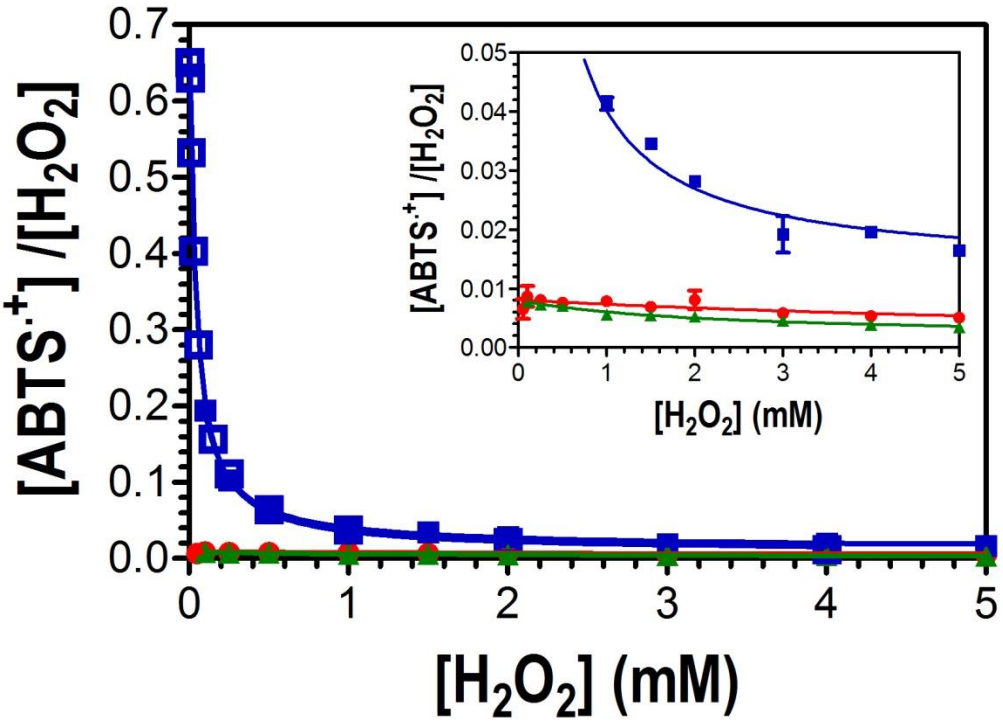

Figure 3.5. Amount of ABTS radical generated to H_2O_2 consumed for wild-type (▲), R418A (■), and R418K KatG (●). All reactions contained 20 nM KatG enzymes and were carried out in 50 mM acetate buffer pH 5.0, at 23℃. ABTS was present at a concentration of 0.1 mM. The extent of $ABTS^{\bullet+}$ production by R418A KatG was also measured by stopped flow (□) according to the procedure described in *Materials and methods* at 0.003, 0.006, 0.015, 0.03, 0.06, 0.15, 0.25, 0.5, 1.0, 2.0, and 4.0 mM H_2O_2.

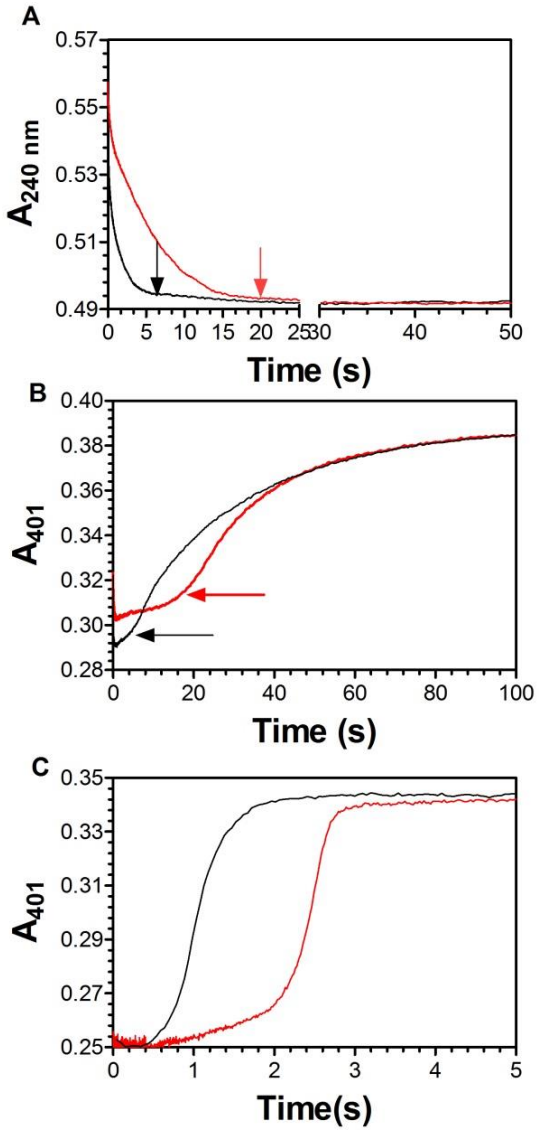

Figure 3.6. H_2O_2 consumption and return of the ferric (resting) state of wild-type (black), and R418A KatG (red). Decrease in H_2O_2 concentration (A) was monitored at 240 nm upon mixing 3 μM wild-type (black) or R418A KatG (red) with 2 mM H_2O_2. Return of ferric states, in the absence (B) and in the presence (C) of 0.1 mM ABTS was observed at 401 nm for wild-type (black) and R418A KatG (red). Reactions were carried out by stopped-flow using 50 mM acetate buffer pH 5.0 at 4℃. The arrows indicate the time points corresponding to the cessation of H_2O_2 consumption for each KatG protein.

rates of H_2O_2 consumption. The return of the ferric state thereafter is nearly identical between both proteins (Fig. 3.6A). These data suggest that although R418A KatG steady-state turnover is slower than wild-type due to the participation of the arginine switch in the KatG catalase mechanism, both proteins accumulate similarly unreactive states during turnover. Indeed, at the conclusion of H_2O_2 consumption, R418A KatG shows spectral features that are consistent with inactive intermediates observed for wild-type KatG (Fig. 3.7). However, for reasons that remain unclear, at all reaction times, the spectral features of R418A KatG are less pronounced than for wild-type enzyme. For example, 2.5 ms after reaction with H_2O_2, wild-type KatG shows very clear absorption bands at 416 (Fig. 3.7A), as well as 540, and 578 nm (Fig. 3.7B); R418A KatG shows a clear Soret band near 416 nm (Fig. 3.7C), but only weak features are observed at 540 and 578 nm (Fig. 3.7D).

For both wild-type and R418A, inclusion of a PxED (i.e., ABTS), dramatically reduced the time necessary to consume H_2O_2 and increased the rate of return of the ferric state at the conclusion of the reaction (Fig. 3.6C). Even in the presence of ABTS, R418A still required more time than wild-type to consume a given concentration of H_2O_2. This is indicative of the direct participation of R418 in the catalase mechanism of KatG [135, 142], for example facilitating the conversion of compound III* (Fe^{III}-$O_2^{\bullet-}$ [$MYW^{\bullet+}$]) to ferric enzyme in the last step of the cycle [135, 142]. However, the stimulatory effect of ABTS on catalatic turnover and the return of the KatG ferric state at the conclusion of H_2O_2 consumption confirms that wild-type and R418A KatG share similar properties with respect to accumulation and rescue of inactive states.

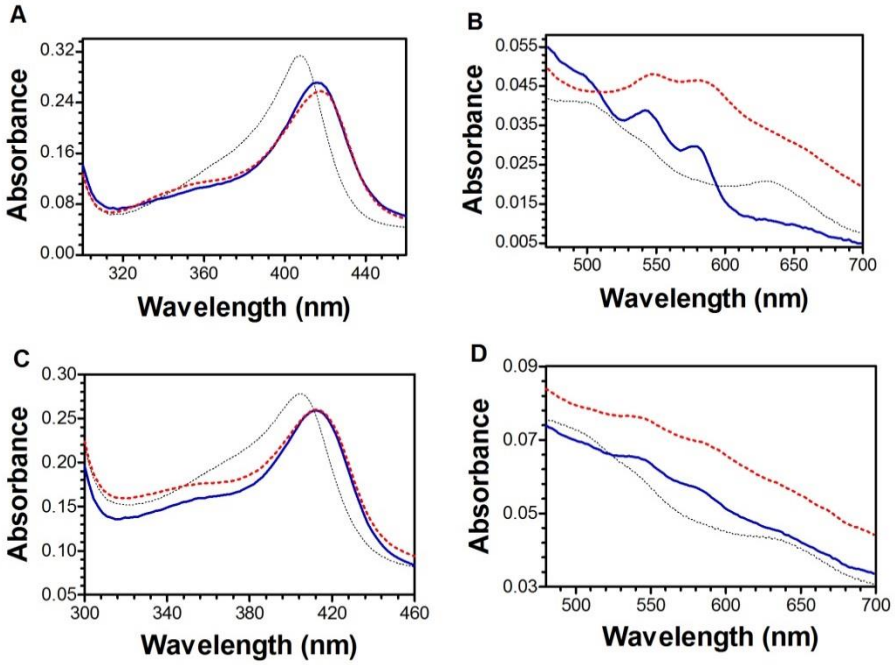

Figure 3.7. Spectra from reaction of wild-type and R418A KatG with H_2O_2. Wild-type (A and B) and R418A KatG (C and D) were reacted with 2 mM H_2O_2 by stopped-flow and spectra for the Soret band (A and C) and Q bands (B and D) were recorded throughout the reaction by diode array. Spectra obtained 2.5 ms after reaction with H_2O_2 are shown in blue. Spectra recorded at the time corresponding to H_2O_2 depletion (6 s for wild-type and 20 s for R418A) are shown in red. Spectra recorded for the ferric enzyme following mixing with buffer alone are shown by dashed lines. All reactions were carried out as described for Fig. 3.6.

3.3.5. Rapid Freeze-Quench EPR Evaluations of R418A KatG. Greater off-pathway electron transfer during turnover of R418A KatG could be accounted for by one of two scenarios (or some combination of both). In the first, the absence of R418 would increase the *frequency* of off-pathway oxidation of the proximal tryptophan (W321), a residue we have already shown is a hotspot for misdirected electron transfer [187]. Alternatively, the absence of the arginine switch may make other residues more susceptible to oxidation. In order to investigate these possibilities, we examined the protein-based radicals formed by R418A KatG upon reaction with H_2O_2 by RFQ-EPR. Similar to wild-type KatG, a clear narrow-doublet was observed 10 ms after mixing with H_2O_2 (Fig. 3.8A). Its lineshape intensity were nearly identical to that observed for the wild-type enzyme under similar conditions at the same time point (Fig. 3.9).

When the reaction between R418A and H_2O_2 was quenched at the point of peroxide depletion (i.e., 20 s after mixing), a broad singlet radical was observed. This spectrum was highly similar to that observed for wild-type KatG at its point of peroxide depletion (i.e., 6 s) (Figs. 3.10, 3.11, and S1). Broadening of this nature has been attributed to an exchange-coupling interaction between a tryptophan-based radical and the iron of the heme center. More specifically for KatG and one of its closest relatives, C*c*P, this spectrum has been assigned as a radical centered on the so-called proximal tryptophan (W321 in *M. tuberculosis* KatG; see Fig. 3.1) [130]. Compared to the wild-type narrow doublet, the broad singlet radicals produced by wild-type and R418A KatG were both resistant to power saturation, but the broad radical from the wild-type enzyme was more so than R418A with $P_{1/2}$ values of 0.012 and 0.005, respectively (Figs. 3.11 and 3.12). The best fit of the data for both radicals returned *b* values substantially below the theoretical lower limit of 1.0 for

inhomogenous broadening (i.e., 0.48 for wild-type and 0.55 for R418A KatG). Elsewhere, this has been interpreted as broadening due to a dipolar coupling interaction [191].

Similar to the wild-type enzyme, R418A KatG protein-based radicals persisted long after consumption of H_2O_2 had ceased. Reactions freeze-quenched 100 s after mixing R418A and H_2O_2 showed a narrow singlet radical species (g = 2.0046) (Fig. 3.13B). The signal was markedly less intense than that detected at 20 s. Due to its relatively low intensity, and because the ferric form of the enzyme was also accumulating in this time range, a second feature (g = 1.9760) was observed in the spectrum (Fig. 3.14B). All contribution of this feature was absent when the temperature for spectral collection was raised to 20 K (Fig. 3.14B). Thus the properties of this feature are consistent with the g_z contribution from high-spin ferric KatG. The protein-based radical component of the spectrum was still observed at higher temperature (20 K and 60 K). The narrow signal (peak to trough = 14.8 G) and its easy saturation with increasing microwave power all suggested that this signal was due to a radical more remote from the heme center than that detected 20 s after mixing with H_2O_2. Even 5 min. after mixing with H_2O_2 (and 4 min. 40 s after cessation of H_2O_2 consumption), R418A KatG still showed the presence of protein-based radicals (Fig. 3.13C and 3.14C). The intensity of the protein-based radical contribution was considerably less, but g_z component of the high-spin resting state was essentially unchanged from that observed at 1 min. As for the protein based radical(s) detected 1 min. after reaction with H_2O_2, the signal was narrow and easily saturated by increasing microwave power, indicating that these radicals were based on a residue(s) more remote from the heme center than the proximal tryptophan.

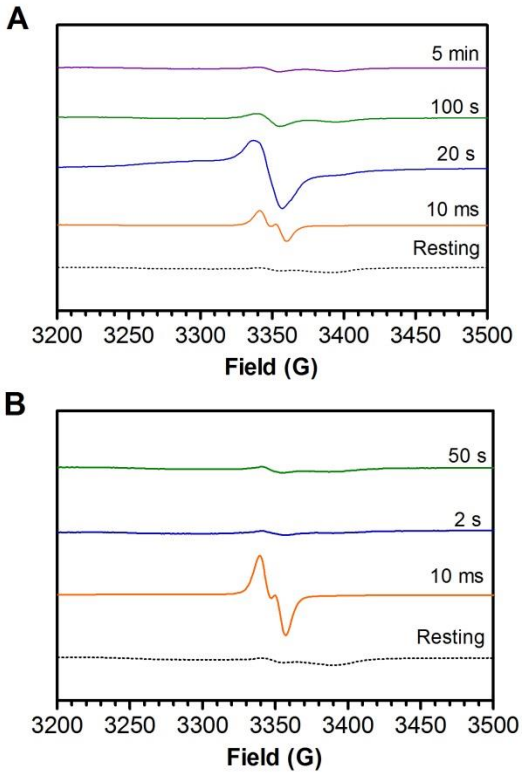

Figure 3.8. EPR spectra for protein-based radicals observed during R418A KatG reaction with H_2O_2 in the absence (A) and presence of ABTS/ascorbate (B). Enzyme (150 μM) and H_2O_2 (100 mM) were mixed and allowed to react for the times indicated prior freeze-quenching with liquid ethane. ABTS and ascorbate, when present, were 2 mM and 6 mM respectively. The reactions were carried out in 100 mM acetate buffer pH 5.0 at 4℃. The spectra were recorded at 4.5 K with spectrometer settings as described in *Materials and methods*.

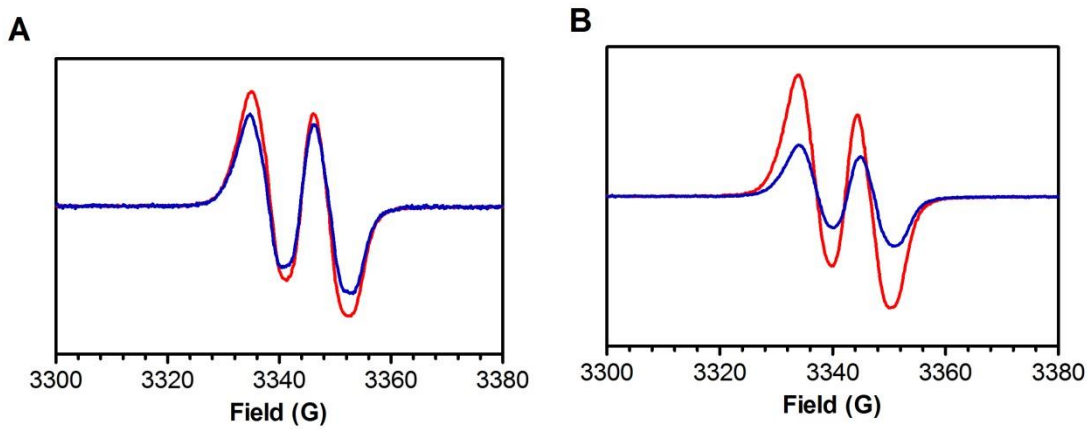

Figure 3.9. Comparison of EPR spectra for protein-based radicals 10 ms after mixing wild-type (A) and R418A KatG (B) with H_2O_2 in the presence (red trace) and absence (blue trace) of ABTS/ascorbate. All spectra were recorded at 77 K. Reaction conditions were as described for Figure 3.8. Spectrometer settings were as described in the *Materials and Methods*.

Just as we observed for wild-type KatG, the narrow doublet radical was the only radical observed for R418A when a PxED (i.e., ABTS/ascorbate) was included in the reaction (Figs. 3.8B, 3.9, and 3.10). The narrow doublet captured for R418A in the presence of ABTS/ascorbate was about two fold more intense than that detected with H_2O_2 alone (Fig. 3.9B). These data also support the idea that PxEDs provide more assistance for R418A KatG because it is susceptible to greater frequency of off-pathway oxidation events. As we have observed with wild-type KatG, inclusion of ABTS/ascorbate prevented the accumulation of all other radicals observed when R418A KatG was reacted with H_2O_2 alone.

3.3.6. pH, alternative mechanisms, and PxED-enhanced catalase activity. It has long been observed that pH is a critical parameter in KatG structure and function. We noted a striking correspondence between the pH dependence of PxED-stimulated activity, the computationally predicted exploitation of the proximal tryptophan as an electron donor to the Fe^{IV}[porphyrin]$^{\bullet+}$ state of KatG, and the observed conformational position of KatGs arginine switch. Our investigation of W321F KatG in comparison with the wild-type enzyme confirmed the connection between formation of catalase-inactive intermediates during reaction with H_2O_2 and the off-pathway oxidation of the enzyme's proximal tryptophan. That these phenomena were all observed under acidic conditions implied that they were connected to and facilitated by the orientation of the arginine switch away from the active site. The data we have reported here confirm that the absence of the arginine switch from the active site is directly connected to a greater propensity toward off-catalase electron transfer and the need for exogenous electron donors to facilitate efficient catalatic H_2O_2 decomposition.

How an arginine switch-independent catalase mechanism is facilitated at low pH remains to be determined. Indeed, how the arginine switch itself facilitates KatG's unique catalase mechanism is still not fully resolved. However, a consistent feature of mechanisms proposed to date is that orientation of the positively charged switch toward the phenolic oxygen of the MYW cofactor (i.e., the *in* or *Y* conformation) is favorable toward reduction of the MYW radical to the fully covalent state. It is possible that in the absence of the switch (either by its orientation in the *out* or *R* conformation or by R418A substitution) is mitigated to some extent at low pH, providing ample H^+ to coincide with reduction of the MYW adduct radical. As has been surmised through DFT calculations [171], and as we have confirmed previously, the off-pathway oxidation of the proximal tryptophan world also become prominent under these same conditions. Accordingly, the catalase activity that KatG could produce under these conditions would be muted by the greater propensity toward inactivation, and at the same time, inclusion of a PxED would also have a substantial stimulatory effect by returning these inactive states to active catalatic turnover.

The properties of a KatG completely lacking the arginine switch (i.e., R418A) reveal the overlap between a catalase mechanism that is independent of the arginine switch with one that is substantially stimulated by inclusion of a peroxidatic electron donor. Where wild-type and R418K KatG show both an arginine switch-dependent/PxED-independent (optimal near neutral pH) as well as an arginine switch-independent/PxED-stimulated catalase activity (optimal near pH 5.0), the R418A variant only shows the latter. Moreover, the properties of the latter mechanism correspond well to one another whether produced by R418A, R418K, or wild-type KatG.

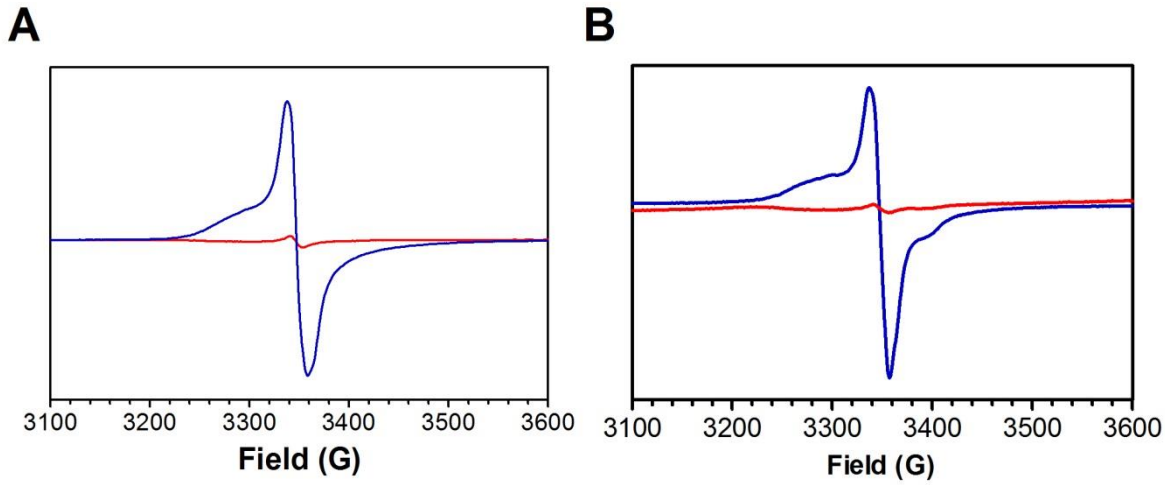

Figure 3.10. Comparison of EPR spectra for protein-based radicals at points of H_2O_2 depletion after mixing wild-type (A) and R418A KatG (B) with 100 mM H_2O_2 in the presence (red trace) and absence (blue trace) of ABTS/ascorbate. All spectra were recorded at 4.5 K.

3.3.7. The arginine switch and off-catalase electron transfer. The first experimental evidence that removal of the arginine switch promotes misdirected protein oxidation was observed at the termination of the process with R418L variant of *M. tuberculosis* KatG [142]. The reaction of this enzyme with H_2O_2 resulted in substantial increases in oxidative protein aggregation. At the other end of the temporal scale, computational analyses determined that the absence of the arginine switch along with protonation of the MYW adduct (as expected at acidic pH) would increase oxidation of the enzymes proximal tryptophan [171]. The data we present here highlights a strong connection between these two endpoints. Our EPR data strongly suggests that the $W321^{\bullet+}$ radical accumulates during catalatic H_2O_2 consumption by R418A KatG. With time, radical transfer away from the active site appears to occur, generating a protein-based radical(s) that shows no evidence of exchange-coupling with the heme iron. In contrast to the narrow doublet (i.e., $MYW^{\bullet+}$), none of these radicals are integral to catalase activity most obviously indicated by the fact that none of them accumulate if an exogenous PxED (i.e., ABTS) is also present in the reaction. Additionally, R418A produces far more oxidized PxED (i.e., $ABTS^{\bullet+}$) for a given concentration of H_2O_2. Given the relatively large size of ABTS and its inability to transit the substrate channel and access the heme and active site, its very oxidation indicates that radical transfer to the enzyme's solvent accessible surface has occurred to a much greater extent with R418A than wild-type KatG.

Certainly, W321 (i.e., the proximal tryptophan) is a prominent starting point for off-catalase protein oxidation (Fig. 3.15, path a) for wild-type KatG and also the R418A KatG enzyme. Although the R418A variant appears to permit a much higher frequency of off-catalase electron transfer events, it is not clear whether this still occurs largely *via* W321F or

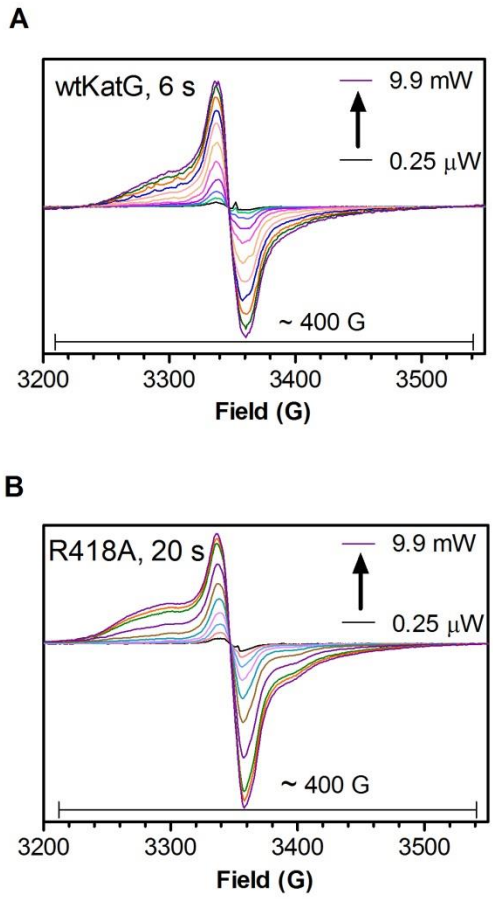

Figure 3.11. Effect of power on the radicals observed for wild-type (A) and R418A KatG (B) at their points of H_2O_2 depletion 6 s and 20 s respectively.

.

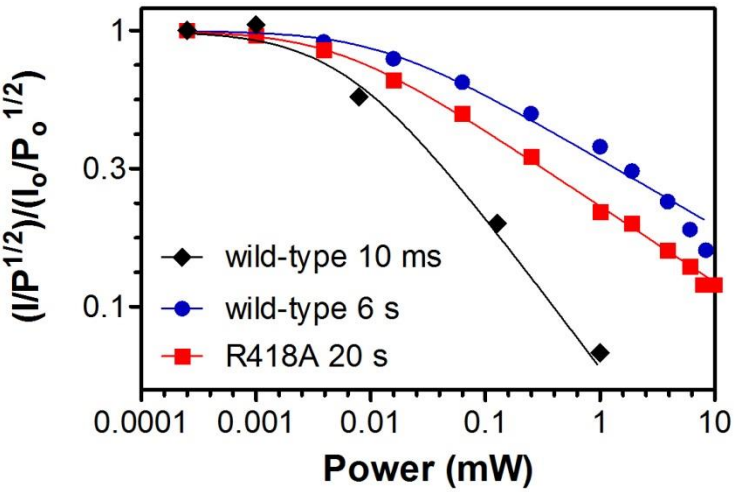

Figure 3.12. Effect of microwave power on EPR signal intensity for KatG radicals observed upon reaction with H_2O_2. The KatG variant and the time of freeze quenching for each radical are indicated.

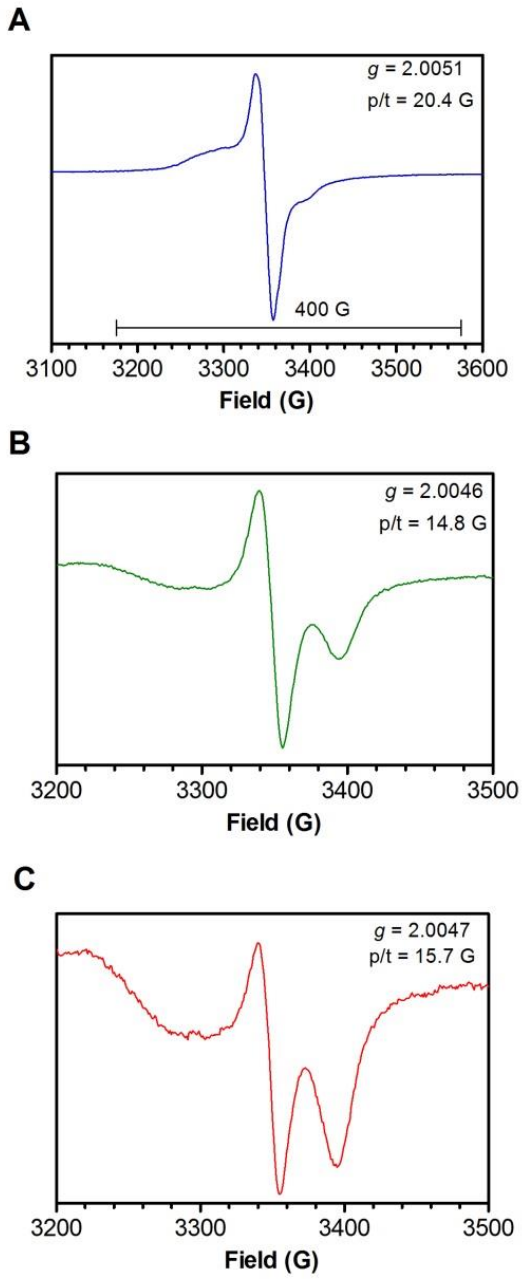

Figure 3.13. EPR spectra recorded for freeze-quenched samples from reactions of R418A KatG with H_2O_2. The radicals observed at 20 s (A), 100 s (B), and 5 min (C) are shown. Reaction conditions were as described for Figure 7. All spectra were recorded at 4.5 K.

if other pathways, perhaps *via* reduction of the $MYW^{\bullet+}$ by another amino acid instead of by the Fe^{III}-$O_2^{\bullet-}$ heme (Fig. 3.15, path b). At the point H_2O_2 consumption ceases, $W321^{\bullet+}$ appears to be the dominant radical. On the other hand, the steep inverse dependence of off-catalase electron transfer on H_2O_2 concentration may indicate that compound I* (i.e., Fe^{IV}=O[$MYW^{\bullet+}$]) is an important branch point (Fig. 3.15, path b), not just compound I (i.e., Fe^{IV}=O[$porphyrin^{\bullet+}$]).

3.3.8. What is KatG peroxidase activity? Intramolecular electron transfers involving the KatG-unique MYW adduct appears to be a frequent event necessary for the enzyme's unique catalase activity [127, 129, 143]. It is also noteworthy that across KatG's two-domain structure, easily oxidizable tryptophan and tyrosine side chains (i.e., ~18 tryptophans, and ~12 tyrosines) are concentrated in the N-terminal domain where the heme/active site are located rather than in the C-terminal domain which lacks heme and a functioning active site. Thus, the catalase activity of KatG notwithstanding, the KatG structure is one which seems ideal for the transfer of oxidizing equivalents from the enzyme's buried heme center to the protein surface. At first, this seems counter to optimal KatG catalase function. The enzyme's proximal tryptophan is oxidized during catalatic turnover, leading to the accumulation of catalase-inactive states [187]. This is mitigated to a large extent by substitution of the proximal tryptophan with a far less oxidizable residue, phenylalanine. It is odd, then, that the proximal tryptophan is universally conserved among KatGs in this position, and a universal feature of KatG N-terminal domain is a high density of other relatively oxidizable amino acids.

Interestingly, we have also observed that inclusion of selected PxEDs prevents the accumulation of catalase-inactive states, stimulating catalatic H_2O_2 consumption. Because these donors are unable to directly access the KatG heme, their action appears to result from interaction with oxidizing equivalents transferred to the enzyme's surface, and the extent to which oxidized PxED accumulates reflects the frequency of off-catalase electron transfer and rescue of the resulting inactive intermediates.

Thus it appears that the KatG structure has been optimized for more than just efficient catalase function. Through this combination of factors, KatG is able to maintain a highly efficient catalase over a wide range of pH. However, in addition to this, a peroxidatic function is also permitted, but it is carried out in such a way that the PxED substrate never interferes with catalatic turnover, but instead sustains catalase function simultaneous with its own oxidation. As such, the control of activity distribution (catalase and/or peroxidase) rests with the enzyme itself and depends almost entirely on the control of intramolecular electron transfer. Our investigations suggest that the arginine switch not only manages intramolecular electron transfer to facilitate a completely novel catalase mechanism, it also more broadly serves to distribute intramolecular electron transfer to allow for a peroxidase function. As pH decreases and the arginine switch is directed away from the MYW adduct, peroxidatic function begins to emerge. But rather than interfering with catalase activity, the PxED by its own oxidation serves to maintain KatG in an efficient state of catalase turnover while simultaneously accumulating the PxED in its oxidized state.

The stimulation observed by PxEDs expands KatGs capacity as an efficient catalase and allows for the simultaneous and synergistic operation of a peroxidase function. Notably, the conditions most conducive to this mode of KatG action coincide with conditions

employed by higher eukaryotes to thwart invasion by pathogenic bacteria. The oxidative burst initiated by human neutrophils in response to bacterial infection is one example.

In light of the versatility of KatG in its mechanisms of decomposition of H_2O_2, perhaps it should not be surprising to find its prominent use among notorious pathogenic bacteria, including *M. tuberculosis*, *Yersinia pestis*, *E. coli* O157:H7, and *Magnaporthe grisea*.

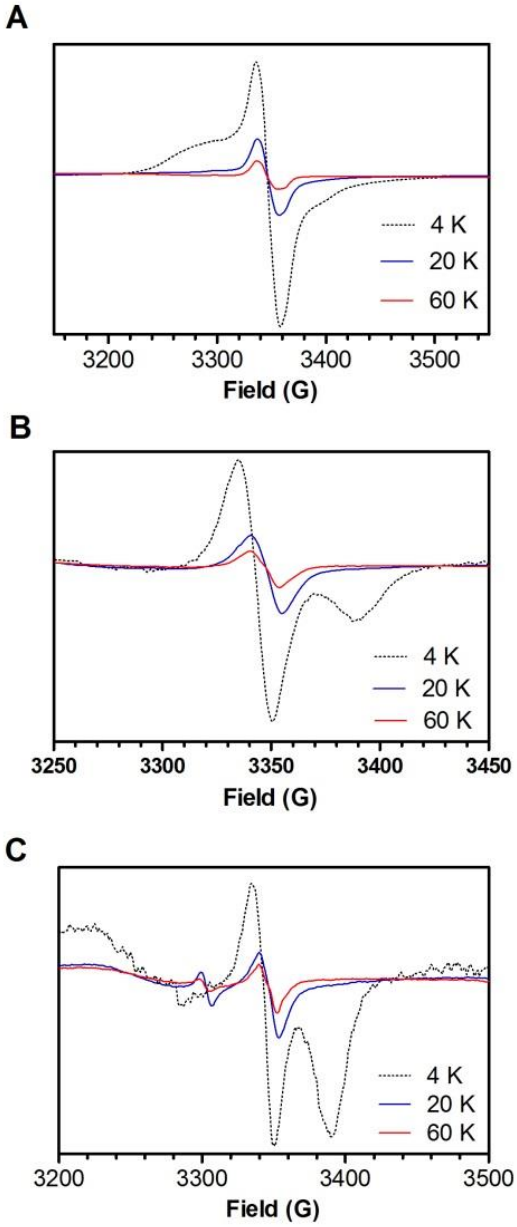

Figure 3.14. Effect of temperature on the radicals observed for R418A after reaction with H_2O_2 at 20 s (A), 100 s (B), and 5 min (C). The *g*-value observed for each radical is presented in Table S3.Reaction conditions are indicated in the *Materials and Methods*.

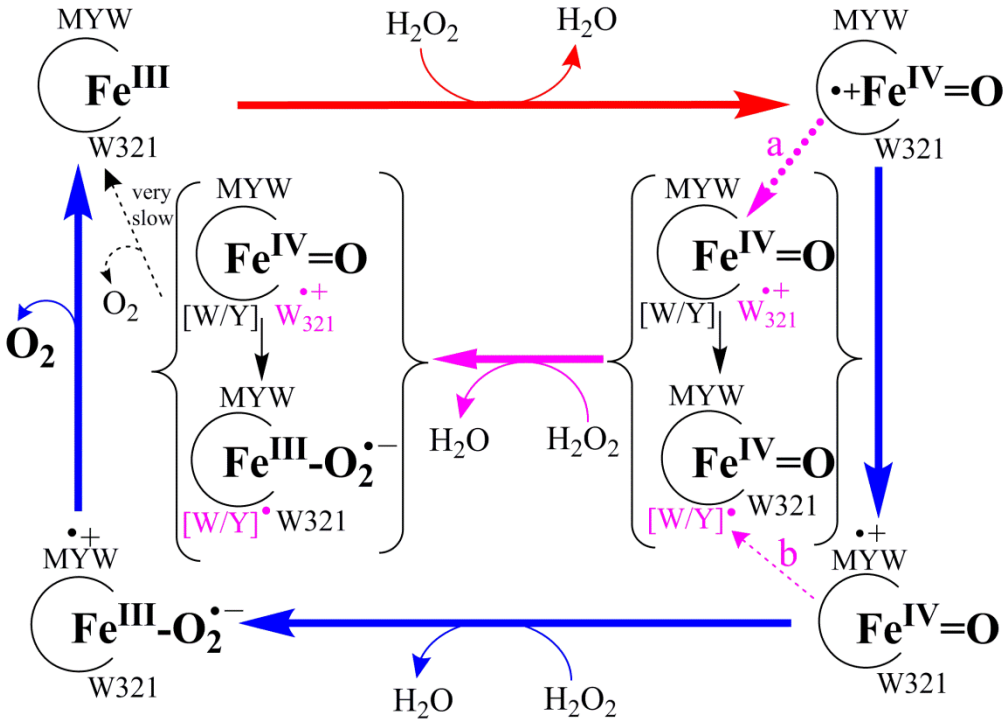

Figure 3.15. Scheme representing the proposed mechanism for inactivation of KatG catalase activity by way of the arginine switch and its prevention by a peroxidatic electron donor (PxED). Off-pathway reduction of the MYW adduct radical of compound I* by the proximal tryptophan (W_{321}) (path a) and or remote radicals (path b) produces the catalase-inactive intermediate compound I^i (I^i). Subsequent reaction of I^i with H_2O_2 is expected to produce a catalase-inactive compound III-like intermediate (III^i) where the protein based radical is unable to facilitate oxidation and O_2 release from the Fe^{III}-$O_2^{\bullet-}$ complex. Species derived from radical migration from W_{321} to oxidizable residues further from the active site (W/Y) could occur with either Fe^{IV}=O or Fe^{III}-$O_2^{\bullet-}$ intermediates. The conversion of I^i to the active ferric state by a peroxidatic electron donor (PxED) is proposed. The Met-Tyr-Trp covalent adduct and its corresponding radical are represented by MYW and $MYW^{\bullet+}$, respectively. The proximal tryptophan and its corresponding radical are represented by W_{321} and $W_{321}^{\bullet+}$, respectively. An unspecified KatG oxidizable amino acid and its corresponding radical are represented by [W/Y] and $[W/Y]^{\bullet}$, respectively.

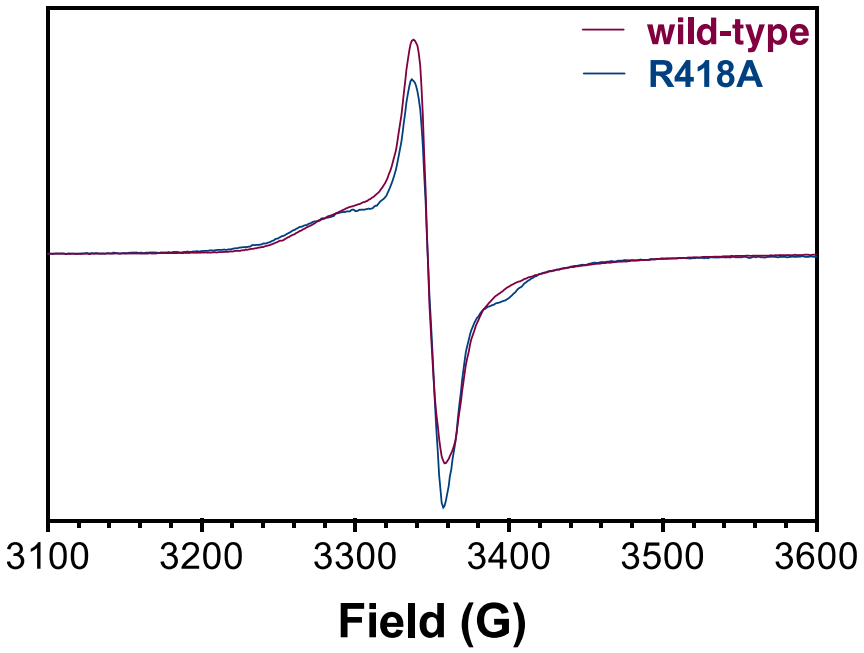

Figure S3.1: Superimposition of the exchange-coupled radical captured at the points of peroxide depletion for wild-type KatG (6 s) and R418A KatG (20 s)

Table 3.3. Effect of electron donors on catalase kinetic parameters at pH 5.0.

Electron Donor[a]		KatG Protein		
	Parameter[b,c]	MtKatG	R418K	R418A
None	k_{cat} (s^{-1})	570 ± 30	330 ± 30	148 ± 3
	K_M (mM H_2O_2)	0.8 ± 0.1	1.6 ± 0.4	0.29 ± 0.04
	k_{cat}/K_M ($M^{-1}s^{-1}$)	(7.1 ± 1.3) × 10^5	(2.1 ± 0.7) × 10^5	(5.1 ± 0.8) × 10^5
ABTS	k_{cat} (s^{-1})	3300 ± 60	2560 ± 40	1184 ± 0.1
	K_M (mM H_2O_2)	0.83 ± 0.05	0.85 ± 0.06	1.1 ± 0.1
	k_{cat}/K_M ($M^{-1}s^{-1}$)	(4.0 ± 0.3) × 10^6	(3.0 ± 0.3) × 10^6	(1.1 ± 0.1) × 10^6
CPZ	k_{cat} (s^{-1})	7940 ± 120	2382 ± 24	1960 ± 60
	K_M (mM H_2O_2)	1.1 ± 0.1	0.36 ± 0.02	4.8 ± 0.5
	k_{cat}/K_M ($M^{-1}s^{-1}$)	(7.2 ± 0.8) × 10^6	(6.6 ± 0.01) × 10^6	(4.1 ± 0.6) × 10^5
TMPD	k_{cat} (s^{-1})	7010 ± 60	2700 ± 80	1150 ± 40
	K_M (mM H_2O_2)	1.2 ± 0.1	0.79 ± 0.07	1.0 ± 0.1
	k_{cat}/K_M ($M^{-1}s^{-1}$)	(6.0 ± 0.5) × 10^6	(3.4 ± 0.4) × 10^6	(1.1 ± 0.2) × 10^6
TMB	k_{cat} (s^{-1})	5220 ± 70	490 ± 20	82 ± 6
	K_M (mM H_2O_2)	0.70 ± 0.05	0.07 ± 0.02	3.1 ± 0.9
	k_{cat}/K_M ($M^{-1}s^{-1}$)	(7.4 ± 0.6) × 10^6	(7.0 ± 0.08) × 10^6	(2.6 ± 1) × 10^4
o-dianisidine	k_{cat} (s^{-1})	5600 ± 100	540 ± 30	93 ± 5
	K_M (mM H_2O_2)	0.49 ± 0.05	0.13 ± 0.04	4.1 ± 0.8
	k_{cat}/K_M ($M^{-1}s^{-1}$)	(1.2 ± 0.14) × 10^7	(4.2 ± 1.5) × 10^6	(2.3 ± 0.6) × 10^4
pyrogallol	k_{cat} (s^{-1})	630 ± 20	820 ± 30	250 ± 10
	K_M (mM H_2O_2)	0.20 ± 0.03	0.30 ± 0.04	0.30 ± 0.04
	k_{cat}/K_M ($M^{-1}s^{-1}$)	(3.1 ± 0.6) × 10^6	(2.7 ± 0.5) × 10^6	(8.3 ± 1.4) × 10^5

Table S3.1: *g*-values for radicals observed for R418A after reaction with H_2O_2 at 20 s, 100 s and 5 mins.

	20 s radical	100 s radical	100 s g_z	5 min. radical	5 min. g_z
4 K	2.0051	2.0046	1.9765	2.0047	1.9768
20 K	2.0048	2.0043		2.0044	
60 K	2.0047	2.0042		2.0344	

Chapter Four: Summary

In the 30 years since its initial discovery, KatG has been a study in dichotomy. Its initial characterization noted its two dominant activities; catalase and peroxidase [137, 192]. Kinetically, catalase appeared to dominate, particularly at neutral pH, but structurally, it became abundantly clear that KatG emerged from peroxidatic relatives and still had an active site that was nearly identical to cytochrome c peroxidase (C*c*P), a canonical peroxidase with no catalase activity. Similar to C*c*P, its close relative, KatG appears to readily accommodate intramolecular electron transfer where a canonical compound I (Fe^{IV}=O [porphyrin]$^{\bullet+}$) accepts an electron from the protein to form a Fe^{IV}=O [protein]$^{\bullet+}$ intermediate [124, 126, 127, 129, 140] .

Here, as well two opposing ideas have emerged regarding the identity of the protein-based radical(s) and their relevance to KatG activity. Reaction of KatG with peracetic acid (PAA) generates the ferryl intermediate associated with catalytic heme proteins including a (Fe^{IV}=O [proximal Trp]$^{\bullet+}$) species first observed in C*c*P and famously named "compound ES" [131, 132]. Compound ES is known to be central to the C*c*P catalytic mechanism [131, 132]. Yet, PAA is not a physiological substrate for either C*c*P or KatG. The timing of the observation of the KatG (Fe^{IV}=O [proximal Trp]$^{\bullet+}$) state does not seem to fit the rates of catalatic turnover of the enzyme. Indeed, reaction of KatG with PAA produces substantial oxidative modifications of KatG protein that would be inconsistent with competent physiological function. On the other hand, reaction of KatG with H_2O_2 produces a completely different set of radical species. The dominant radical, a narrow doublet, has been assigned to KatG unique MYW adduct, and the redox cycling of this protein-based cofactor

has been proposed to account for catalase activity [124, 127, 142]. Still, this species is associated with an apparent heme state, Fe^{III}-$O_2^{\bullet-}$, that has until recently only been associated with inactive peroxidases *and* catalases.

KatG's split personality carries over into the nature of the interplay between its catalase and peroxidase activities. From the beginning, these have been thought to be mutually antagonistic. Consistent with this, KatG's catalase and peroxidase activities show two distinct pH profiles with little overlap between them. Further, KatG variants that lack catalase activity often show substantial increases in peroxidase activity. Nevertheless, we have recently observed that inclusion of peroxidatic electron donors does not inhibit catalase activity as anticipated, but rather stimulates it by an order of magnitude.

Finally, even in its structure, KatG has an arginine switch that can occupy one of two positions. An 'out' position at acidic pH (i.e < 6.5) and an 'in' position at basic pH (i.e., > 6.5) [133, 134]. As with many other KatG features, the position of the switch is pH-dependent, and computational studies have indicated that the position of the switch helps determine the electron source to reduce the porphyrin radical of compound I, the MYW adduct or the proximal Trp. The research described in this dissertation makes a substantial leap forward in reconciling these binary and often paradoxical observations.

4.1. Bridging the Divide: Research Findings

This research is the first to observe the exchange-coupled proximal Trp radical (i.e., $W321^{\bullet+}$) in the presence of H_2O_2 rather than PAA, and we are also the first to observe both the $MYW^{\bullet+}$ narrow doublet and the exchange-coupled $W321^{\bullet+}$ radicals in the same reaction sequence. Indeed, we captured both radicals at different time points during KatG catalatic

consumption of H_2O_2. At early reaction times when KatG shows optimum rates of H_2O_2 degradation, the $MYW^{\bullet+}$ narrow-doublet is the dominant species. As turnover progresses, KatG loses activity and the radical is transferred to the KatG proximal tryptophan (i.e., $W321^{\bullet+}$) such that it is the dominant species at the cessation of H_2O_2 consumption. This is the first residue to accumulate in its oxidized radical state, and it appears to be a conduit for subsequent radical migration to remote sites. With oxidizing equivalents held on remote residues (and not on the MYW adduct), KatG is unable to complete its catalatic cycle and catalase-inactive states accumulate. The two KatG protein-based radicals are also connected to each other by way of the arginine switch. At low pH or in the absence of the arginine switch, spin density is localized more on the exchange-coupled proximal tryptophanyl radical while at basic pH, spin density is localized more on the narrow-doublet radical [171].

Second, this thesis elucidates the nature of the interplay of KatG's two dominant activities. They are not mutually exclusive as has long been believed. Rather, PxEDs stimulate catalase activity simultaneously preventing the accumulation of *all* protein-based radicals with the solitary exception of the MYW adduct radical. Minimal accumulation of PxEDs in their radical states relative to the concentration of H_2O_2 consumed (e.g., 0.008 $ABTS^{\bullet+}$ per H_2O_2 consumed) is in stark contrast with typical peroxidatic stoichiometry (i.e., 2 $ABTS^{\bullet+}$ per H_2O_2 consumed). This reveals that PxEDs produce a substantial stimulation of H_2O_2 detoxification by repairing relatively rare off-catalase electron transfer events. Replacement of W321 with a residue that cannot be oxidized by the Fe^{IV}=O[porphyrin]$^{\bullet+}$ state of KatG produces greater catalase activity than wild-type enzyme. As a result, inclusion of PxEDs produces a smaller stimulatory effect with W321F KatG. In other words, the problem of off-pathway electron transfer has been addressed at the protein level, reducing

the need for intervention of exogenous electron donors. The striking conclusion is that KatG is far more a catalase than previously appreciated; it appears that KatG's peroxidase activity is merely a manifestation of 'misfired' catalatic turnover, and the role of a PxED is to maximize *catalase* activity. Consistent with these ideas and the well-known very narrow substrate access channel of the enzyme, PxEDs are unable to prevent accumulation of the $MYW^{\bullet+}$ radical. Instead, they appear to perform their catalase rescue mechanism at the enzyme's surface. Our data suggest that W321 oxidation is the first step in a radical transfer pathway to the surface.

Third, the research reported here addresses the role of the Arg switch in KatG radical transfer reaction mechanisms. The unique pH-dependence of the PxED stimulatory effect (none at pH 7.0 to optimal at pH 5.0) and the clear observation of the $MYW^{\bullet+}$ early and the $W321^{\bullet+}$ late in the absence of PxED pointed to a potential role of R418 in the inactivation process.

We observed that R418A KatG has far more catalase activity than was previously supposed, but this is only observed at low pH. Further, the pH profile of R418A catalase activity precisely follows the profile of stimulatory effect of PxEDs. Indeed, R418A catalase activity can be stimulated to nearly the same extent as wild-type KatG by the inclusion of a PxED. Substantial catalase activity can be observed with R418A, but importantly the extent of off-pathway electron transfer appears to be greatly enhanced. In an effect which was inversely dependent on H_2O_2 concentration, the stimulated catalase activity of R418A KatG required a five-fold greater extent of PxED oxidation than wild-type at 5 mM H_2O_2, an effect which grew to 25-fold at 0.1 mM H_2O_2. R418 has been proposed to participate in regulating the pathways of electron transfer, and therefore, the level of observed catalase versus

peroxidase activity. From this thesis, we can postulate that R418 plays an integral role in modulating electron transfer for KatG activity, inactivation, and its restoration mechanisms. It remains unresolved how off-pathway electron transfer is affected by the absence of R418. Does it influence more W321 oxidation or oxidation of alternative residues? A double variant targeting both the proximal tryptophan and the arginine switch will give us insights on the flow of electrons for KatG inactivation. We have preliminary data on the double variant which indicate that it may be a combination of both.

In light of the research presented here, an important question to address is: Why is the proximal tryptophan still present at all? At the very least, W321 does not appear to be useful for the individual activities of KatG. Even distant relatives of KatG like HRP lack the proximal tryptophan. KatGs closest relative, C*c*P has a proximal tryptophan but does not have catalase activity, and as mentioned above, oxidation of this tryptophan is integral to its peroxidatic oxidation of ferrocytochrome c. Notably, because the heme of the substrate (cytochrome c) and the heme of the enzyme (C*c*P) are both buried within their respective proteins, such through-protein electron transfer is necessary to accommodate catalytically competent rates of electron transfer. We speculate from these findings that the role of KatG proximal tryptophan is for the mutual synergism of KatG's two activities. The proximal Trp, and with it, other oxidizable amino acids in KatG participate in off-catalase electron transfer pathways. At first glance, this would appear to be detrimental to the catalase function of KatG. But such events are essential to the peroxidase activity of the enzyme. Elimination of off-catalase electron transfer pathways (e.g., Trp/Tyr replacement by Phe) might serve to optimize catalase activity, but it would also substantially limit if not eliminate KatG's peroxidatic activity with most exogenous electron donors. Strikingly, these off-catalase

electron transfer possibilities have remained open through evolutionary history. The synergistic favor is returned when an exogenous PxED is oxidized, and as a result catalase-inactive intermediates are returned back to active catalase turnover. A peroxidase function is retained, but not at the expense of catalase function. In fact, PxED participation makes efficient H_2O_2 degradation possible over a much wider range of pH. The physiological ramifications of such mutual synergism are potentially far-reaching. For example, it imparts to many prominent pathogenic bacteria the capacity to use KatG as a defense against host-derived H_2O_2 production.

4.2. Future directions.

The results from this dissertation have unraveled many apparently contradictory or paradoxical features of KatG structure and function. However, many issues remain to be resolved. First, a Fe^{III}-$O_2^{\bullet -}$ state has been proposed as a major intermediate in the catalase mechanism of KatG. This is highly unusual because this heme state has previously been regarded as inactive in all catalase and peroxidases. To date, the primary evidence to support this heme structural assignment is UV-visible absorption spectra recorded by stopped-flow during H_2O_2 consumption by KatG. The studies presented here show precisely the kinds of freeze-quench experiments that will be necessary to prepare samples for Mössbauer spectroscopic evaluation. This is expected to provide a much more definitive assignment of the key heme states in the unique catalatic mechanism of KatG. Second, what could be other possible pathways involved in KatG inactivation mechanism and are they still rescuable by PxEDs? A double variant targeting both the proximal tryptophan and arginine switch will unravel this question. This double variant of KatG will also enlighten us on the direction of intramolecular electron transfer in the KatG active site for its activity, inactivation and

restoration mechanisms. For example, if the double variant mimics the behavior of wild-type KatG or R418A KatG, then the data will suggest that the absence of R418 influences inactivation through W321 oxidation instead of opening alternative pathways for KatG intramolecular electron transfer. It would also be important to know if these alternative pathways are still rescuable by PxEDs.

We have discovered properties that will be helpful to identify the physiological PxED for KatG. This has persisted as an unresolved question in the field from the first report of KatG isolation and characterization [137]. We propose that the physiological PxED should *stimulate* KatG catalase activity, it should minimize the accumulation of protein-based radicals but it should not interfere with the unique narrow-doublet radical. As such, we have a novel paradigm to base our search for KatG's physiological electron donor, whether it be a protein like ferrocytochrome c, other larger polymeric material, or a small molecule. Knowledge of KatG physiological substrate will be important not only to understand the mutual synergism between KatGs two dominant activities, but also to better understand how pathogenic organisms use KatG to maximize their survival.

References

[1] E. Cadenas, Biochemistry of oxygen toxicity, Annu. Rev. Biochem., 58 (1989) 79-110.

[2] M.L. Hess, N.H. Manson, Molecular oxygen: friend and foe. The role of the oxygen free radical system in the calcium paradox, the oxygen paradox and ischemia/reperfusion injury, J. Mol. Cell. Cardiol., 16 (1984) 969-985.

[3] S.G. Lindahl, Oxygen and life on earth: an anesthesiologist's views on oxygen evolution, discovery, sensing, and utilization, Anesthesiology, 109 (2008) 7-13.

[4] Y. Zheng, A.R. Brash, On the role of molecular oxygen in lipoxygenase activation: comparison and contrast of epidermal lipoxygenase-3 with soybean lipoxygenase-1, J. Biol. Chem., 285 (2010) 39876-39887.

[5] C. Schweitzer, R. Schmidt, Physical mechanisms of generation and deactivation of singlet oxygen, Chem. Rev., 103 (2003) 1685-1757.

[6] Sharma P, Jha AB, Dubey RS, P. M, Reactive oxygen species, oxidative damage, and antioxidative defense mechanism in plants under stressful conditions, J. Botany, (2012).

[7] G.Y. Lam, J. Huang, J.H. Brumell, The many roles of NOX2 NADPH oxidase-derived ROS in immunity, Semin. Immunopathol., 32 (2010) 415-430.

[8] J. Hirst, M.S. King, K.R. Pryde, The production of reactive oxygen species by complex I, Biochem. Soc. Trans., 36 (2008) 976-980.

[9] J.F. Turrens, Mitochondrial formation of reactive oxygen species, J. Physiol., 552 (2003) 335-344.

[10] M.P. Murphy, How mitochondria produce reactive oxygen species, Biochem. J., 417 (2009) 1-13.

[11] L. Kussmaul, J. Hirst, The mechanism of superoxide production by NADH:ubiquinone oxidoreductase (complex I) from bovine heart mitochondria, Proc. Natl. Acad. Sci. U. S. A., 103 (2006) 7607-7612.

[12] K. Asada, K. Kiso, K. Yoshikawa, Univalent reduction of molecular oxygen by spinach chloroplasts on illumination, J. Biol. Chem., 249 (1974) 2175-2181.

[13] P. Pospisil, Production of reactive oxygen species by photosystem II, Biochim. Biophys. Acta, 1787 (2009) 1151-1160.

[14] A. Telfer, S.M. Bishop, D. Phillips, J. Barber, Isolated photosynthetic reaction center of photosystem II as a sensitizer for the formation of singlet oxygen. Detection and quantum yield determination using a chemical trapping technique, J. Biol. Chem., 269 (1994) 13244-13253.

[15] V. Massey, Activation of molecular oxygen by flavins and flavoproteins, J. Biol. Chem., 269 (1994) 22459-22462.

[16] D.H. Flint, J.F. Tuminello, M.H. Emptage, The inactivation of Fe-S cluster containing hydro-lyases by superoxide, J. Biol. Chem., 268 (1993) 22369-22376.

[17] C.F. Kuo, T. Mashino, I. Fridovich, alpha, beta-Dihydroxyisovalerate dehydratase. A superoxide-sensitive enzyme, J. Biol. Chem., 262 (1987) 4724-4727.

[18] A. Hausladen, I. Fridovich, Superoxide and peroxynitrite inactivate aconitases, but nitric oxide does not, J. Biol. Chem., 269 (1994) 29405-29408.

[19] B.M. Babior, R.S. Kipnes, J.T. Curnutte, Biological defense mechanisms. The production by leukocytes of superoxide, a potential bactericidal agent, J. Clin. Invest., 52 (1973) 741-744.

[20] Y. Yang, A.V. Bazhin, J. Werner, S. Karakhanova, Reactive oxygen species in the immune system, Int. Rev. Immunol., 32 (2013) 249-270.

[21] Y. Yang, S. Karakhanova, J. Werner, A.V. Bazhin, Reactive oxygen species in cancer biology and anticancer therapy, Curr. Med. Chem., 20 (2013) 3677-3692.

[22] J.M. McCord, I. Fridovich, Superoxide dismutase. An enzymic function for erythrocuprein (hemocuprein), J. Biol. Chem., 244 (1969) 6049-6055.

[23] I. Fridovich, Superoxide radical and superoxide dismutases, Annu. Rev. Biochem., 64 (1995) 97-112.

[24] J.S. Kroll, P.R. Langford, K.E. Wilks, A.D. Keil, Bacterial [Cu,Zn]-superoxide dismutase: phylogenetically distinct from the eukaryotic enzyme, and not so rare after all!, Microbiology, 141 (Pt 9) (1995) 2271-2279.

[25] K. Djinovic, G. Gatti, A. Coda, L. Antolini, G. Pelosi, A. Desideri, M. Falconi, F. Marmocchi, G. Rolilio, M. Bolognesi, Structure solution and molecular dynamics refinement of the yeast Cu,Zn enzyme superoxide dismutase, Acta Crystallogr. B, 47 (Pt 6) (1991) 918-927.

[26] I.W. Boucher, A.M. Brzozowski, J.A. Brannigan, C. Schnick, D.J. Smith, S.A. Kyes, A.J. Wilkinson, The crystal structure of superoxide dismutase from Plasmodium falciparum, BMC Struct. Biol., 6 (2006) 20.

[27] J. Wuerges, J.W. Lee, Y.I. Yim, H.S. Yim, S.O. Kang, K. Djinovic Carugo, Crystal structure of nickel-containing superoxide dismutase reveals another type of active site, Proc. Natl. Acad. Sci. U. S. A., 101 (2004) 8569-8574.

[28] T. Hunter, J.V. Bannister, G.J. Hunter, Thermostability of manganese- and iron-superoxide dismutases from Escherichia coli is determined by the characteristic position of a glutamine residue, Eur. J. Biochem., 269 (2002) 5137-5148.

[29] D.P. Barondeau, C.J. Kassmann, C.K. Bruns, J.A. Tainer, E.D. Getzoff, Nickel superoxide dismutase structure and mechanism, Biochemistry, 43 (2004) 8038-8047.

[30] L.P. Nelles, J.A. Arnold, D.S. Willman, Enzymatic production of hydrogen peroxide and acetaldehyde in a pressure reactor, Biotechnol. Bioeng., 36 (1990) 834-838.

[31] J.A. Imlay, The molecular mechanisms and physiological consequences of oxidative stress: lessons from a model bacterium, Nat. Rev. Microbiol., 11 (2013) 443-454.

[32] M.M. Mubarakshina, B.N. Ivanov, I.A. Naydov, W. Hillier, M.R. Badger, A. Krieger-Liszkay, Production and diffusion of chloroplastic H2O2 and its implication to signalling, J. Exp. Bot., 61 (2010) 3577-3587.

[33] B. Rada, T.L. Leto, Oxidative innate immune defenses by Nox/Duox family NADPH oxidases, Contrib. Microbiol., 15 (2008) 164-187.

[34] S. Jang, J.A. Imlay, Hydrogen peroxide inactivates the Escherichia coli Isc iron-sulphur assembly system, and OxyR induces the Suf system to compensate, Mol. Microbiol., 78 (2010) 1448-1467.

[35] B.S. Berlett, E.R. Stadtman, Protein oxidation in aging, disease, and oxidative stress, J. Biol. Chem., 272 (1997) 20313-20316.

[36] F. Bafort, O. Parisi, J.P. Perraudin, M.H. Jijakli, Mode of action of lactoperoxidase as related to its antimicrobial activity: a review, Enzyme Res, 2014 (2014) 517164.

[37] S. Mishra, J. Imlay, Why do bacteria use so many enzymes to scavenge hydrogen peroxide?, Arch Biochem Biophys, 525 (2012) 145-160.

[38] A. Brenot, K.Y. King, B. Janowiak, O. Griffith, M.G. Caparon, Contribution of glutathione peroxidase to the virulence of Streptococcus pyogenes, Infect. Immun., 72 (2004) 408-413.

[39] B. Heym, E. Stavropoulos, N. Honore, P. Domenech, B. Saint-Joanis, T.M. Wilson, D.M. Collins, M.J. Colston, S.T. Cole, Effects of overexpression of the alkyl hydroperoxide reductase AhpC on the virulence and isoniazid resistance of Mycobacterium tuberculosis, Infect. Immun., 65 (1997) 1395-1401.

[40] V.V. Barynin, M.M. Whittaker, S.V. Antonyuk, V.S. Lamzin, P.M. Harrison, P.J. Artymiuk, J.W. Whittaker, Crystal structure of manganese catalase from Lactobacillus plantarum, Structure, 9 (2001) 725-738.

[41] C.J. Reedy, B.R. Gibney, Heme protein assemblies, Chem. Rev., 104 (2004) 617-649.

[42] P. Attri, Y.H. Kim, D.H. Park, J.H. Park, Y.J. Hong, H.S. Uhm, K.N. Kim, A. Fridman, E.H. Choi, Generation mechanism of hydroxyl radical species and its lifetime prediction during the plasma-initiated ultraviolet (UV) photolysis, Sci. Rep., 5 (2015) 9332.

[43] P.M. Wood, The potential diagram for oxygen at pH 7, Biochem. J., 253 (1988) 287-289.

[44] S. Vilhunen, J. Puton, J. Virkutyte, M. Sillanpaa, Efficiency of hydroxyl radical formation and phenol decomposition using UV light emitting diodes and H2O2, Environ. Technol., 32 (2011) 865-872.

[45] M. Zamocky, P.G. Furtmuller, C. Obinger, Evolution of catalases from bacteria to humans, Antioxid. Redox Signal., 10 (2008) 1527-1548.

[46] J.W. Whittaker, Non-heme manganese catalase--the 'other' catalase, Arch Biochem Biophys, 525 (2012) 111-120.

[47] P. Chelikani, X. Carpena, I. Fita, P.C. Loewen, An electrical potential in the access channel of catalases enhances catalysis, J. Biol. Chem., 278 (2003) 31290-31296.

[48] S.P. de Visser, What external perturbations influence the electronic properties of catalase compound I?, Inorg. Chem., 45 (2006) 9551-9557.

[49] J. Bravo, N. Verdaguer, J. Tormo, C. Betzel, J. Switala, P.C. Loewen, I. Fita, Crystal structure of catalase HPII from Escherichia coli, Structure, 3 (1995) 491-502.

[50] M. Alfonso-Prieto, X. Biarnes, P. Vidossich, C. Rovira, The molecular mechanism of the catalase reaction, J. Am. Chem. Soc., 131 (2009) 11751-11761.

[51] A. Diaz, P.C. Loewen, I. Fita, X. Carpena, Thirty years of heme catalases structural biology, Arch Biochem Biophys, 525 (2012) 102-110.

[52] P.C. Loewen, J. Switala, I. von Ossowski, A. Hillar, A. Christie, B. Tattrie, P. Nicholls, Catalase HPII of Escherichia coli catalyzes the conversion of protoheme to cis-heme d, Biochemistry, 32 (1993) 10159-10164.

[53] A. Hillar, P. Nicholls, J. Switala, P.C. Loewen, NADPH binding and control of catalase compound II formation: comparison of bovine, yeast, and Escherichia coli enzymes, Biochem. J., 300 (Pt 2) (1994) 531-539.

[54] X. Carpena, M. Soriano, M.G. Klotz, H.W. Duckworth, L.J. Donald, W. Melik-Adamyan, I. Fita, P.C. Loewen, Structure of the Clade 1 catalase, CatF of Pseudomonas syringae, at 1.8 A resolution, Proteins, 50 (2003) 423-436.

[55] G.N. Murshudov, A.I. Grebenko, V. Barynin, Z. Dauter, K.S. Wilson, B.K. Vainshtein, W. Melik-Adamyan, J. Bravo, J.M. Ferran, J.C. Ferrer, J. Switala, P.C. Loewen, I. Fita, Structure of the heme d of Penicillium vitale and Escherichia coli catalases, J. Biol. Chem., 271 (1996) 8863-8868.

[56] C. Obinger, M. Maj, P. Nicholls, P. Loewen, Activity, peroxide compound formation, and heme d synthesis in Escherichia coli HPII catalase, Arch Biochem Biophys, 342 (1997) 58-67.

[57] T.P. Ko, M.K. Safo, F.N. Musayev, M.L. Di Salvo, C. Wang, S.H. Wu, D.J. Abraham, Structure of human erythrocyte catalase, Acta Crystallogr. D Biol. Crystallogr., 56 (2000) 241-245.

[58] D. Koua, L. Cerutti, L. Falquet, C.J. Sigrist, G. Theiler, N. Hulo, C. Dunand, PeroxiBase: a database with new tools for peroxidase family classification, Nucleic Acids Res., 37 (2009) D261-266.

[59] M. Zamocky, S. Hofbauer, I. Schaffner, B. Gasselhuber, A. Nicolussi, M. Soudi, K.F. Pirker, P.G. Furtmuller, C. Obinger, Independent evolution of four heme peroxidase superfamilies, Arch Biochem Biophys, 574 (2015) 108-119.

[60] D.T. Akin, J.M. Kinkade, Jr., Processing of a newly identified intermediate of human myeloperoxidase in isolated granules occurs at neutral pH, J. Biol. Chem., 261 (1986) 8370-8375.

[61] E. Torres, M. Ayala, Biocatalysis based on heme peroxidases, Chapter 2, Molecular Phylogeny of heme peroxidases, Springer, New York, 2010.

[62] T.J. Fiedler, C.A. Davey, R.E. Fenna, X-ray crystal structure and characterization of halide-binding sites of human myeloperoxidase at 1.8 A resolution, J. Biol. Chem., 275 (2000) 11964-11971.

[63] X. Carpena, P. Vidossich, K. Schroettner, B.M. Calisto, S. Banerjee, J. Stampler, M. Soudi, P.G. Furtmuller, C. Rovira, I. Fita, C. Obinger, Essential role of proximal histidine-asparagine interaction in mammalian peroxidases, J. Biol. Chem., 284 (2009) 25929-25937.

[64] K.G. Welinder, Superfamily of plant, fungal and bacterial peroxidases, Curr. Opin. Struct. Biol., 2 (1992) 388-393.

[65] B.C. Finzel, T.L. Poulos, J. Kraut, Crystal structure of yeast cytochrome c peroxidase refined at 1.7-A resolution, J. Biol. Chem., 259 (1984) 13027-13036.

[66] M. Sundaramoorthy, K. Kishi, M.H. Gold, T.L. Poulos, Preliminary crystallographic analysis of manganese peroxidase from Phanerochaete chrysosporium, J. Mol. Biol., 238 (1994) 845-848.

[67] G.I. Berglund, G.H. Carlsson, A.T. Smith, H. Szoke, A. Henriksen, J. Hajdu, The catalytic pathway of horseradish peroxidase at high resolution, Nature, 417 (2002) 463-468.

[68] P.R. Ortiz de Montellano, Catalytic sites of hemoprotein peroxidases, Annu. Rev. Pharmacol. Toxicol., 32 (1992) 89-107.

[69] N.C. Veitch, Horseradish peroxidase: a modern view of a classic enzyme, Phytochemistry, 65 (2004) 249-259.

[70] T.L. Poulos, S.T. Freer, R.A. Alden, S.L. Edwards, U. Skogland, K. Takio, B. Eriksson, N. Xuong, T. Yonetani, J. Kraut, The crystal structure of cytochrome c peroxidase, J. Biol. Chem., 255 (1980) 575-580.

[71] A.N. Hiner, E.L. Raven, R.N. Thorneley, F. Garcia-Canovas, J.N. Rodriguez-Lopez, Mechanisms of compound I formation in heme peroxidases, J. Inorg. Biochem., 91 (2002) 27-34.

[72] T.L. Poulos, J. Kraut, The stereochemistry of peroxidase catalysis, J. Biol. Chem., 255 (1980) 8199-8205.

[73] E. Derat, S. Shaik, C. Rovira, P. Vidossich, M. Alfonso-Prieto, The effect of a water molecule on the mechanism of formation of compound 0 in horseradish peroxidase, J. Am. Chem. Soc., 129 (2007) 6346-6347.

[74] P. Vidossich, M. Alfonso-Prieto, X. Carpena, I. Fita, P.C. Loewen, C. Rovira, The dynamic role of distal side residues in heme hydroperoxidase catalysis. Interplay between X-ray crystallography and ab initio MD simulations, Arch Biochem Biophys, 500 (2010) 37-44.

[75] P. Vidossich, G. Fiorin, M. Alfonso-Prieto, E. Derat, S. Shaik, C. Rovira, On the role of water in peroxidase catalysis: a theoretical investigation of HRP compound I formation, J. Phys. Chem. B, 114 (2010) 5161-5169.

[76] A.T. Smith, N. Santama, S. Dacey, M. Edwards, R.C. Bray, R.N. Thorneley, J.F. Burke, Expression of a synthetic gene for horseradish peroxidase C in Escherichia coli and folding and activation of the recombinant enzyme with Ca2+ and heme, J. Biol. Chem., 265 (1990) 13335-13343.

[77] M. Gajhede, D.J. Schuller, A. Henriksen, A.T. Smith, T.L. Poulos, Crystal structure of horseradish peroxidase C at 2.15 A resolution, Nat. Struct. Biol., 4 (1997) 1032-1038.

[78] K.G. Welinder, J.M. Mauro, L. Norskov-Lauritsen, Structure of plant and fungal peroxidases, Biochem. Soc. Trans., 20 (1992) 337-340.

[79] I. Morgenstern, S. Klopman, D.S. Hibbett, Molecular evolution and diversity of lignin degrading heme peroxidases in the Agaricomycetes, J. Mol. Evol., 66 (2008) 243-257.

[80] T.K. Kirk, R.L. Farrell, Enzymatic "combustion": the microbial degradation of lignin, Annu. Rev. Microbiol., 41 (1987) 465-505.

[81] H. Wariishi, L. Akileswaran, M.H. Gold, Manganese peroxidase from the basidiomycete Phanerochaete chrysosporium: spectral characterization of the oxidized states and the catalytic cycle, Biochemistry, 27 (1988) 5365-5370.

[82] J. Jarvinen, S. Taskila, R. Isomaki, H. Ojamo, Screening of white-rot fungi manganese peroxidases: a comparison between the specific activities of the enzyme from different native producers, AMB Express, 2 (2012) 62.

[83] C. Bernini, R. Pogni, R. Basosi, A. Sinicropi, The nature of tryptophan radicals involved in the long-range electron transfer of lignin peroxidase and lignin peroxidase-like systems: Insights from quantum mechanical/molecular mechanics simulations, Proteins, 80 (2012) 1476-1483.

[84] M. Zamocky, Q. Garcia-Fernandez, B. Gasselhuber, C. Jakopitsch, P.G. Furtmuller, P.C. Loewen, I. Fita, C. Obinger, X. Carpena, High conformational stability of secreted eukaryotic catalase-peroxidases: answers from first crystal structure and unfolding studies, J. Biol. Chem., 287 (2012) 32254-32262.

[85] A. Caverzan, G. Passaia, S.B. Rosa, C.W. Ribeiro, F. Lazzarotto, M. Margis-Pinheiro, Plant responses to stresses: Role of ascorbate peroxidase in the antioxidant protection, Genet. Mol. Biol., 35 (2012) 1011-1019.

[86] G. Noctor, C.H. Foyer, ASCORBATE AND GLUTATHIONE: Keeping Active Oxygen Under Control, Annu. Rev. Plant Physiol. Plant Mol. Biol., 49 (1998) 249-279.

[87] M. Zamocky, B. Gasselhuber, P.G. Furtmuller, C. Obinger, Turning points in the evolution of peroxidase-catalase superfamily: molecular phylogeny of hybrid heme peroxidases, Cell. Mol. Life Sci., 71 (2014) 4681-4696.

[88] M. Becana, M.A. Matamoros, M. Udvardi, D.A. Dalton, Recent insights into antioxidant defenses of legume root nodules, New Phytol., 188 (2010) 960-976.

[89] F. Passardi, M. Zamocky, J. Favet, C. Jakopitsch, C. Penel, C. Obinger, C. Dunand, Phylogenetic distribution of catalase-peroxidases: are there patches of order in chaos?, Gene, 397 (2007) 101-113.

[90] S. Tanabe, N. Ishii-Minami, K. Saitoh, Y. Otake, H. Kaku, N. Shibuya, Y. Nishizawa, E. Minami, The role of catalase-peroxidase secreted by Magnaporthe oryzae during early infection of rice cells, Mol. Plant. Microbe Interact., 24 (2011) 163-171.

[91] M. Zamocky, P.G. Furtmuller, M. Bellei, G. Battistuzzi, J. Stadlmann, J. Vlasits, C. Obinger, Intracellular catalase/peroxidase from the phytopathogenic rice blast fungus Magnaporthe grisea: expression analysis and biochemical characterization of the recombinant protein, Biochem. J., 418 (2009) 443-451.

[92] M. Zamocky, P.G. Furtmuller, C. Obinger, Two distinct groups of fungal catalase/peroxidases, Biochem. Soc. Trans., 37 (2009) 772-777.

[93] M. Zamocky, P.G. Furtmuller, C. Obinger, Evolution of structure and function of Class I peroxidases, Arch Biochem Biophys, 500 (2010) 45-57.

[94] Y. Zhang, B. Heym, B. Allen, D. Young, S. Cole, The catalase-peroxidase gene and isoniazid resistance of Mycobacterium tuberculosis, Nature, 358 (1992) 591-593.

[95] D. Martins, M. Kathiresan, A.M. English, Cytochrome c peroxidase is a mitochondrial heme-based H2O2 sensor that modulates antioxidant defense, Free Radic. Biol. Med., 65 (2013) 541-551.

[96] A.N. Volkov, P. Nicholls, J.A. Worrall, The complex of cytochrome c and cytochrome c peroxidase: the end of the road?, Biochim. Biophys. Acta, 1807 (2011) 1482-1503.

[97] M.A. Matamoros, J. Loscos, M.J. Coronado, J. Ramos, S. Sato, P.S. Testillano, S. Tabata, M. Becana, Biosynthesis of ascorbic acid in legume root nodules, Plant Physiol., 141 (2006) 1068-1077.

[98] W.R. Patterson, T.L. Poulos, Crystal structure of recombinant pea cytosolic ascorbate peroxidase, Biochemistry, 34 (1995) 4331-4341.

[99] W.R. Patterson, T.L. Poulos, D.B. Goodin, Identification of a porphyrin pi cation radical in ascorbate peroxidase compound I, Biochemistry, 34 (1995) 4342-4345.

[100] O.J. Njuma, E.N. Ndontsa, D.C. Goodwin, Catalase in peroxidase clothing: Interdependent cooperation of two cofactors in the catalytic versatility of KatG, Arch Biochem Biophys, 544 (2014) 27-39.

[101] R. Singh, B. Wiseman, T. Deemagarn, V. Jha, J. Switala, P.C. Loewen, Comparative study of catalase-peroxidases (KatGs), Arch Biochem Biophys, 471 (2008) 207-214.

[102] W. Brunder, H. Schmidt, H. Karch, KatP, a novel catalase-peroxidase encoded by the large plasmid of enterohaemorrhagic Escherichia coli O157:H7, Microbiology, 142 (Pt 11) (1996) 3305-3315.

[103] M. Zamocky, E. Droghetti, M. Bellei, B. Gasselhuber, M. Pabst, P.G. Furtmuller, G. Battistuzzi, G. Smulevich, C. Obinger, Eukaryotic extracellular catalase-peroxidase from Magnaporthe grisea - Biophysical/chemical characterization of the first representative from a novel phytopathogenic KatG group, Biochimie, 94 (2012) 673-683.

[104] T. Bertrand, N.A. Eady, J.N. Jones, Jesmin, J.M. Nagy, B. Jamart-Gregoire, E.L. Raven, K.A. Brown, Crystal structure of Mycobacterium tuberculosis catalase-peroxidase, J. Biol. Chem., 279 (2004) 38991-38999.

[105] X. Carpena, S. Loprasert, S. Mongkolsuk, J. Switala, P.C. Loewen, I. Fita, Catalase-peroxidase KatG of Burkholderia pseudomallei at 1.7A resolution, J. Mol. Biol., 327 (2003) 475-489.

[106] K. Wada, T. Tada, Y. Nakamura, T. Kinoshita, M. Tamoi, S. Shigeoka, K. Nishimura, Crystallization and preliminary X-ray diffraction studies of catalase-peroxidase from Synechococcus PCC 7942, Acta Crystallogr. D Biol. Crystallogr., 58 (2002) 157-159.

[107] Y. Yamada, T. Fujiwara, T. Sato, N. Igarashi, N. Tanaka, The 2.0 A crystal structure of catalase-peroxidase from Haloarcula marismortui, Nat. Struct. Biol., 9 (2002) 691-695.

[108] X. Zhao, H. Yu, S. Yu, F. Wang, J.C. Sacchettini, R.S. Magliozzo, Hydrogen peroxide-mediated isoniazid activation catalyzed by Mycobacterium tuberculosis catalase-peroxidase (KatG) and its S315T mutant, Biochemistry, 45 (2006) 4131-4140.

[109] R.D. Baker, C.O. Cook, D.C. Goodwin, Properties of catalase-peroxidase lacking its C-terminal domain, Biochem. Biophys. Res. Commun., 320 (2004) 833-839.

[110] R.D. Baker, C.O. Cook, D.C. Goodwin, Catalase-peroxidase active site restructuring by a distant and "inactive" domain, Biochemistry, 45 (2006) 7113-7121.

[111] Y. Wang, D.C. Goodwin, Integral role of the I'-helix in the function of the "inactive" C-terminal domain of catalase-peroxidase (KatG), Biochim. Biophys. Acta, 1834 (2013) 362-371.

[112] S.N. Kudalkar, O.J. Njuma, Y. Li, M. Muldowney, N.R. Fuanta, D.C. Goodwin, A role for catalase-peroxidase large loop 2 revealed by deletion mutagenesis: control of active site water and ferric enzyme reactivity, Biochemistry, 54 (2015) 1648-1662.

[113] A. Hillar, B. Peters, R. Pauls, A. Loboda, H. Zhang, A.G. Mauk, P.C. Loewen, Modulation of the activities of catalase-peroxidase HPI of Escherichia coli by site-directed mutagenesis, Biochemistry, 39 (2000) 5868-5875.

[114] G. Regelsberger, C. Jakopitsch, F. Ruker, D. Krois, G.A. Peschek, C. Obinger, Effect of distal cavity mutations on the formation of compound I in catalase-peroxidases, J. Biol. Chem., 275 (2000) 22854-22861.

[115] J. Stubbe, D.G. Nocera, C.S. Yee, M.C. Chang, Radical initiation in the class I ribonucleotide reductase: long-range proton-coupled electron transfer?, Chem. Rev., 103 (2003) 2167-2201.

[116] J. Stubbe, W.A. van Der Donk, Protein Radicals in Enzyme Catalysis, Chem. Rev., 98 (1998) 705-762.

[117] C.M. Wilmot, E.T. Yukl, MauG: a di-heme enzyme required for methylamine dehydrogenase maturation, Dalton Trans, 42 (2013) 3127-3135.

[118] E.T. Yukl, L.M. Jensen, V.L. Davidson, C.M. Wilmot, Structures of MauG in complex with quinol and quinone MADH, Acta Crystallogr. Sect. F Struct. Biol. Cryst. Commun., 69 (2013) 738-743.

[119] E.T. Yukl, F. Liu, J. Krzystek, S. Shin, L.M. Jensen, V.L. Davidson, C.M. Wilmot, A. Liu, Diradical intermediate within the context of tryptophan tryptophylquinone biosynthesis, Proc. Natl. Acad. Sci. U. S. A., 110 (2013) 4569-4573.

[120] R.A. Ghiladi, G.M. Knudsen, K.F. Medzihradszky, P.R. Ortiz de Montellano, The Met-Tyr-Trp cross-link in Mycobacterium tuberculosis catalase-peroxidase (KatG): autocatalytic formation and effect on enzyme catalysis and spectroscopic properties, J. Biol. Chem., 280 (2005) 22651-22663.

[121] R.A. Ghiladi, K.F. Medzihradszky, P.R. Ortiz de Montellano, Role of the Met-Tyr-Trp cross-link in Mycobacterium tuberculosis catalase-peroxidase (KatG) as revealed by KatG(M255I), Biochemistry, 44 (2005) 15093-15105.

[122] L.J. Donald, O.V. Krokhin, H.W. Duckworth, B. Wiseman, T. Deemagarn, R. Singh, J. Switala, X. Carpena, I. Fita, P.C. Loewen, Characterization of the catalase-peroxidase KatG from Burkholderia pseudomallei by mass spectrometry, J. Biol. Chem., 278 (2003) 35687-35692.

[123] C. Jakopitsch, D. Kolarich, G. Petutschnig, P.G. Furtmuller, C. Obinger, Distal side tryptophan, tyrosine and methionine in catalase-peroxidases are covalently linked in solution, FEBS Lett., 552 (2003) 135-140.

[124] J. Suarez, K. Ranguelova, A.A. Jarzecki, J. Manzerova, V. Krymov, X. Zhao, S. Yu, L. Metlitsky, G.J. Gerfen, R.S. Magliozzo, An oxyferrous heme/protein-based radical intermediate is catalytically competent in the catalase reaction of Mycobacterium tuberculosis catalase-peroxidase (KatG), J. Biol. Chem., 284 (2009) 7017-7029.

[125] X. Zhao, S. Yu, K. Ranguelova, J. Suarez, L. Metlitsky, J.P. Schelvis, R.S. Magliozzo, Role of the oxyferrous heme intermediate and distal side adduct radical in the catalase activity of Mycobacterium tuberculosis KatG revealed by the W107F mutant, J. Biol. Chem., 284 (2009) 7030-7037.

[126] C. Jakopitsch, J. Vlasits, B. Wiseman, P.C. Loewen, C. Obinger, Redox intermediates in the catalase cycle of catalase-peroxidases from Synechocystis PCC 6803, Burkholderia pseudomallei, and Mycobacterium tuberculosis, Biochemistry, 46 (2007) 1183-1193.

[127] X. Zhao, J. Suarez, A. Khajo, S. Yu, L. Metlitsky, R.S. Magliozzo, A radical on the Met-Tyr-Trp modification required for catalase activity in catalase-peroxidase is established by isotopic labeling and site-directed mutagenesis, J. Am. Chem. Soc., 132 (2010) 8268-8269.
[128] J. Colin, B. Wiseman, J. Switala, P.C. Loewen, A. Ivancich, Distinct role of specific tryptophans in facilitating electron transfer or as [Fe(IV)=O Trp(*)] intermediates in the peroxidase reaction of Bulkholderia pseudomallei catalase-peroxidase: a multifrequency EPR spectroscopy investigation, J. Am. Chem. Soc., 131 (2009) 8557-8563.
[129] A. Ivancich, C. Jakopitsch, M. Auer, S. Un, C. Obinger, Protein-based radicals in the catalase-peroxidase of synechocystis PCC6803: a multifrequency EPR investigation of wild-type and variants on the environment of the heme active site, J. Am. Chem. Soc., 125 (2003) 14093-14102.
[130] R. Singh, J. Switala, P.C. Loewen, A. Ivancich, Two [Fe(IV)=O Trp*] intermediates in M. tuberculosis catalase-peroxidase discriminated by multifrequency (9-285 GHz) EPR spectroscopy: reactivity toward isoniazid, J. Am. Chem. Soc., 129 (2007) 15954-15963.
[131] A. Ivancich, P. Dorlet, D.B. Goodin, S. Un, Multifrequency high-field EPR study of the tryptophanyl and tyrosyl radical intermediates in wild-type and the W191G mutant of cytochrome c peroxidase, J. Am. Chem. Soc., 123 (2001) 5050-5058.
[132] M. Sivaraja, D.B. Goodin, M. Smith, B.M. Hoffman, Identification by ENDOR of Trp191 as the free-radical site in cytochrome c peroxidase compound ES, Science, 245 (1989) 738-740.
[133] X. Carpena, B. Wiseman, T. Deemagarn, B. Herguedas, A. Ivancich, R. Singh, P.C. Loewen, I. Fita, Roles for Arg426 and Trp111 in the modulation of NADH oxidase activity of

the catalase-peroxidase KatG from Burkholderia pseudomallei inferred from pH-induced structural changes, Biochemistry, 45 (2006) 5171-5179.

[134] X. Carpena, B. Wiseman, T. Deemagarn, R. Singh, J. Switala, A. Ivancich, I. Fita, P.C. Loewen, A molecular switch and electronic circuit modulate catalase activity in catalase-peroxidases, EMBO Rep, 6 (2005) 1156-1162.

[135] B.I. Kruft, R.S. Magliozzo, A.A. Jarzecki, Density Functional Theory Insights into the Role of the Methionine-Tyrosine-Tryptophan Adduct Radical in the KatG Catalase Reaction: O2 Release from the Oxyheme Intermediate, J. Phys. Chem. A, 119 (2015) 6850-6866.

[136] P.C. Loewen, X. Carpena, P. Vidossich, I. Fita, C. Rovira, An ionizable active-site tryptophan imparts catalase activity to a peroxidase core, J. Am. Chem. Soc., 136 (2014) 7249-7252.

[137] A. Claiborne, I. Fridovich, Purification of the o-dianisidine peroxidase from Escherichia coli B. Physicochemical characterization and analysis of its dual catalatic and peroxidatic activities, J. Biol. Chem., 254 (1979) 4245-4252.

[138] E.N. Ndontsa, R.L. Moore, D.C. Goodwin, Stimulation of KatG catalase activity by peroxidatic electron donors, Arch Biochem Biophys, 525 (2012) 215-222.

[139] C. Jakopitsch, A. Ivancich, F. Schmuckenschlager, A. Wanasinghe, G. Poltl, P.G. Furtmuller, F. Ruker, C. Obinger, Influence of the unusual covalent adduct on the kinetics and formation of radical intermediates in synechocystis catalase peroxidase: a stopped-flow and EPR characterization of the MET275, TYR249, and ARG439 variants, J. Biol. Chem., 279 (2004) 46082-46095.

[140] C. Jakopitsch, C. Obinger, S. Un, A. Ivancich, Identification of Trp106 as the tryptophanyl radical intermediate in Synechocystis PCC6803 catalase-peroxidase by

multifrequency Electron Paramagnetic Resonance spectroscopy, J. Inorg. Biochem., 100 (2006) 1091-1099.

[141] B. Wiseman, X. Carpena, M. Feliz, L.J. Donald, M. Pons, I. Fita, P.C. Loewen, Isonicotinic acid hydrazide conversion to Isonicotinyl-NAD by catalase-peroxidases, J. Biol. Chem., 285 (2010) 26662-26673.

[142] X. Zhao, A. Khajo, S. Jarrett, J. Suarez, Y. Levitsky, R.M. Burger, A.A. Jarzecki, R.S. Magliozzo, Specific function of the Met-Tyr-Trp adduct radical and residues Arg-418 and Asp-137 in the atypical catalase reaction of catalase-peroxidase KatG, J. Biol. Chem., 287 (2012) 37057-37065.

[143] A. Ivancich, L.J. Donald, J. Villanueva, B. Wiseman, I. Fita, P.C. Loewen, Spectroscopic and kinetic investigation of the reactions of peroxyacetic acid with Burkholderia pseudomallei catalase-peroxidase, KatG, Biochemistry, 52 (2013) 7271-7282.

[144] H.B. Dunford, *Heme Peroxidases*, Wiley-VCH, New York, 1999.

[145] F.R. Salemme, Structure and function of cytochromes c, Annu. Rev. Biochem., 46 (1977) 299-329.

[146] M. Sono, J.H. Dawson, K. Hall, L.P. Hager, Ligand and halide binding properties of chloroperoxidase: peroxidase-type active site heme environment with cytochrome P-450 type endogenous axial ligand and spectroscopic properties, Biochemistry, 25 (1986) 347-356.

[147] H.B. Dunford, Hewson, W. D., and Steiner, H., Horseradish peroxidase. 29. Reactions in water and deuterium-oxide, cyanide binding, compound-I formation, and reactions of compound-I and compound-II with ferrocyanide., Can. J. Chem., 56 (1978) 2844-2852.

[148] S. Chouchane, S. Girotto, S. Kapetanaki, J.P. Schelvis, S. Yu, R.S. Magliozzo, Analysis of heme structural heterogeneity in Mycobacterium tuberculosis catalase-peroxidase (KatG), J. Biol. Chem., 278 (2003) 8154-8162.

[149] C. Jakopitsch, A. Wanasinghe, W. Jantschko, P.G. Furtmuller, C. Obinger, Kinetics of interconversion of ferrous enzymes, compound II and compound III, of wild-type synechocystis catalase-peroxidase and Y249F: proposal for the catalatic mechanism, J. Biol. Chem., 280 (2005) 9037-9042.

[150] G. Palmer, and Que, L., Jr., Electron Paramagnetic Resonance of Metalloproteins in, Phisical Methods in Bioinorganic Chemistry, University Science Books, Sausalito, California, 2002, pp. 121.

[151] D.A. Svistunenko, J.A. Worrall, S.B. Chugh, S.C. Haigh, R.A. Ghiladi, P. Nicholls, Ferric haem forms of Mycobacterium tuberculosis catalase-peroxidase probed by EPR spectroscopy: Their stability and interplay with pH, Biochimie, 94 (2012) 1274-1280.

[152] J.W. Whittaker, Free radical catalysis by galactose oxidase, Chem. Rev., 103 (2003) 2347-2363.

[153] B.A. Barry, M.K. el-Deeb, P.O. Sandusky, G.T. Babcock, Tyrosine radicals in photosystem II and related model compounds. Characterization by isotopic labeling and EPR spectroscopy, J. Biol. Chem., 265 (1990) 20139-20143.

[154] G. Jeschke, EPR techniques for studying radical enzymes, Biochim. Biophys. Acta, 1707 (2005) 91-102.

[155] M.a.O. Zamocky, C., Molecular phylogeny of heme peroxidases. in Biophysics Based on Heme Peroxidases Springer-Verlag, Berlin, 2010.

[156] J.A. Imlay, Cellular defenses against superoxide and hydrogen peroxide, Annu. Rev. Biochem., 77 (2008) 755-776.

[157] G.A. Uhlich, KatP contributes to OxyR-regulated hydrogen peroxide resistance in Escherichia coli serotype O157 : H7, Microbiology, 155 (2009) 3589-3598.

[158] G.A. Uhlich, C.Y. Chen, B.J. Cottrell, P.L. Irwin, J.G. Phillips, Peroxide resistance in Escherichia coli serotype O157 : H7 biofilms is regulated by both RpoS-dependent and -independent mechanisms, Microbiology, 158 (2012) 2225-2234.

[159] H. Guo, Q. Seet, S. Denkin, L. Parsons, Y. Zhang, Molecular characterization of isoniazid-resistant clinical isolates of Mycobacterium tuberculosis from the USA, J. Med. Microbiol., 55 (2006) 1527-1531.

[160] Y. Zhang, Vilcheze, C., and Jacobs, W.R., Jr., Mechanisms of drug resistance in Mycobacterium tuberculosis. in *Tuberculosis and the Tubercle Bacillus,*, 2nd Ed. ed., American Society for Microbiology, Washington, D.C, 2005.

[161] C.E. Cade, A.C. Dlouhy, K.F. Medzihradszky, S.P. Salas-Castillo, R.A. Ghiladi, Isoniazid-resistance conferring mutations in Mycobacterium tuberculosis KatG: catalase, peroxidase, and INH-NADH adduct formation activities, Protein Sci., 19 (2010) 458-474.

[162] R.L. Moore, L.J. Powell, D.C. Goodwin, The kinetic properties producing the perfunctory pH profiles of catalase-peroxidases, Biochim. Biophys. Acta, 1784 (2008) 900-907.

[163] M. Zamocky, G. Regelsberger, C. Jakopitsch, C. Obinger, The molecular peculiarities of catalase-peroxidases, FEBS Lett., 492 (2001) 177-182.

[164] C. Jakopitsch, E. Droghetti, F. Schmuckenschlager, P.G. Furtmuller, G. Smulevich, C. Obinger, Role of the main access channel of catalase-peroxidase in catalysis, J. Biol. Chem., 280 (2005) 42411-42422.

[165] S.N. Kudalkar, R.A. Campbell, Y. Li, C.L. Varnado, C. Prescott, D.C. Goodwin, Enhancing the peroxidatic activity of KatG by deletion mutagenesis, J. Inorg. Biochem., 116 (2012) 106-115.

[166] C. Jakopitsch, M. Auer, A. Ivancich, F. Ruker, P.G. Furtmuller, C. Obinger, Total conversion of bifunctional catalase-peroxidase (KatG) to monofunctional peroxidase by exchange of a conserved distal side tyrosine, J. Biol. Chem., 278 (2003) 20185-20191.

[167] G. Regelsberger, C. Jakopitsch, P.G. Furtmuller, F. Rueker, J. Switala, P.C. Loewen, C. Obinger, The role of distal tryptophan in the bifunctional activity of catalase-peroxidases, Biochem. Soc. Trans., 29 (2001) 99-105.

[168] S. Yu, S. Girotto, X. Zhao, R.S. Magliozzo, Rapid formation of compound II and a tyrosyl radical in the Y229F mutant of Mycobacterium tuberculosis catalase-peroxidase disrupts catalase but not peroxidase function, J. Biol. Chem., 278 (2003) 44121-44127.

[169] J. Vlasits, C. Jakopitsch, M. Bernroitner, M. Zamocky, P.G. Furtmuller, C. Obinger, Mechanisms of catalase activity of heme peroxidases, Arch Biochem Biophys, 500 (2010) 74-81.

[170] R.A. Ghiladi, K.F. Medzihradszky, F.M. Rusnak, P.R. Ortiz de Montellano, Correlation between isoniazid resistance and superoxide reactivity in mycobacterium tuberculosis KatG, J. Am. Chem. Soc., 127 (2005) 13428-13442.

[171] P. Vidossich, M. Alfonso-Prieto, X. Carpena, P.C. Loewen, I. Fita, C. Rovira, Versatility of the electronic structure of compound I in catalase-peroxidases, J. Am. Chem. Soc., 129 (2007) 13436-13446.

[172] L. Schrodinger, The PyMOL Molecular Graphics System, 2013.

[173] B.C. Finzel, T.L. Poulos, J. Kraut, Crystal structure of yeast cytochrome *c* peroxidase refined at 1.7-A resolution, J. Biol. Chem., 259 (1984) 13027-13036.

[174] S. Moore, 'Round-the-horn site-directed mutagenesis - OpenWetWare., http://openwetware.org/wiki/'Round-the-horn_site-directed_mutagenesis, Accessed June 2014.

[175] C.L. Varnado, D.C. Goodwin, System for the expression of recombinant hemoproteins in *Escherichia coli*, Protein Expr. Purif., 35 (2004) 76-83.

[176] J.K. Falk, in: K.M. Smith (Ed.) Porphyrins and Metalloporphyrins, Elsevier Publishing, New York, 1964, pp. 804-807.

[177] S.L. Scott, W.J. Chen, A. Bakac, J.H. Espenson, Spectroscopic parameters, electrode-potentials, acid ionization-constants, and electron-exchange rates of the 2,2'-azinobis(3-ethylbenzothiazoline-6-sulfonate) radicals and ions, J. Phys. Chem., 97 (1993) 6710-6714.

[178] D.P. Nelson, L.A. Kiesow, Enthalpy of decomposition of hydrogen-peroxide by catalase at 25 degrees C (with molar extinction coefficients of H_2O_2 solutions in UV), Anal. Biochem., 49 (1972) 474-478.

[179] D.C. Goodwin, K.M. Hertwig, Peroxidase-catalyzed oxidation of capsaicinoids: steady-state and transient-state kinetic studies, Arch Biochem Biophys, 417 (2003) 18-26.

[180] D.C. Goodwin, I. Yamazaki, S.D. Aust, T.A. Grover, Determination of rate constants for rapid peroxidase reactions, Anal. Biochem., 231 (1995) 333-338.

[181] A. Liu, S. Potsch, A. Davydov, A.L. Barra, H. Rubin, A. Graslund, The tyrosyl free radical of recombinant ribonucleotide reductase from Mycobacterium tuberculosis is located in a rigid hydrophobic pocket, Biochemistry, 37 (1998) 16369-16377.

[182] J. Suarez, K. Ranguelova, A.A. Jarzecki, J. Manzerova, V. Krymov, X. Zhao, S. Yu, L. Metlitsky, G.J. Gerfen, R.S. Magliozzo, An oxyferrous heme/protein-based radical intermediate is catalytically competent in the catalase reaction of *Mycobacterium tuberculosis* catalase-peroxidase (KatG), J. Biol. Chem., 284 (2009) 7017-7029.

[183] X. Zhao, A. Khajo, S. Jarrett, J. Suarez, Y. Levitsky, R.M. Burger, A.A. Jarzecki, R.S. Magliozzo, Specific function of the Met-Tyr-Trp adduct radical and residues Arg-418 and Asp-137 in the atypical catalase reaction of catalase-peroxidase KatG, J. Biol. Chem., 287 (2012) 37057-37065.

[184] X. Zhao, J. Suarez, A. Khajo, S. Yu, L. Metlitsky, R.S. Magliozzo, A radical on the Met-Tyr-Trp modification required for catalase activity in catalase-peroxidase is established by isotopic labeling and site-directed mutagenesis, J. Am. Chem. Soc., 132 (2010) 8268-8269.

[185] M. Gajhede, D.J. Schuller, A. Henriksen, A.T. Smith, T.L. Poulos, Crystal structure of horseradish peroxidase C at 2.15 A resolution, Nat. Struct. Biol., 4 (1997) 1032-1038.

[186] M. Sundaramoorthy, K. Kishi, M.H. Gold, T.L. Poulos, The crystal structure of manganese peroxidase from *Phanerochaete chrysosporium* at 2.06-A resolution, J. Biol. Chem., 269 (1994) 32759-32767.

[187] O.J. Njuma, Davis, I., Ndontsa, E.N., Liu, A., Goodwin, D.C., Proximal Tryptophan Participation in Catalase-Peroxidase Inactivation: Peroxidatic Electron Donors and the Stimulation of Catalase Activity, J. Biol. Chem., (2016).

[188] M. Wilming, K. Johnsson, Spontaneous Formation of the Bioactive Form of the Tuberculosis Drug Isoniazid, Angew. Chem. Int. Ed. Engl., 38 (1999) 2588-2590.

[189] A. Ivancich, Jouve, H.M., Gaillard, J., EPR evidence for a tyrosyl radical intermediate in bovine liver catalase, J. American. Chem. Society, 118 (1996) 12852-12853.

[190] B. Gasselhuber, M.M. Graf, C. Jakopitsch, M. Zamocky, A. Nicolussi, P.G. Furtmuller, C. Oostenbrink, X. Carpena, C. Obinger, Interaction with the Redox Cofactor MYW and Functional Role of a Mobile Arginine in Eukaryotic Catalase-Peroxidase, Biochemistry, 55 (2016) 3528-3541.

[191] D.J. Hirsh, G.W. Brudvig, Measuring distances in proteins by saturation-recovery EPR, Nat. Protoc., 2 (2007) 1770-1781.

[192] A. Claiborne, D.P. Malinowski, I. Fridovich, Purification and characterization of hydroperoxidase II of Escherichia coli B, J. Biol. Chem., 254 (1979) 11664-11668.